Development of CdZnTe detector systems for space applications

Kuvvetli, Irfan

Publication date:
2003

Document Version
Publisher's PDF, also known as Version of record

Development of CdZnTe detector systems for space applications

Irfan Kuvvetli

Ph.D. Thesis

This thesis has been submitted to the institute Ørsted-DTU, Technical University of Denmark, Kgs. Lyngby, Denmark, in partial for fulfilment of the requirements for the degree of Doctor of Philosophy.

Ørsted•DTU

Technical University of Denmark Ørsteds Plads, building 348 DK-2800 Kgs. Lyngby

DSRI

Danish Space Research Institute Juliane Maries Vej 30 DK-2100 Copenhagen Ø Denmark

Submitted on March 31th 2003

This document has been typeset using LaTeX and (apart from a few typos) is identical to the submitted version.
Electronic versions may be obtained at <www.dsri.dk/∼irfan> or by contacting the author at irfan@dsri.dk.

Front cover. *Bi-parametric distribution of* ^{137}Cs *radiation source. See Chapter* 3 *for more information.*

Preface

This thesis has been submitted to the institute Ørsted-DTU, Technical University of Denmark, Kgs. Lyngby, Denmark, in partial for fulfilment of the requirements for the degree of Doctor of Philosophy (PhD). The work presented here has been carried out under the supervision of Prof. Uffe Korsbech and under the supervision of Dr. Carl Budtz-Jørgensen between November 1999 and March 2003 at the Ørsted-DTU, Technical University of Denmark and the Danish Space Research Institute DSRI.

One of the goals of this research was to understand and develop a model for CdZnTe drift strip detectors. A serious concern for space use of this type of detectors is the effect of particle induced radiation damage, which is known to affect the electron collection. At DSRI, in collaboration with the cyclotron facility at Copenhagen University Hospital, we have performed a study of radiation effects by exposing a 2.7 mm thick CdZnTe drift strip detector to 30 MeV protons. The radiation damage was studied as a function of depth inside the detector material. A computer model was developed in order to describe the CdZnTe drift strip detector. The computer model that emulates the physical processes of the charge transport in the CdZnTe drift strip detector was used to derive the charge trapping parameter, $\mu\tau_e$ (the product of charge mobility and trapping time for electrons) as a function of proton fluence.

Acknowledgements

Financial support from the Danish Space Research Institute during the 3 years of this project is gratefully acknowledged.

My thesis supervisor at DTU, Associate Professor Uffe Korsbech was tireless in his support of this project. Many thanks are owed for his intellectual direction and encouragement.

My thesis supervisor at DSRI, Dr. Carl Budtz-Jørgensen was more than a supervisor for me since the beginning of my Ph.D study. His motivation and flair for establishing international collaborations and finding a way to finance such ventures is impressive and added greatly to the content of this work.

My appreciation is also extended to the following people for the use of their facilities and generous time and effort:

- Dr. Carl Stahle, Goddard Space Flight Center, USA: for fabricating the CdZnTe drift strip detectors used in this thesis.
- Dr. Mikael Jensen and Dr. Holger Jensen, Cyclotron Unit at Copenhagen University Hospital, Denmark: for assistance and use of the cyclotron and their valuable help for the irradiation experiment of the CdZnTe drift strip detector performed with 30 MeV protons.
- Dr. Fiona Harrison and Dr. Aleksey Bolotnikov, Space Radiation Labaratory, California Institute of Technology, Los Angeles, USA: for generous supply of data from the prototype HEFT CdZnTe pixel detector and for the use of their facility resources to make an X-ray scan of the CdZnTe drift strip detector.

Finally, I would especially like to thank my wife Sevim Kuvvetli for her patience and support and my parents Kadir Kuvvetli and Emine Kuvvetli and my sister Aysegul Kuvvetli for their support and encouragement throughout my studies.

Publications

The present work has so far resulted in the following publications:

[I] *Radiation Damage Effects in CZT Drift Strip Detectors*
I. Kuvvetli, C. Budtz-Jørgensen, U. Korsbech, H.J. Jensen.
Accepted for publication in SPIE proc. vol 4851 , **in press**, 2002.

[II] *Radiation Damage Measurements on CdZnTe Drift Strip Detectors.*
I. Kuvvetli, C. Budtz-Jørgensen, U. Korsbech, H.J. Jensen.
Accepted for publication in Nuclear Instruments and Methods in Physics Research - Section A, **in press**, 2002

[III] *The Response of CZT Drift-Strip Detector to hard X and Gamma Rays*
I. Kuvvetli, C. Budtz-Jørgensen, L. Gerward, C. M. Stahle.
Radiation Physics and Chemistry., **vol. 61**, 2001, p. 457-460.

[IV] *The X-ray Imager on AXO.*
C. Budtz-Jørgensen, I. Kuvvetli, N.J. Westergaard, P. Jonasson, V. Reglero, C.J. Eyles.
Astrophysics and Space Science., **vol. 276**, 2001, p. 281-289.

[V] *New Results for the CZT Drift-Strip Detector.*
I. Kuvvetli, C. Budtz-Jørgensen, L. Gerward, C. M. Stahle.
Accepted for publication in Space Astrophysics Detectors and Detector Technologies proceedings., **in press**, 1999.

[VI] *Development of large area CZT detector systems.*
I. Kuvvetli, C. Budtz-Jørgensen, N.J. Westergaard, , P. Jonasson, M.A.J. van Pamelen, V. Reglero, C. Eyles, T. Neubert.
SPIE Proceedings., **vol. 3765**, 1999, p. 370-378.

[VII] *Dual-purpose camera for terrestrial x/gamma observation.*
N. J. Westergaard, C. Budtz-Jørgensen, I. Kuvvetli, P. Jonasson, T. Velasco, J. Luis Requena, V. Reglero, C. Eyles and T. Neubert.
SPIE Proceedings., **vol. 3750**, 1999, p. 557-567.

[VIII] *Development of CdZnTe X-ray detectors at DSRI.*
M.A.J. van Pamelen, C.Budtz-Jørgensen and I. Kuvvetli.
Nuclear Instruments and Methods in Physics Research A., **vol. 439**, 2000, p. 625-633.

[IX] *Effects of Bulk and Surface Conductivity on the Performance of CdZnTe Pixel Detectors*
Aleksey E. Bolotnikov, C. M. Hubert Chen, Walter R. Cook, Fiona A.

Harrison, Irfan Kuvvetli and Stephen M. Schindler.
Nuclear Science, IEEE transaction., **vol. 49**, No. 4, 2002, p. 1941-1949.

[X] *Development of Drift-Strip Detectors Based on CdZnTe*
V. Gostilo, C. Budtz-Jorgensen, I. Kuvvetli, D. Gryaznov, I.I. Lisjutin, A. Loupilov.
Nuclear Science, IEEE transaction., **vol. 49**, No. 5, 2002.

Abstract

This work covers a comprehensive investigation of the issues confronting radiation damage in CdZnTe drift strip detectors planned for use as space instrumentation. Five main problems requiring investigation are identified and addressed including requirement specification with particular emphasis on device material properties, particle induced radiation damage, energy resolution improvement, noise minimization, and electron sensitive detector geometry.

This thesis reports on experimental studies of the radiation damage effects of a 2.7 mm thick CdZnTe drift strip detector exposed to 30 MeV protons in order to describe the effect on the electron trapping characteristic of the material. The experimental studies, reported on this thesis, have been performed at DSRI, in collaboration with the cyclotron facility at Copenhagen University Hospital. The detector characteristics were evaluated after exposure to a number of fluences in the range from 2×10^8 to $60 \times 10^8 p^+/cm^2$. Even for the highest fluences, which had a dramatic effect on the spectroscopic performance, the detector was recovered after an appropriate annealing procedure. The radiation damage was studied as a function of depth inside the detector material. A numerical model that emulates the physical processes of the charge transport in the CdZnTe detector was used to derive the electron transport property as a function of fluence.

Contents

Introduction

Contemporary semiconductor detectors are used in a large variety of fields in science and technology, including nuclear physics, elementary particle physics, optical and X-ray astronomy, medicine, and material testing. For the specific field X-ray astronomy, the next generation of X-ray astrophysics missions will seek to extend the energy range beyond the current limit of about 10 keV studied by ongoing X-ray missions such as ASCA, CHANDRA and XMM. The exploration of the 10 keV to 100 keV band, however, necessitates both advances in the spectral and imaging capabilities of detectors based on semiconductors as well as on the capabilities on X-ray imaging optics.

The importance of the room temperature semiconductor radiation detectors

The material properties such as high quantum efficiency, no requirement for cooling to cryogenic temperatures are needed in relation to space application. Also providing a low cost, large area material is preferred. Detectors combined with modern electronics are ideally suited for instrument in a small-sized satellite with minimum of power consumption. The detector materials that provide the best energy resolution require cryogenic temperature for operation. This requirement is a drawback for a long time space mission.

Over a past few decades, considerable effort has been invested in developing a range of compound semiconductors for use as photon and charged particle detectors. Tab. 1 shows material properties of some of the selected material used as room temperature semiconductor detectors [1]. The key material requirements for the compound semiconductors are: high effective atomic number to provide sufficient stopping power, wide enough band-gap to ensure operation at room temperature, and material uniformity in spatial and spectral response. It is also a requirement that the materials have excellent charge carrier transport properties. Some of the compound semiconductor materials, which moderately fulfil these requirements, are GaAs, CdZnTe, CdTe, HgI_2, PbI_2 and TlBr.

Research have been conducted to provide a background and practical knowledge about the room-temperature semiconductor detector material science, detector design, manufacturing technologies, as well as readout microelectronics design, testing procedures and performance evaluation of imaging devices and systems. There are numerous articles and books written in the past few years

Material	$Cd_{0.9}Zn_{0.1}Te$	CdTe	Ge^*	Si	GaAs	HgI_2	PbI_2	TlBr
Atomic number, Z	48,30,52	48,52	32	14	31,33	80,53	82,53	81,35
Average Z	49.1	50	32	14	32	62	62.7	58
Density, ρ_d (g/cm^3)	5.78	5.85	5.33	2.33	5.32	6.4	6.2	7.56
Band gab E_g @ RT (eV)	1.572	1.44	0.67	1.12	1.43	2.15	2.32	2.68
Fano factor, F	0.1		0.063	0.085	0.138	0.12		0.14
Dielectric constant ε_s	10.9	11	16	11.7	12.8	8.8		
Ionization energy w (eV)	4.64	4.43	2.96	3.62	4.2	4.2	4.9	6.5
$1/e$ abs. depth (mm)@ 100 keV	1.01	≈ 1	3.51	23.19	3.46	0.46		0.32
Bulk Resistivity ρ (Ωcm)	3×10^{10}	10^9	50	$< 10^4$	10^7	10^{13}	10^{12}	
Electron mobility μ_e (cm^2/Vs)	1000	1100	3900	1400	8000	100	8	6
Electron lifetime τ_e (s)	3×10^{-6}	3×10^{-6}	$> 10^{-3}$	$> 10^{-3}$	10^{-8}	10^{-6}	10^{-6}	2.5×10^{-6}
Hole mobility μ_h (cm^2/Vs)	50-80	100	1900	480	400	4	2	
Hole lifetime τ_h (s)	10^{-6}	2×10^{-6}	10^{-3}	2×10^{-3}	10^{-7}	10^{-5}		
$\mu\tau_e$ (cm^2/V)	$(3-5) \times 10^{-3}$	3.3×10^{-3}	> 1	> 1	8×10^{-5}	10^{-4}	8×10^{-6}	
$\mu\tau_h$ (cm^2/V)	5×10^{-5}	2×10^{-4}	> 1	≈ 1	4×10^{-6}	4×10^{-5}		2×10^{-5}

Table 1 Comparison between semiconductor detector material properties. Data are taken from ref. [1] and [2]. The electrical properties at a low temperature (e.g., room temperature). *) The operation temperature for Ge is cryogenic.

as a result of these research.

CdZnTe X-ray and gamma ray detectors for space application

Compared to established Si and Ge, CdZnTe semiconductors are attractive, since their high average atomic number (close to 50) ensures a high sensitivity to hard X- and gamma rays. The photo absorption process is dominant for energies up to 100 keV. Another advantage, is that CdZnTe detectors operate at room temperature. However, present technology does not allow CdZnTe crystals to be produced with the same high charge collection efficiency as Si and Ge. In particular, this is true for the collection of the positive charge carriers[1] (holes). The trapping probability of positive charges is higher than the trapping probability of negative charges (electrons). The holes have a low transport property[2] $\mu\tau_h$ compared to the electrons in CdZnTe material. Consequently, CdZnTe detectors generally have a spectral performance which is degraded compared to the theoretical Fano-limited resolution[3]. This degradation is most severe at high energies (> 50 keV) where absorption takes place deeper below the detector surface such that the holes with their low mobility will be collected inefficiently. Even for the best CdZnTe material available, the detector response will therefore suffer from broad tails, which become more pronounced with increasing photon energy.

Various methods already exist to diminish the effects caused by hole trapping. The methods can be divided into two groups: The first group of methods is based on being able to distinguish the events with a large contribution of holes and reject them. Examples of the methods can be the rise-time discrimination [3], and the dual shaping time [4]. Employing these techniques for most CdZnTe detectors may lead to a large loss of photo peak efficiency. The second group of methods is based on reducing the contribution from holes to the signal by fabricating detector and contact configurations that differ from the commonly used planar detectors. The common factor for these different contact configurations is their ability to make the collected charge dependent primarily of the electron-induced charge near the anode. Therefore leading

[1] The vacant energy state left in the valance band after an electron in the valance band gain energy to jump to conduction band is called a *hole* and it behaves like a positive charge carrier with the same charge as an electron, but of opposite sign. These positive charges (holes) are "moving" when the vacant state recombine with electron(s) from a neighbor atom leaving that atom as positively charged.

[2] The transport properties of charge carriers within the semiconductor material is determined by the product of their mobility μ and charge lifetime τ, the average time that carrier can survive before it is trapped. The $\mu\tau$ product is related to the spectral performance of a semiconductor detector material.

[3] Fano-factor limited energy resolution is explained in Sec. 1.4.

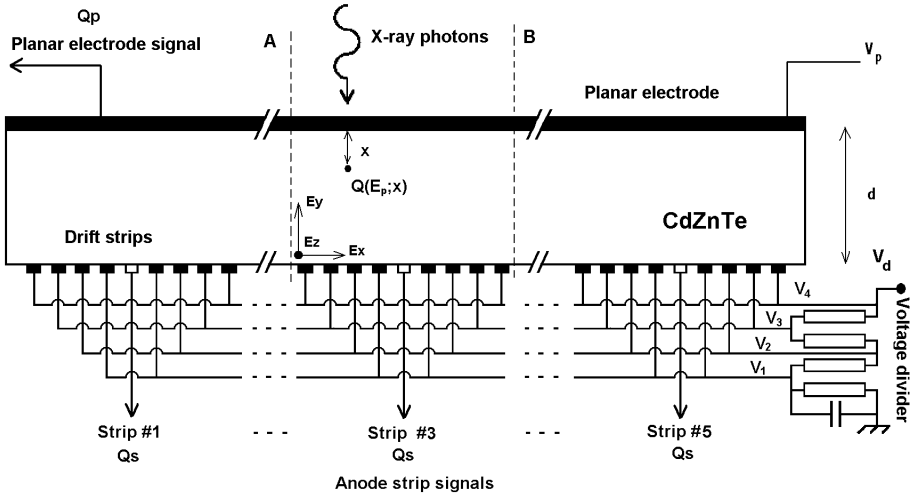

Figure 1 Cross-section of a detector based on the Drift Strip Method (DSM). A drift strip detector cell is shown between dashed lines marked with "A" and "B". The drift strip electrodes and the planar electrode are biased in such that the electrons move to the anode strips.

to independence on the position of interaction. An example of reducing the sensitivity to the contribution of holes is the coplanar grid technique [4]. This is achieved by subtracting the signals on two sets of coplanar strips yielding a signal that is nearly independent of holes. Applying this coplanar grid technique to CdZnTe detectors require complex read-out electronic, which is not feasible if not impossible to use in a large area detector arrays.

Development of CdZnTe X-ray detectors at Danish Space Research Institute (DSRI)

In 1996, the Danish Space Research Institute (DSRI) initiated a research program to develop CdZnTe X-ray and gamma ray detectors employing micro strip readout techniques for space applications. The research has resulted in a technique with the use of micro strip electrodes [5] the so called Drift Strip Method (DSM) at DSRI. In 1987, J. Kemmer and G. Lutz introduced a detector concept which was based on a single-sided strip electrode structure configured as drift detector on one side and a planar electrode on the other side of a semiconductor material. Details can be found in [6] and [7]. The DSM is based on this approach using CdZnTe as a detector material. A significant improve-

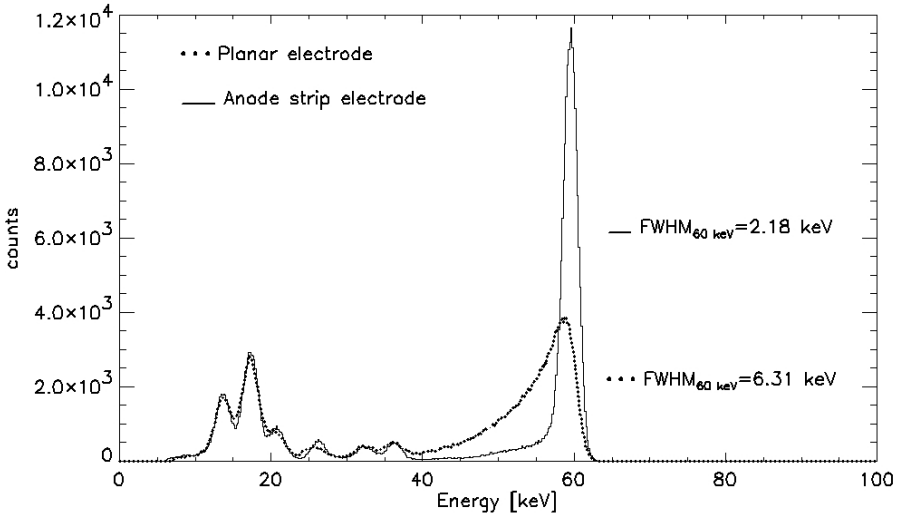

Figure 2 ^{241}Am spectra obtained with a 2.7 mm thick CdZnTe drift strip detector. The spectra obtained with the planar electrode (dotted line) and with the anode strip (solid line). The applied bias voltages are Vp=-230 V and Vd=-80 V. The operating temperature is 22 ^oC.

ment of the energy response was achieved when operating the detectors as a drift detector instead of a conventional planar detector. In the following years, many prototype of CdZnTe drift strip detector were tested and the results were presented in journals.

A short description of the DSM is as follows, and an elaborated explanation is given in Chapter 3. The DSM is based on modified and geometrically weighted electrode design. Due to modified electrode design, the weighting field within the detector is changed so the anode strip electrode is more sensitive to electrons and less sensitive to holes. A detector applied DSM structure is shown in Fig. 1. The DSM structure consists of a planar electrode on one side and a number of strips on other side. A drift detector cell consists of a number of drift strip electrodes and one anode readout strip electrode. The drift strip electrodes and the planar electrode are biased such that the electrons with their transport properties $\mu\tau_e$ are drifted to the anode strip. The drift strips provide an electrostatic shield so that the movement of the holes only will induce a rather small signal at the anode strip. Thus the sensitivity to the trapping of holes is strongly reduced for the anode strip whereas the planar

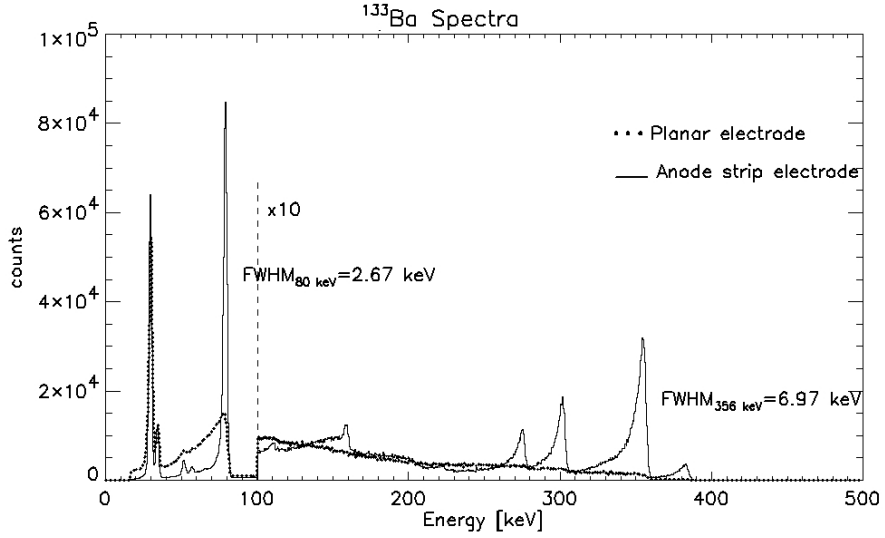

Figure 3 ^{133}Ba spectra obtained with planar electrode (dotted line) and the anode strip (solid line). The spectra are scaled above 110 keV with a factor of 10 in order to show more detail. The applied bias voltages are Vp=-300 V and Vd=-80 V. The operating temperature is 22 ^oC. The shaping time is 1 μs for all shaping amplifiers.

electrode sensitivity to holes is unchanged. Collection of charge carriers induce a signal on the collecting electrodes whose amplitude is proportional to the energy of the incident photon. The result of the incomplete charge collection, or charge trapping will reduce the detected charge pulses. This reduction will cause the charge pulse signal to be assigned an energy of the photon lower than its true energy. These reduced energy measurements appear as a "tail" on the low-energy side of the detected peak on the spectrum.

The drift strip method (DSM) applied to the CdZnTe detectors leads to a energy resolution improvement.

The improvement of the energy response of the detector when operating it as a drift detector is shown in Fig. 2 (^{241}Am) and Fig. 3 (^{133}Ba). Here the full drawn lines show the spectra obtained by the anode strip and the dotted lines show the spectra obtained by the planar electrode. The spectra (obtained by the anode strip and the planar electrode) were recorded simultaneously and in coincidence[4]. For the planar electrode, the "tail" on the low-energy side

[4]Coincidence is a detection mode (or technique) used to produce a simplified spectrum from certain types of detector systems. These systems consist of two (or more) independent

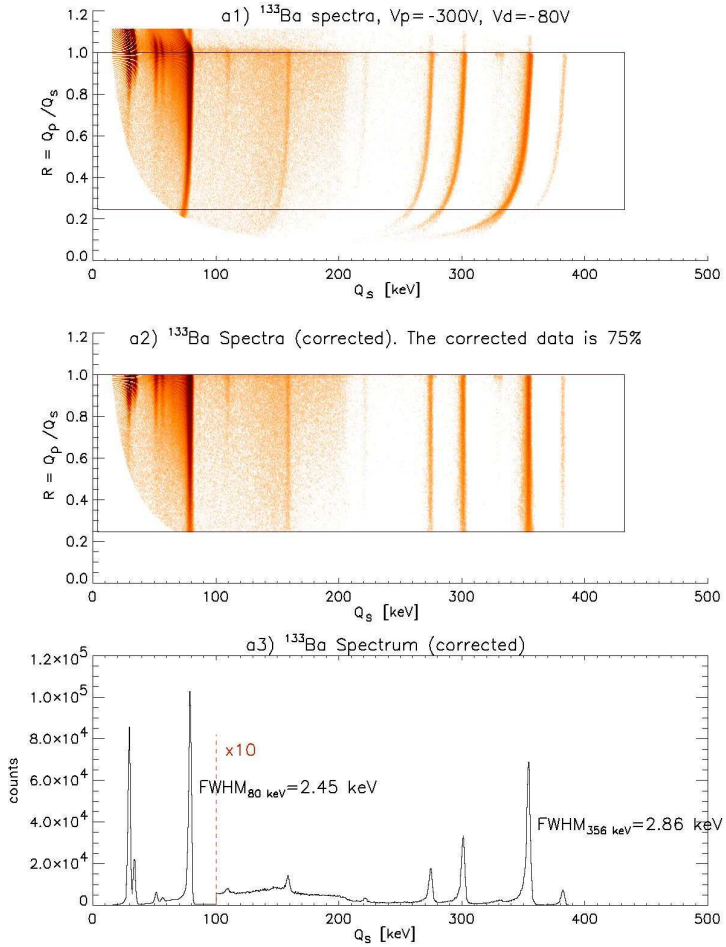

Figure 4 Bi-parametric distribution is shown in a1). The corrected bi-parametric distribution of ^{133}Ba contains all events ($\sim$ 75 %) with R-values distributed between 0.25 and 1.0 and is shown in a2). The relation between the ratio R=Qp/Qs and Qs is used to correct Qs for electron trapping and none-ideal weighting potential effect. More detail is given in Chapter 3. The corrected spectrum of ^{133}Ba is shown in a3). The spectrum is scaled with a factor of 10 above the 110 keV in order to show more details. The applied bias voltages are Vp=-300 V and Vd=-80 V. The operating temperature is 22 ^{o}C. The shaping time is 1 μs for all shaping amplifiers.

of the ^{241}Am 60 keV line is due to hole trapping. For the anode strip, the tailing was strongly reduced and the energy resolution was 2.18 keV (FWHM) at 60 keV, which is comparable with the electronic noise of 2.05 keV (FWHM) as measured with a pulse generator.

Degradation of the energy response due to hole trapping becomes more pronounced with increasing energy. This can be seen from the planar electrode spectrum of ^{133}Ba, shown in Fig. 3. The lines above 80 keV are hardly visible. For the anode strip, all energy lines of the ^{133}Ba were detected. The energy resolution was 2.67 keV(FWHM) and 6.97 keV (FWHM) for the 80 keV and 356 keV line, respectively.

The resolution could be improved further using a correction method described by Budtz-Jørgensen *et al.* [5]. The method is based on a "depth"[5] information technique using the effect of the hole trapping phenomena. The depth of photon interaction between the planar electrode and the anode strip electrode is obtained from the ratio R between the planar electrode signal Q_p and the anode strip signal Q_s. The depth information has a value $R \approx 1.0$ for interactions close to the planar electrode or detector surface because the planar and the anode strip electrode signals are due to electrons movement. It has a value $R \approx 0.0$ for interactions near the strip electrodes because the signals are due to holes movement. In practice, the correction can be obtained from the bi-parametric distribution of "depth" and the anode strip signal. Fig. 4 shows the corrected spectrum. The spectrum contains all events ($\sim$ 75 %) with R-values distributed between 0.25 and 1.0. Energy resolution of 2.45 keV (FWHM) and 2.86 keV (FWHM) are now obtained for the 80 keV and 356 keV line, respectively. The depth information can also be used to discriminate between gamma rays and charged particles since their depth distributions are very different.

Although the spectroscopic properties of the drift strip detectors are almost independent of material hole transport properties, they are of course very dependent on the electron collection efficiencies and, especially, material with fluctuating electron transport properties will result in degraded detector performance. A serious concern for space use of the CdZnTe drift strip detectors is therefore, the effect of particle induced radiation damage, which is known to affect the electron trapping property of the CdZnTe material, therefore, it affects the electron collection efficiency of the detector. Chapter 4 focuses on ground-based testing by exposing a 2.7 mm thick CdZnTe drift strip detector

detectors. Each detector produces separate signals for the event. In coincidence, only those events are recorded and counted for the event signal produced simultaneously in at least two of the detectors.

[5]The effect of the severely trapped holes causes the planar electrode signal strongly influenced by the photon interaction "depth" position whereas the anode strip signal is almost independent to it. This is elaborated in details in Chapter 3.

to 30 MeV protons and the subsequent predictions of the detector performance degradation as a function of the proton fluence.

The aim of this work

The main goal of this research was to investigate CdZnTe drift strip detector systems for space application. An important part of the work was to test the influence of the radiation damage induced by the energetic charged particles and to understand the effect of the radiation damage on the detector performance. Following objectives are considered in order to achieve the goal of this research:

- A set-up for irradiation experiment with necessary hardware and software should be designed and constructed.
- A model describing the physical processes for the CdZnTe drift strip detector should be developed.
- The model should be used to explain the experimental data from the detector. In the model the equations describing the response of CdZnTe drift strip detector with complicated geometric electrode structures require the use of numerical methods. Therefore the electric field and the potential distribution should be calculated within the CdZnTe drift strip detector.
- A data analyzing software using the model to fit the experimental data should be developed and used in order to determine the electron transport property for the irradiated CdZnTe drift strip detector.
- The damage profile within the irradiated CdZnTe drift strip detector should be determined.
- A compact low noise low power Application Specific Integrated Circuit (ASIC) readout electronic for CdZnTe drift strip detector should be investigated.

Chapter 1. Here, the basic semiconductor detector physics is reviewed to the extent which is necessary to understand the results of this thesis. Also, towards the end of the chapter, a series of mathematical descriptions of the physical processes used for computer simulations of a CdZnTe drift strip detector equivalent to the ones being experimentally studied here will be presented.

Chapter 2. Here a more thorough review of the CdZnTe material properties is given, with emphasis on the current status of commercial production of

crystals. This will partly be illustrated by experimental measurements done by others. An X-ray scan experiment performed on a prototype detector in order to investigate the effect of grain boundaries to detector performance is presented.

Chapter 3. The CdZnTe drift strip deetector was extensively examined with its practical applicability as a room temperature X-ray and gamma ray detector with space applications in mind. The drift strip method mechanism are briefly reviewed, and experiments performed on prototype detectors are presented. Furthermore, the fundamentals of the depth information and signal correction are discussed. The results of this chapter are contained in **Articles III, IV, V, VI** and **VIII**.

Chapter 4. A 2.7 mm thick CdZnTe drift strip detector was bombarded with energetic protons (30 MeV) in order to measure the radiation damage effect in the detector . The radiation damage experiment and results are presented. In this chapter, experimental evidence of detector performance degradation is presented and explained with the aid of computer simulations of the detector model. The results of this chapter are contained in **Article I and II**.

Appendix A. A 2D position sensitive pixel detector and readout electronics were designed. Drift strip method was applied to the contact geometry of this detector. It was planned to use an Application Specific Integrated Circuit (ASIC) chip from eV-products as a read-out electronic for the CdZnTe drift pixel detector. The detector system was not characterized as the detector was not received in time. In this chapter, only the pixel electrode geometry and the noise characteristic of the ASIC chip from eV-products are presented.

Appendix B. For the irradiation experiment, software and hardware were developed to ensure correct fluences for the detector. A sort of "user guide" to the irradiation experiment is given in this appendix to help others to use the set-up for similar irradiation experiments.

Appendix C. The data from the calculation of the damage profile using the computer software TRIM and the data from the calculation of the stopping range of 30 MeV protons in the CdZnTe using the computer software SRIM are given in this appendix.

1

Basic Radiation Detector Physics

Examining the radiation, emitted or absorbed by matter, can enhance our understanding of the nature of matter, its chemical composition, temperature, density, and motions. These properties and many others can be measured by instruments employing radiation interaction with matter, e.g., scattering of radiation and/or transitions between the energy levels of atoms or molecules in matter. This chapter presents the radiation types, how radiation conveys information by interacting with matter and what techniques are to be used to collect and measure radiation. However, this chapter will focus on the theory relevant to the thesis topic. It is not the goal to cover the wide range of the theory on this subject. Thus, the chapter will concentrate on the X-ray and gamma ray radiation types and their interaction with semiconductor detector material.

1.1 Introduction and basic concepts

What is the radiation? How does the radiation interacts with matter? How does a radiation detector work? What does a radiation detector measure? What is the magnitude of the induced charge? These and many other questions will be discussed shortly in following pages. Basic semiconductor physics is treated in many excellent textbooks (e.g., [8], [9]), to which the reader is referred. These references focus on books which have become popular in the field. The specific goal of this section is to gain a brief and basic framework

for the reader to be able to understand the semiconductor detectors and their detection mechanism. The following section is based on books by G. Lutz [7], T.E. Schlesinger [1] and G. Knoll [10].

1.2 Radiation

Radiation is energy moving through space in the form of electromagnetic waves (gamma rays, x-rays, micro waves or ultraviolet light) or as particles (alpha particles, protons or beta particles). Most of these radiation types can be observed in accelerator experiments or at radioactive decay of atomic nuclei. X-rays or micro waves can easily be created in a laboratory. This project deals with, X-rays and soft gamma rays. In the energy spectrum, X-rays are situated in the range from 1 keV to 100 keV, while gamma rays generally are situated between 100 keV and 10 MeV. The traditional unit for a measurement of radiation energy is the electron volt or eV, defined as the kinetic energy gained by an electron by its acceleration through a potential difference of 1 volt. In general, radiation may broadly be divided into two categories:

- Ionizing radiation including beta particles (electrons and positrons), protons, alpha particles, X-rays, gamma rays, neutrons and fission fragments.

- Non-ionizing radiation which includes microwaves, laser light and radio frequency radiation.

1.2.1 Ionizing radiation

Ionizing radiation is radiation that is able to ionize atoms when passing through matter. Ionizing an atom occurs when radiation with enough energy removes bound electrons from their orbits leaving the atom charged. The most common types of ionizing radiation are:

- **Alpha particles (charged):** are among the most massive types of radiation. They are nuclei of helium, and therefore, have 2 protons (positive charge) and 2 neutrons (no charge). Alpha particles are emitted during the decay of unstable heavy atomic nuclei.

- **Protons (charged):** (positive charge) can be accelerated to a high energy with a particle accelerator. A Proton is an elementary particle that is identical with the nucleus of a hydrogen atom. In space, the Van Allen

belts radiation [1] consist principally of electrons of up to a few MeV energy and protons of up to several hundred MeV energy with high fluence rates.

- **Beta particles (charged):** are electrons (negative charge) or positrons (positively charged electrons) and therefore have a mass much lower than alpha particles and protons. The negative betas come from nuclei that have too many neutrons, while the positive betas are generated from nuclei having too many protons. In space intense fluence rates of energetic electrons are common.

- **Neutrons (uncharged):** are neutral particles originating from the nucleus of an atom during nuclear reactions.

- **Gamma rays (uncharged):** are electromagnetic radiation similar to radio waves, visible light, and X-rays, except that they have much higher energies (higher frequency or shorter wavelength). After a radioactive decay (α and β), the new nucleus often has an excess of energy and this is usually released by the emission of gamma rays. Gamma rays are transmitted in small individual quantities of energy known as photons and in some ways they behave more like particles than as waves. The time delay between the decay of a radioactive atom and the gamma-ray emission is so small that for most practical purposes they may be considered to occur simultaneously.

- **X-rays (uncharged):** are also electromagnetic radiations, similar to the gamma rays. X-rays originate in the orbital electron field surrounding the nucleus. This process takes place in its simple way when an electron is knocked out from its orbit, leaving the atom in an unstable state. Another electron of a higher energy falls down, filling the place of the missing electron and the energy difference between the two energies is released. In addition, the high speed electrons may lose energy in the form of X-rays when they quickly decelerate upon striking a material. This is called Bremsstrahlung (or Breaking) Radiation.

[1] The space radiation environment is principally composed of naturally occurring charged particles trapped in the Earth's magnetic field. This region is known as the Van Allen belts. The Van Allen radiation is usually responsible for most of the ionizing dose damage to electronics and materials, though energetic solar particles can also be a significant source during solar storms. The trapped particles in the Earth's magnetic field are constantly in motion. Their motions in the field consist of a gyration about field lines, a bouncing motion between the magnetic mirrors found near the Earth's poles, and a drift motion around the magnetic field lines [11].

1.2.2 Non-ionizing radiation

Non-ionizing radiation is electromagnetic radiation ranging from extremely low frequency (ELF) radiation to ultraviolet light. Non-ionizing radiation does not have enough energy to remove bound electrons from their orbits during an interaction with the atom.

1.3 Interaction of radiation with detector materials

Energetic photons as hard X-rays and gamma rays interact with matter mainly by four basic processes:

- Elastic scattering, which is a change of photons path without changing its energy.
- Photoelectric absorption where the photon disappear after transferring all its energy to a photoelectron.
- Compton scattering in which some fraction of the photon energy is transferred to a free electron in the material. The path of the photon is changed.
- Pair production in which the photon energy is spontaneously converted into a electron-positron pair.

Only three of the four types play an important role in radiation measurements. These are photoelectric absorption, Compton scattering and pair production. All these processes lead to a partial or complete transfer of the photon energy to electron energy.

1.3.1 Elastic scattering

In the case of elastic scattering, the energy of the incident photon is not changed, rather the photon is merely deflected out of its path. This process does not deposit energy in the detector and is without interest here.

Each of the following three processes involves the deposition of all or part of the energy of the incident photon to matter for example within the detector volume.

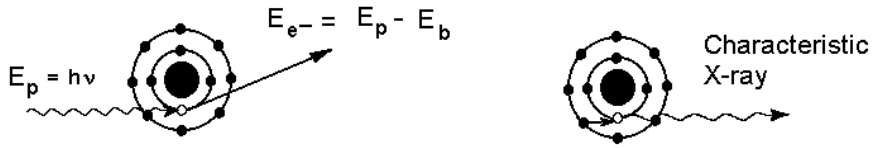

Figure 1.1 Photoelectric absorption. The photon is absorbed and the energy is transferred to an orbit electron of the atom. The vacancy that is created in the electron shell as a result of photoelectron emission is quickly filled by electron rearrangement. In the process, the binding energy of the electron is emitted either in form a characteristic X-ray or an Auger electron.

1.3.2 Photoelectric absorption

Photoelectric absorption is, in most cases, the ideal process for detector operation. All of the energy of an incident photon is transferred to one of the orbital electrons of the atoms within the detector material usually to an electron of the K-shell. This photoelectron will have a kinetic energy equal to that of the incident photon energy minus the atomic binding energy of the ejected electron.

$$E_{\text{e-}} = E_{\text{p}} - E_{\text{b}} \tag{1.1}$$

where $E_{\text{e-}}$ is the photoelectron energy after collision, E_{b} is the binding energy of the photoelectron and E_{p} is the photon energy. A sketch of the interaction is given in Fig. 1.1.

The atom with a missing inner-shell electron emits a characteristic X-ray photon[2] after an outer-shell electron is transferred to the incomplete inner shell. This X-photon may interact with another atom by means of one or more processes until it loses all its energy or escapes from the material. Instead of emitting a X-ray photon the atom may emit an Auger electron[3] with a characteristic energy [10]. Auger electrons are of very low energy and can only travel a short distance within the matter. The Auger electron can escape from the material only when the absorption of the incoming photon takes place very

[2]The emitted radiation is known as fluorescence. These fluorescent X-rays are unique fingerprint of the kind of atom that produces the fluorescence.

[3]Auger electron, named after the French physicist Pierre Auger who first discovered the process.

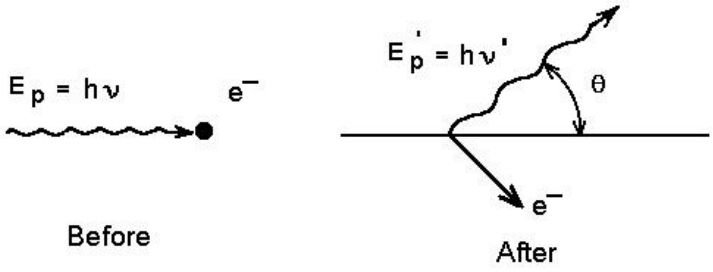

Figure 1.2 Compton scattering. The result of a Compton scattering is a recoil electron and a scattered photon. The incident photon energy is divided between the photoelectron and the scattered photon dependent on the scattering angle.

close to the surface.

In a semiconductor material as well as in other materials, the photoelectron will lose its kinetic energy via coulomb interactions with the semiconductor electrons, creating many electron-hole pairs.

1.3.3 Compton scattering

Compton scattering is a collision between an incident photon and an orbital electron. The result is the creation of a recoil electron and a scattered photon. The incident photon energy is divided between the recoil electron and the scattered photon dependent on the scattering angle θ [10]. A sketch of the interaction is given in Fig. 1.2.

The scattered photon energy in terms of its scattering angle is given by:

$$E'_{\mathrm{p}} = \frac{E_{\mathrm{p}}}{1 + (E_{\mathrm{p}}/m_0c^2)(1 - \cos\theta)} \tag{1.2}$$

where m_0c^2 is the rest mass energy of the electron. The kinetic energy of the recoil electron is therefore:

$$E_{\mathrm{e}^-} = E_{\mathrm{p}} - E'_{\mathrm{p}} \tag{1.3}$$

In normal circumstances, all scattering angles will occur in the detector. Therefore, a continuum of energies can be transferred to the electron, ranging

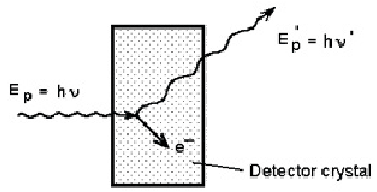

Figure 1.3 Multiple scattering neglected. The Compton scattered photon here escapes from the detector crystal.

from:

$$\begin{array}{c} \theta \cong 0 \\ E'_{\rm p} \cong E_{\rm p} \\ E_{\rm e\text{-}} \cong 0 \end{array} \tag{1.4}$$

to

$$\begin{array}{c} \theta = \pi \\ E'_{\rm p}|_{\theta=\pi} = \frac{E_{\rm p}}{1+(2E_{\rm p}/m_0c^2)} \\ E_{\rm e\text{-}}|_{\theta=\pi} = E_{\rm p}\ \frac{2E_{\rm p}/m_0c^2}{1+(2E_{\rm p}/m_0c^2)} \end{array} \tag{1.5}$$

After a Compton scattering in the detector material, the scattered photon either interacts with the detector or escapes from it. Two situations are considered.

1) Multiple scattering neglected.

After the Compton scattering, the scattered photon leaves the detector material as illustrated in Fig. 1.3. The energy of the escaped photon will be lost.

The recoil electron will loose its energy through the creation of electron-hole pairs in the detector and contribute to the Compton continuum recorded by the detector, as it is illustrated in an example in Fig. 1.4.

In Fig. 1.4, the gap between the maximum Compton recoil electron energy and the incident photon energy is given by:

$$E_{\rm c} \equiv E_{\rm p} - E_{\rm e\text{-}}|_{\theta=\pi} = \frac{2E_{\rm p}}{1+(2E_{\rm p}/m_0c^2)} \tag{1.6}$$

If the incident photon energy is large i.e., $E_{\rm p} \gg m_0c^2/2$, then this energy difference approaches a constant value given by:

$$E_{\rm c} \cong m_0c^2/2 \quad (= 0.256\ MeV) \tag{1.7}$$

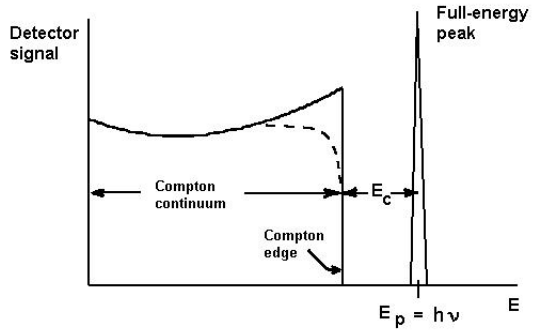

Figure 1.4 A continuum of energies can be transferred to the Compton electron depending on the scattering angle, ranging from $\theta = 0$ to $\theta = \pi$. Here the electrons are assumed initially free or unbound. In actual detector materials, the binding energy of the electron can have a measurable effect on the shape of the Compton continuum at lower photon energies. This effect can be a rounding-off of the rise in the continuum near the Compton edge (dashed line) [10].

As an example, in this work, ^{137}Cs radioactive source was used as a calibration and test source for the detectors. The highest photon energy from the source is 661.6 keV. The energy difference E_c is calculated as:

$$E_c = \frac{661.6\ keV}{1 + (2 \times 661.6\ keV/511\ keV)} \simeq 184.3\ keV) \tag{1.8}$$

2) Multiple scattering occurs.

In the case of multiple scattering, the Compton scattered photon interacts also with the detector, either by additional Compton scatterings or by a photoelectric process. In this way all the energy of the incoming photon will end up in the detector crystal. These multiple scattering will contribute to the full energy peak signal at E=E_p , see Fig. 1.4.

1.3.4 Pair production

For photon energies greater than twice the rest mass energy of the electron (1.022 MeV) pair production may occur and will actually be the dominant type of interaction at energies above several MeV. In this type of interaction, the energy of the incident photon is converted to an electron-positron pair.

Afterwards the positron annihilates with an electron producing two 511 keV photons. Unless these photons are reabsorbed in the detector, the pair production process will not contribute to the full energy peak. The highest photon energy used for the project is a calibration source ^{137}Cs (661.6 keV), therefore pair production is not of interest in this thesis.

The probability of the three types of photon interaction with a detector material of atomic number Z is proportional to Z^n $(4 < n < 5)$ for photoelectric interactions, Z for Compton scattering, and Z^2 for pair production [1].

For all these interaction processes explained previously, the attenuation of the intensity of a beam of photons as they pass through an absorbing medium follows an exponential law, the Beer's law:

$$I(x) = I_0 \exp(-\xi x) \tag{1.9}$$

where I_0 is the incident photon intensity in s^{-1}. I(x) is the intensity of primary photons at a depth x in cm in the absorber, and ξ is the linear attenuation coefficient in cm^{-1}. In order to avoid a confusion between the charge carrier mobility and the linear attenuation coefficient, the symbol ξ is used here instead of the μ which is normal used for the linear attenuation coefficient in literature.

For radiation measurements, the important feature of all of these interactions is the electron-hole pairs, that are generated in a detector and can be detected by an external electronic circuit. For X-rays and gamma rays the number of electron-hole pairs is almost proportional to the energy of the incident photon deposited in the detector. The proportionality constant, the mean energy to create an electron-hole pair, depends on the semiconductor material, but is of the order of few eV.

1.4 Basic features of semiconductor radiation detectors

Basically, the operation of any radiation detector depends on the manner in which the radiation to be detected interacts with the material of the detector. The result of the interaction then should be interpreted in order to extract information about the radiation. The interaction should cause a measurable quantity i.e., a change in temperature, a current, a charge or even chemical or nuclear changes in the detector material.

As an example, the X-ray or gamma ray photon interaction with a semiconductor detector material can create a number of electron-hole pairs within the active volume of the detector. These charge carriers (electrons and holes) can be collected to form an electrical current pulse signal by applying a bias

voltage between two electrodes on the surface of the detector. The signal can then be analyzed with the help of an external electronic circuit.

A detector can be used for measuring three different properties of the radiation:

- **Position:** To get an image of the source, by recording in detail the positions of the interactions of the incoming radiation.
- **Energy:** To measure the spectrum of the source i.e., a measurement of the energy deposited by each interacting photon.
- **Time:** To get the timing information, by measuring the time of the interactions accurately.

Radiation detectors are instruments employed in astronomy, medical science, material science and many other fields in which radiation is involved. There are several types of detectors using different kinds of detection methods. The detector type analyzed in this thesis is the X-ray and gamma ray radiation detector based on room temperature semiconductor detector material. The general semiconductor detector theory and detection mechanisms will be shortly presented in this chapter, as they are also valid for the CdZnTe room temperature (compound) semiconductor detector. The basic electrode geometry for semiconductor detectors is the parallel planar electrode geometry. This detector geometry will be explored gradually in order to gain an understanding of the theoretical aspects for how the detectors work.

1.4.1 Ionization energy, detector resolution and the Fano factor

The energy resolution[4] is the most important factor for detectors which are designed to measure the energy distribution of the incident radiation. The resolution is usually given in terms of the *full width at half maximum* (FWHM) of the peak. The FWHM is defined as the energy width of the spectral response to monochromatic radiation energies, at which the number of counts has decreased to half of the maximum.

In a semiconductor detector, a full absorption of a photon with energy E_p can create a number of electron-hole pairs within the active volume of the detector. The number of electron-hole pairs is given by:

$$N_0 = E_p/\omega \tag{1.10}$$

with ω is the mean energy required for creation of an electron-hole pair.

[4]The detector can distinguish between two close lying energies.

For a given radiation energy, the number of electron-hole pairs will fluctuate around a mean value N_0. An estimate can be made of the amount of inherent fluctuation by assuming that the formation of each electron-hole pair follows a Poisson statistic. The variance σ^2 in the number of electron-hole pairs N_0 is given by:

$$\sigma^2 = N_0 \tag{1.11}$$

According to the Poisson distribution, the limiting resolution due to statistical fluctuations is:

$$\frac{\Delta E}{E} = \frac{2.35}{\sqrt{N_0}} \tag{1.12}$$

Careful measurements of the energy resolution of some types of radiation detectors have shown that assumption of Poisson statistic is not correct and R is actually smaller than that calculated from Eq. (1.12) [10]. Statistically, this means that the formation of each electron-hole pair is not independent so that Poisson statistics are not applicable. *Fano* [12] was the first to calculate the variance under this condition and found:

$$\sigma^2 = FN_0 \tag{1.13}$$

with F the Fano factor. The Fano factor has been introduced in an attempt to quantify the departure of the observed statistical fluctuation in the number of charge carriers from pure Poisson statistics [10] and is defined as:

$$F \equiv \frac{\text{observed variance in } N_0}{\text{Poisson predicted variance } (= N_0)} \tag{1.14}$$

From Eq. (1.13), the achievable theoretical Fano factor limited energy resolution is then given by:

$$\frac{\Delta E}{E} = 2.35\sqrt{\frac{F}{N_0}} \tag{1.15}$$

In addition to the inherent statistical fluctuations in the number of charge carriers, two external predominant factors can affect the overall total energy resolution of the detector. The first one is the fluctuations due to electronic noise[5]. The second one is the fluctuations due to trapping of charge carriers in the detector. Then the total FWHM will be the quadrature sum of the FWHM values for each individual source of fluctuation.

$$(FWHM)^2_{total} = (FWHM)^2_{statistical} + (FWHM)^2_{elc} + (FWHM)^2_{trapping} \tag{1.16}$$

[5]The electronic noise due to the input stage of the preamplifier including the capacitance and leakage current of the detector itself.

The electronic noise component to the total energy resolution is independent of energy. It is symmetrical and due to several noise sources arises from the detector, the components and materials used in the input stage of the preamplifier, the placement of the components, and specific parameters of the shaping amplifier.

The statistical noise is proportional to the square root of the energy of the incident radiation. This term also produces a symmetrical broadening of the peak.

The noise component, due to the trapping of charge carriers, is more complex than the other two components. It is highly dependent on interaction position (at higher energies the radiation interaction can occur throughout the detector active volume) due to trapping of carriers. The resulting shape of the peak is dependent on the energy of the incident radiation.

1.4.2 Semiconductor detector

The simple semiconductor radiation detector may consist of a semiconductor detector material between two parallel electrodes (metal contacts). The positive electrode is called the anode, and the negative electrode is the cathode. The basic detector structure is shown in Fig. 1.5. It consists of metal contacts on both sides of the semiconductor material. The common principle of the semiconductor radiation detectors can be described as follows: The incoming radiation generates a photoelectron or a Compton electron. This energetic electron afterwards generates number of electron-hole pair within the detector. An electric field is obtained within the material by applying a bias voltage to the metal electrodes. The electric field separates electron-hole pairs formed by ionizing radiation and collect the carriers via drift movements on the appropriate electrodes. The rapid movement of carriers in the electric field generates a current pulse at the device electrodes. Because of the unique relationship between the energy deposited by the radiation to the number of moving electron-hole pairs generated in the device, and between the induced charge on the electrode, the deposited energy can be obtained from the amplified and converted induced charge. The induced charge on the electrodes is converted to a voltage pulse using a charge sensitive preamplifier and the amplitude of the output voltage signal ideally is proportional to the deposited energy.

1.4.3 Charge collection

The electron-hole pairs generated in the detector can be separated and collected at appropriate electrodes by applying an electric field $\mathbf{E}$. This process is called drift. The drift velocity is proportional with the carrier mobility μ and the

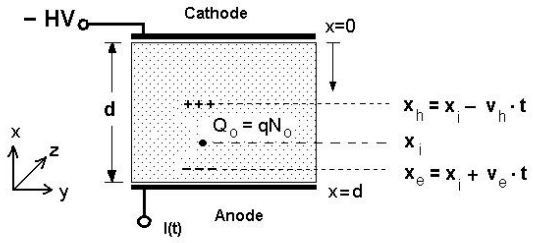

Figure 1.5 Simple detector with parallel geometry and an illustration of the charge carriers' motion. $\mathbf{x}_i$ is the initial position for the generated charges by ionizing radiation. $\mathbf{v}_h$ and $\mathbf{v}_e$ are the drift velocity of the holes and electrons, respectively. $\mathbf{x}_e$ and $\mathbf{x}_h$ are the electron and hole positions after an elapsed time t.

electric field $\mathbf{E}$. The drift velocities of the electrons and the holes are given by:

$$\begin{aligned} \mathbf{v}_e &= \mu_e \mathbf{E} \\ \mathbf{v}_h &= \mu_h \mathbf{E} \end{aligned} \tag{1.17}$$

where $\mathbf{v}_h$ and $\mathbf{v}_e$ are the drift velocity of the holes and electrons, respectively. The electric field $\mathbf{E}$ is the gradient of the scalar potential existing in the device is given by :

$$\mathbf{E} = -\nabla V \tag{1.18}$$

The minus sign shows that the electric field is directed from the region of higher potential to the region of lower potential.

Consider an electron-hole pair originating at $\mathbf{x}_i$. After an elapsed time t, the position of the electrons ,$\mathbf{x}_e(t)$, and holes, $\mathbf{x}_h(t)$, is given by:

$$\begin{aligned} \mathbf{x}_e(t) &= \mathbf{x}_i + t\mathbf{v}_e \\ \mathbf{x}_h(t) &= \mathbf{x}_i - t\mathbf{v}_h \end{aligned} \tag{1.19}$$

where $\mathbf{x}_e$ and $\mathbf{x}_h$ are the position of the electrons and the holes after an elapsed time t. The time required for a charge carrier to traverse the sensitive volume from the interaction point $\mathbf{x}_i$ to the appropriate electrode is called the collection time. The collection time for the electrons is given by:

$$t_{ce} = \frac{|\mathbf{x}_i - d|}{\mu_e \mathbf{E}} \tag{1.20}$$

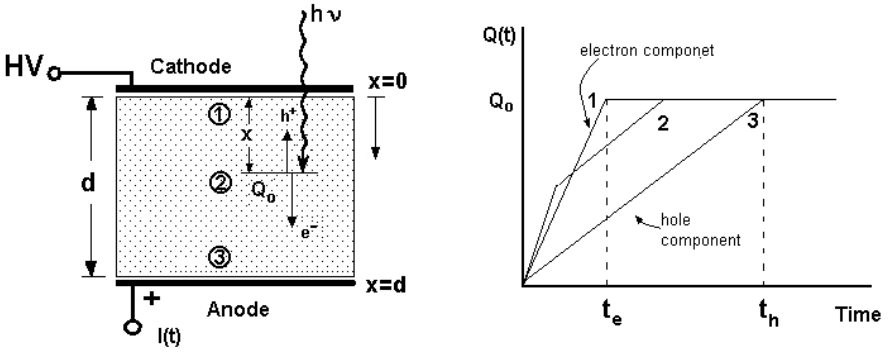

Figure 1.6 Time dependence of the induced signal for three different positions of the electron-hole production in a semiconductor detector. The fast rising part of the signal is due to the electron component of the signal while the slower rise is caused by the holes, as the holes are relatively slow than the electrons.

Where d is the distance between electrodes. The collection time for the holes is given by:

$$t_{ch} = \frac{|\mathbf{x}_i|}{\mu_h \mathbf{E}} \tag{1.21}$$

The time required to traverse the detector thickness d for an electron is given by:

$$t_e = \frac{d}{\mu_e \mathbf{E}} \tag{1.22}$$

and for a hole is given by:

$$t_h = \frac{d}{\mu_h \mathbf{E}} \tag{1.23}$$

The current pulse begins when the charge carriers begin to move. The motion of the charge carriers induces charge on collecting electrodes. The induced charge is time dependent due to the charge mobilities. The time dependence of the induced charge is illustrated in Fig. 1.6 for three different interaction positions within the detector volume. In case 1, the charge is produced very close to the cathode, and so the entire induced signal is due to the motion of the electrons, while in case 2, both the holes and the electrons contribute to the signal. The fast rising part of the signal is due to the electron component of the signal while the slower rise is caused by the holes. In case 3, where the charge is produced very close to the anode, the entire signal is due to the motion of the

holes. The induced signal builds up linearly to the value of the initial charge Q_0, reaching this value when the holes are collected at the cathode.

1.4.4 Induced charge

The induced charge signal on an electrode can be calculated by using the theorem of Ramo [13], in which uses the weighting potential. The weighting potential (dimensionless) is defined as the potential that would exist in the detector with the collecting electrode at "unit" potential[6], while holding all other electrodes at zero potential. The Ramo theorem which was originally applied to calculate the induced charge in vacuum tubes with no space charge was also proven to be valid by Jen [14] and Cavalleri *et al.* [15] for devices with the presence of stationary space charges (e.g., semiconductors). The theorem of Ramo is reviewed and discussed by He [16] with its applications in semiconductor gamma-ray detectors in focus. The theorem states that regardless of the presence of space charge, the change in the induced charge $\triangle Q_{ind}$ and the current i at an electrode by q moving from $\mathbf{x}_i$ to $\mathbf{x}_f$ is given by:

$$\begin{aligned} \triangle Q_{ind} &= \textstyle\int_{\mathbf{x}_i}^{\mathbf{x}_f} q\mathbf{E}_w \cdot d\mathbf{x} = -q[V_w(\mathbf{x}_f) - V_w(\mathbf{x}_i)] \\ i &= \tfrac{dQ}{dt} = q\mathbf{v} \cdot \mathbf{E}_w \end{aligned} \tag{1.24}$$

$V_w(\mathbf{x})$ and $\mathbf{E}_w(\mathbf{x})$ are the weighting potential (dimensionless) and weighting field at q's instantaneous position $\mathbf{x}$.

The trajectory of the point charge q is determined by the electric field $\mathbf{E}$. The induced charge Q_{ind} is determined by the weighting field and it is independent of the applied operating electric field. The weighting field $\mathbf{E}_w(\mathbf{x})$ is the gradient of the "unit" potential V_w and it is given by:

$$\mathbf{E}_w = -\nabla V_w(\mathbf{x}) \tag{1.25}$$

Consider that a photon with energy E_p is absorbed in the volume of a semiconductor detector with a planar electrode geometry and a thickness d. The weighting field and operating electric field can be reduced to one dimension since the derivative of the $V(x, y, z)$ in the y-direction and the z-direction will be equal to zero. Integrating Eq. (1.18) and Eq. (1.25) only in the x-direction results in $E = V/d$ and $E_w = 1/d$ respectively. The electron charge $Q_e = -qN_0$ and the hole charge $Q_h = qN_0$, generated by the incident photon at position x_0, start to drift towards opposite electrodes by the electric field E. In order to determine the total induced charge on the electrodes, for different charge

[6]The weighting potential is the calculated electric potential divided by the assigned bias voltage at the electrode. Therefore, $0 \leq V_w(\mathbf{x}) \leq 1$ and has no dimension.

carriers, charge trapping within the detector at first is neglected. Then the total induced charge becomes independent of the actual path of the charge carriers. The initial charges Q_e and Q_h are assumed to be point charges. The induced charge signal on the collecting electrodes can be calculated using Eq. (1.24). The total induced charge on an electrode is the sum of the contribution of the electrons $Q_{ind,e}$ and the holes $Q_{ind,h}$:

$$Q_{tot} = Q_{ind,e} + Q_{ind,h} \tag{1.26}$$

The change in induced charge $\triangle Q_{ind,e}$ on the collecting electrode can be derived from current i in Eq. (1.24) as the current is given by:

$$i = \frac{dq}{dt} = qvE_w = qv\frac{1}{d} \tag{1.27}$$

where $v = \mu E$ is the carrier drift velocity. If the point charge qN_0 is moved through an infinitesimal displacement dx, the carrier drift velocity can be rewritten as $v = dx/dt$. The change in induced charge $\triangle Q_{ind}$ on an electrode can be rewritten from Eq. (1.27) as:

$$\begin{aligned} \triangle Q_{ind,e} &= Q_e \tfrac{1}{d} dx \\ \triangle Q_{ind,h} &= Q_h \tfrac{1}{d} dx \end{aligned} \tag{1.28}$$

Electrons will drift from the initial interaction position at x_0 to the anode electrode with a total drift path of $d - x_0$. Holes will drift from the initial interaction position at x_0 to the cathode with a total drift path x_0. The total induced charge Q_{tot} on an electrode can be obtained by integrating Eq. (1.28) along the path of electrons and holes:

$$\begin{aligned} Q_{tot} = Q_{ind,e} + Q_{ind,h} &= \textstyle\int_{x_0}^{d} Q_e \frac{1}{d} dx + \int_{x_0}^{0} Q_h \frac{1}{d} dx \\ &= -qN_0 \tfrac{(d-x_0)}{d} + qN_0 \tfrac{(-x_0)}{d} \\ &= -qN_0 \end{aligned} \tag{1.29}$$

An accurate determination of the energy E_p absorbed in the volume of a semiconductor detector, requires that all the electron and hole charge carriers are collected. In practice, compound semiconductor materials suffer from imperfections introduced during crystal growth, during device fabrication or by radiation damage. These structural defects in the crystal, impurity atoms, vacancies or structural irregularities (e.g., dislocations) introduce states into the crystal that can trap charge carriers. These trapping phenomena usually occur

for both carriers. The charge trapping is characterized by a carrier lifetime τ, the average time a charge carrier can "survive" in a crystal before the trapping occurs. It is possible that the trapped carriers may be released from the trap, drift in the field and be trapped again. Depending on the nature of the trap, thermal excitation or externally applied field can release a trapped carrier, leading to delayed charge collection. A macroscopic model which describes the behavior of the charge trapping phenomena is the exponential decay of the initial charge Q_0 with a time constant equal to the lifetime τ and is given by:

$$Q(t) = Q_0 \exp(-\frac{t}{\tau}) \tag{1.30}$$

After an elapsed time t, the charge traversed a distance x with a carrier speed $v = \mu E$ and it is:

$$t = \frac{x}{v} = \frac{x}{\mu E} \tag{1.31}$$

Assuming a uniform material, the remaining charge after the distance x can be written as:

$$Q(x) = Q_0 \exp(-\frac{x}{\mu \tau E}) \tag{1.32}$$

This simple mathematical model describe very well the charge trapping phenomena and it is used in this thesis. When including the charge trapping within the detector given by Eq. (1.32) into Eq. (1.28) and assume that no de-trapping effects are present one gets:

$$\begin{aligned} \triangle Q_{ind,e} &= Q_e \tfrac{1}{d} e^{(-\frac{x}{\mu \tau_e E})}\, dx \\ \triangle Q_{ind,h} &= Q_h \tfrac{1}{d} e^{(-\frac{x}{\mu \tau_h E})}\, dx \end{aligned} \tag{1.33}$$

An integration of Eq. (1.33) along the path in electrons and holes assuming that no detrapping effects are present, will result a total induced charge on the collecting electrodes as a function of interaction position as:

$$Q(x) = Q_0 \left[\frac{\mu \tau_e E}{d} \left(1 - e^{(-\frac{x-d}{\mu \tau_e E})} \right) + \frac{\mu \tau_h E}{d} \left(1 - e^{(-\frac{x}{\mu \tau_h E})} \right) \right] \tag{1.34}$$

This equation is known as Hecht-relation [17]. The Hecht-relation is widely used to describe the signal formation in a conventional planar detector.

1.4.5 Depletion layer

A semiconductor material has a resistivity lying between that of a conductor(very low resistivity) and that of an insulator (very high resistivity). A

semiconductor establishes its conduction properties through a complex quantum mechanical behavior within a periodic array of semiconductor atoms, i.e., within a crystalline structure. For appropriate atomic elements, the crystalline structure leads to a disallowed energy band between the energy level of electrons bound to the crystal's atom and the energy level of electrons free to move within the crystalline structure (i.e., not bound to an atom). This "energy gap" fundamentally impacts the mechanisms through which electrons associated with the crystal's atoms can become free and serve as conduction electrons. The resistivity of a semiconductor is proportional to the free carrier density, and that density can be changed over a wide range by replacing a very small portion (about 1 in 10^6) of the base crystal's atoms with different atomic species (doping atoms). The majority carrier density is largely pinned to the net dopant impurity density. In addition, some dopants establish the electron carrier density (free electron density) while others establish the "hole" carrier density. In a completely pure semiconductor, all the electrons in the conduction band and all the holes in the valence band would be caused by thermal excitation. Such material is called intrinsic semiconductor. The number of electrons in conduction band is equal to the number of holes in the valence band in this type of materials. This is of course theoretically possible but in practice it is impossible to achieve. There are always some small levels of residual impurities in the real material after the best purification process which is an important factor for the electrical properties of the material. Some small concentration of impurity can be added to semiconductor intentionally. In this manner, different types of semiconductor (n-type with much higher electron carrier density than the hole density and p-type with much higher hole carrier density than the electron carrier density) can be produced.

By intentionally applying the bias as a reverse to the appropriate type of semiconductor detector device, the charge collection capabilities may be improved as the semiconductor becomes depleted of mobile carriers within the depletion region and the charge density in that region is due to the ionized donors. The applied voltage on the electrodes creates space charge region also called "depletion layer" within the semiconductor as a function of the voltage and material type. This region acts like a high resistivity ionization chamber making it feasible to use for radiation detection.

The charge density in a semiconductor depends on the free electron and hole density and on the ionized impurity densities. Ionized donors, which have given off an electron, are positively charged. Ionized acceptors, which have accepted an electron, are negatively charged. The total charge density is therefore given by:

$$\rho = q(p - n + N_d^+ - N_a^-) \tag{1.35}$$

where p is the density of free holes, n is the density of the free electrons, N_d^+ is the doping concentration for the donors and N_a^- is the doping concentration for the acceptors. In the depletion region, $\rho = q(N_d^+ - N_a^-) = q(N_{eff})$ since there are no free carriers.

In an abrupt junction, the depletion layer width, W, expressed as a function of the applied voltage V_{dep} is given by [1]:

$$W = \sqrt{2\varepsilon_0\varepsilon_s\rho\mu V_{dep}} \tag{1.36}$$

where μ is the mobility, ρ is the resistivity and ε_s is the dielectric constant of the semiconductor. $\varepsilon_0 = 8.85 \times 10^{-14}\ F/cm$ is the permittivity of free space. The Eq. (1.36) is tested using properties given in Tab. 1 for the CdZnTe drift strip detector fabricated and used in this thesis using 0.27 cm thick n-type material with a electron mobility of 1000 cm^2/Vs. The voltage required for full depletion of the detector thickness d=0.27 cm is calculated as:

$$V_{dep} = \frac{d^2}{2\varepsilon_0\varepsilon_s\rho\mu} \simeq 0.00126 volt \tag{1.37}$$

This value is a factor of 10^4 less than the measured full depletion voltage V_{dep}. V_{dep} was experimentally determined on this detector illuminating the detector from both the planar side (cathode) and the strip side (anode) with photons and alpha particles (^{109}Cd, ^{241}Am) and varying the bias voltage. From these measurements it was found that the detector material is n-type with $V_{dep} = 20 \pm 5$ volt. As can be seen, the model for the depletion layer with given in Eq. (1.36) can not be used for CdZnTe semiconductor detector material. Other unknown effects may play role in depleting the CdZnTe material and the model must be described taking these effects into account. It is shown by G. Lutz [7] that the Eq. (1.36) is working for detector material fabricated from the highest purity possible i.e., Si.

2

Cadmium Zinc Telluride (CdZnTe) material

Among the room temperature semiconductor detector materials available for X-ray and gamma ray detection, CdZnTe is among those having been studied quantitatively over the past decades. The material still is in rapid evolution. This thesis is not investigating the material science properties of this material. The current state of the material quality is just accepted and its properties with respect to X-ray and gamma-ray detection are investigated.

2.1 Introduction

Cadmium Zinc Telluride (CdZnTe) is a compound semiconductor that has been extensively studied over the last decade with X-rays and gamma rays. It has a cubic, zincblende type lattice with average atomic number close to 50. The chemical composition of the crystal is CdZnTe. The common term, which is used to identify the crystal, is $Cd_{1-x}Zn_xTe$, where x is the fraction of Zn content in the crystal. The $Cd_{1-x}Zn_xTe$ crystals that are investigated in this thesis have the form of $Cd_{0.9}Zn_{0.1}Te$ (10% nominal value of Zn concentration are selected from suppliers data shown in Tab. 2.1). After this section, the term CdZnTe will refer to $Cd_{0.9}Zn_{0.1}Te$. This chapter will summarize the basic in CdZnTe crystals.

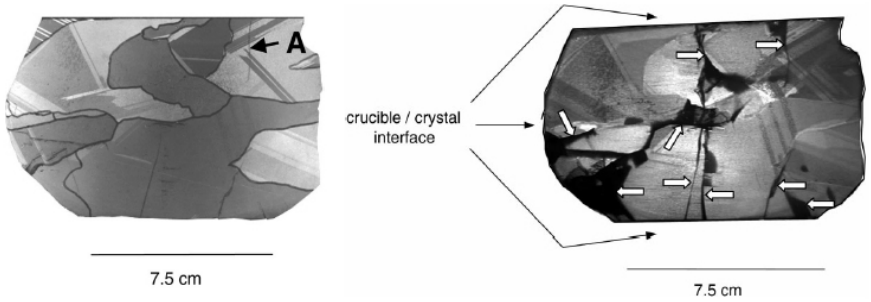

Figure 2.1 The range of grain sizes in an axially sliced CdZnTe material made by the high-pressure vertical Bridgman (HPVB) method. The slice is cut perpendicular to the axis of the ingot. Optical photograph of the wafer (left) with some of the grain boundaries outlined in black. Cracks are visible and they originate from the edge of the wafer and propagate inward through grains and twins (as marked by "A"). Infrared transmission image (right) of the same the wafer with the major cracks identified with arrows. [Photographs courtesy of eV-Products.]

2.2 CdZnTe crystal growing

A comprehensive review of the growing of $Cd_{1-x}Zn_xTe$ crystal and its material properties can be found in [18] and [19]. In the article [18], the most employed method in the growth of $Cd_{1-x}Zn_xTe$ is reported to be the Bridgman crystal growth method and its number of variations. Although significant progress has been achieved in the growth of high-quality CdZnTe semiconductor crystals using the Bridgman technique, this material suffers from the poor charge collection efficiency caused by deep level traps. When a compound semiconductor like CdZnTe is going to be used as room temperature nuclear radiation detector application, then the most important requirements for the electrical and the structural material properties are high resistivity and minimum defect free materials. The high-pressure Bridgman (HPB) method and the high-pressure vertical Bridgman (HPVB) method were reported to be the suppliers primarily choices for the growing of CdZnTe commercially. HPVB is presently the main source of material and is capable of reliably producing high-resistivity material with the electron transport properties needed for spectroscopy. Order of $10^{10}\Omega\,cm$ CdZnTe bulk resistivty is commonly reported in many independent articles. High values of $\mu\tau_e$ ($(1-10)\times 10^{-3}\quad cm^2/Vs$) are reported elsewhere (see Tab. 2.2). The main limitation of the CdZnTe technology is the limited

size of single crystals that can be routinely harvested from ingots grown by HPVB. At present, the largest single crystals manufactured for gamma-ray detectors from HPVB material typically have volumes about $2cm^3$. Cracks and macroscopic structural defects in the material related to the crystal growing are limiting the size of the achievable single crystal in HPVB CdZnTe. Therefore commercially available CdZnTe crystals are usually polycrystalline in nature. The cracks can easily be identified by using infrared transmission imaging technique. As an illustration, the range of grain sizes in an axially sliced HPVB CdZnTe material is shown in Fig. 2.1, with an Optical photograph of the wafer (left) with some of the grain boundaries outlined in black. Cracks are visible and they originate from the edge of the wafer and propagate inward through grains and twins (as marked by "A"). Infrared transmission image (right) of the same the wafer with the major cracks identified with arrows. The cracks appear dark (black) in the infrared because of the scattering due to the irregular and rough surfaces.

These defects, the grain boundaries, are important issues which are known to trap charge carriers and can reduce the full-energy (photo-peak) efficiency and degrade pulse height resolution. Consequently, a uniform response can not be archived from a large detector area. The carrier transport can vary significant between the grain regions. This is an undesirable structural defect within the material. The consequences for the single carrier sensitive radiation detectors (e.g., electron sensitive device) are serious performance degradation. Degradation can range from catastrophical degrading (loss of signal) to a spectrometric degrading (double peak or peak broadening) for a single carrier sensitive device.

2.3 CdZnTe material properties

Property	Nominal	Actual
Zn fraction (%)	10	5-13
Band gap at room temperature (eV)	1.56	1.53-1.58
Intrinsic resistivity ($\times 10^{10}$ Ωcm)	3.0	1.7-4.0
$\mu\tau_e(\times 10^{-3} cm^2/V)$	2.5	0.5-5.0
$\mu\tau_h(\times 10^{-5} cm^2/V)$	2.0	0.2-5.0

Table 2.1 The electrical properties of HPVB-grown CdZnTe crystals at a low temperature (e.g., room temperature) [20].

The commercial supplier of the CdZnTe crystals used in this thesis is eV-

products[1]. The typical material properties for the CdZnTe crystal given by the supplier are shown in Tab. 2.1. The mobility of electrons was reported with a variation from 1000 to 1300 cm^2/Vs elsewhere. All the CdZnTe material produced in USA was reported to be an n-type material. All the CdZnTe detectors designed and fabricated in this thesis are n-type.

2.3.1 Resistivity

The charge density in a semiconductor depends on the free electron and hole density and on the ionized impurity densities. The bulk conductivity of a CdZnTe semiconductor is proportional to the total free carrier density, and that density can be adjusted by applying a bias creating an electric field within the material. By applying the electric fields appropriately, small regions of the semiconductor can be placed in a state where all the carriers (electrons and holes) have been expelled by the electric field. Then the remaining charge density within the material is due to the ionized impurity densities. When a n-type semiconductor is depleted of mobile carriers within the depletion region, then the charge density in that region is due only to the ionized donors. Outside the depletion region, the semiconductor is assumed neutral. The resistivity therefore is higher for the depleted region than for the un-depleted zone. The conductivity of a material is defined to be the current density J, divided by the applied electric field $\mathbf{E}$. Since the current density J equals the product of the charge of the mobile carriers, their density and velocity, J can be expressed as a function of the electric field, the mobility μ_e and μ_h, and the density of free electrons n and free holes p :

$$\mathbf{J} = \sigma\mathbf{E} = q(n\mu_e + p\mu_h)\mathbf{E} \tag{2.1}$$

The conductivity σ due to electrons and holes then becomes:

$$\sigma = q(p\mu_h + n\mu_n) \tag{2.2}$$

The resistivity ρ equals the inverse of the conductivity or:

$$\rho = \frac{1}{\sigma} = \frac{1}{q(p\mu_h + n\mu_n)} \tag{2.3}$$

As n-type materials contain almost no holes, and the resistivity therefore becomes:

$$\rho = \frac{1}{qn\mu_n} \tag{2.4}$$

[1]eV-products is the supplier for all the CdZnTe drift strip detectors used in this thesis. eV-products is located in Saxonburg, Pennsylvania, USA.

The resistivity can be calculated from the current-voltage characteristic. In this thesis, the resistivity of CdZnTe material (GSFC-CZT-1) was measured from the current-voltage characteristic for the bulk material and found to be order of 2.4×10^{10} Ωcm.

2.3.2 Electrical contacts

Metal-to-semiconductor junctions are of great importance since they are present in every semiconductor device. They can behave either as a Schottky barrier or as an Ohmic contact depends on the characteristics of the interface between the metal contact and the semiconductor. An oxide layer formed during the fabrication of contacts on detectors make the electrical measurements complicated. An ohmic contact (Metal-Semiconductor contact) or a none ideal ohmic contact structure (Metal-Insulator-Semiconductor contact)[2] with a negligible contact resistance compared with the bulk or series resistance of the semiconductor can be the result after the contacting process. Gold (Au), indium (In) and platinum (Pt) are the most commonly used metals for contacting the CdZnTe detectors. Contact related problems are not discussed in details in this thesis. The problems concerning contacts are reviewed in Burger *et al.* [21]. In this paper, the author presents a surface and contact characterization study aimed at establishing the effects of the surface preparation steps prior to contacting (polishing and chemical etching), the choice of the metal and contact deposition technique, and the surface oxidation process. The author reports that the metals of choice for p-type high-resistivity CdZnTe are high work function metal like Au and Pt in order to fabricate Ohmic contacts. On the other hand most low work function metals such as In satisfy the condition for ohmic contacts on n-type CdZnTe. The net effect is that the current-voltage characteristic of the detector depends on the work function of the electrode metal, the type and the surface treatment of the CdZnTe. The role of the surface oxide on CdZnTe, was studied by Bolotnikov *et al.* [22]. This paper present mainly a surface and contact characterization study of several Pt-CdZnTe-Pt pixel detector aimed to establish the effects of the surface oxidation layer.

Several contact related problems remain to be solved in the development of high-efficiency and high-sensitivity CdZnTe detectors. The surface preparation during the detector fabrication plays a vital role in determining the contact characteristics and the surface leakage current for detectors using multi electrodes. The surface leakage current is often the dominant factor influencing the detector performance. The surface treatment leads to improvements in this

[2] A Metal-Insulator-Semiconductor frequently referred to as a "MOS" or a Metal-Oxide-Semiconductor. The insulator layer, which is an oxide layer, is usually formed during the fabrication of the detector.

area. The type of surface treatment developed at Goddard Space Flight Center (GSFC) [23] was applied to some of the CdZnTe drift strip detectors (GSFC-CZT-1 and GSFC-CZT-4) used in this thesis with great success in terms of achieving high surface resistivity. This treatment resulted in a interstrip resistance of $7.6 \pm 1.5\ G\Omega$ for these detectors having a strip pitch of 0.2 mm with a strip width of 0.1 mm and a strip length of 9.5 mm. The measurements were conducted at GSFC before shipping.

2.3.3 Charge transport properties

Charge transport is characterized by two parameters for each carrier type: mobility, μ, and mean trapping lifetime, τ. A commonly used method to study the transport properties in detectors with planar geometry is based on their response to alpha-particles. When irradiating the detector on the cathode side, the penetration depth of alpha-particles is only a few microns therefore the obtained signal is due to the electron collection. By measuring the charge collection with a long shaping time (needed for avoid the ballistic deficit) as function of bias and fitting the data to the Eq. (1.34) (for single carrier), one can extract the $\mu\tau_e$ (or $\mu\tau_h$ when irradiating the detector from anode side). Some recent measurements for electron and hole transport properties in spectrometer grade[3] CdZnTe found in the literature from a number of authors are presented and summarized in Tab. 2.2.

Author	Year	$\mu\tau_e$ (cm^2/V)	$\mu\tau_h$ (cm^2/V)
Luke [25]	1995	4×10^{-3}	2×10^{-5}
Lund [26]	1996	6×10^{-3}	9×10^{-5}
Toney [27]	1996	6×10^{-3}	3×10^{-5}
Eisen [28]	1997	$(1 - 10) \times 10^{-3}$	$8 \times 10^{-6} - 3 \times 10^{-5}$

Table 2.2 Some electrons and holes transport properties in CdZnTe found in the literature.

Note that all these measurements show that $\mu\tau_e$ is much greater than the $\mu\tau_h$. Most values for $\mu\tau_e$ and $\mu\tau_h$ are of the order $10^{-3}\ cm^2/V$ and $10^{-5}\ cm^2/V$ respectively. For thin detectors, these values would provide acceptable spectral

[3] The quality of the CdZnTe detector material harvested from the ingots are characterized using a standard measurement set-up by eV-products and they are labelled as "counter" grade, "discriminator" grade or "spectrometer" grade by increasing quality. eV-products inform [24] about the standard measurement set-up as follow: The listed criteria apply to material of thickness from 1 to 5 mm. Typical measurements are performed with an applied field of between 1000 and 2000 Volts/cm of thickness, preamplifier shaping time of 0.25 - 2.0 μs and an external ultra low noise preamplifier (eV-5093). Noise threshold for all classifications 10 keV.

detector response. For thick detectors (> mm), incomplete charge collection would occur. Differences among the values suggest that the $\mu\tau$ products have considerable variation from crystal to crystal, and/or that an accurate measurement of the $\mu\tau$ products in a CdZnTe crystal is difficult. The $\mu\tau_e$ for the GSFC-CZT-1 and the GSFC-CZT-4 were measured as 5×10^{-3} cm^2/V and 8×10^{-3} cm^2/V, respectively.

2.4 X-ray spectral mapping of a CdZnTe drift strip detector

One of the critical challenges for using a large area CdZnTe detector arrays is to get a material with a uniform imaging and spectroscopic response. Commercially available CdZnTe crystals are usually polycrystalline in nature and the grain boundaries that separate the crystal grains with a different carrier transport characteristics introduce a inhomogeneity in the material. These defects can result in non-uniform properties within the material. One of the fabricated drift strip detectors (BSI-CZT-2) used in this thesis has shown a significant spectral non-uniformity behavior and is suspected to suffer spectral performance degradation caused by the grain boundaries. This detector was investigated in order to show the negative impact of the grain boundaries on the detector performance.

Two non-destructive techniques are widely used for characterizing the semiconductor CdZnTe material to detect macroscopic structural defects in the material. The first technique, infrared transmission imaging, allows for rapid visualization of bulk defects. The second technique, X-ray spectral mapping, provides a map of the material spectroscopic response when it is configured as a planar detector. These techniques can be used to develop a correlation between bulk defect type and detector performance. The correlation allows for the use of infrared imaging to rapidly develop material defect maps. Therefore the yield and quality of large area CdZnTe detector arrays increase. The X-ray spectral mapping technique can provide information on uniformity of the $\mu\tau$ for the material.

Fig. 2.2 shows the BSI-CZT-2 detector image. The material piece missing in the left upper corner was lost after the scan. The detector crystal supplier was eV-product, and metal contacts were deposited by the firm Baltic Scientific Instruments (BSI). The material was specified as spectroscopic grade. It can be seen that the detector was not treated with care after the metal contacts were deposited by BSI. They made a lot of scratching on the planar electrode surface during the gluing and wire bonding processes. However, the strip side was free of these scratches. This is indeed very important as the scratches

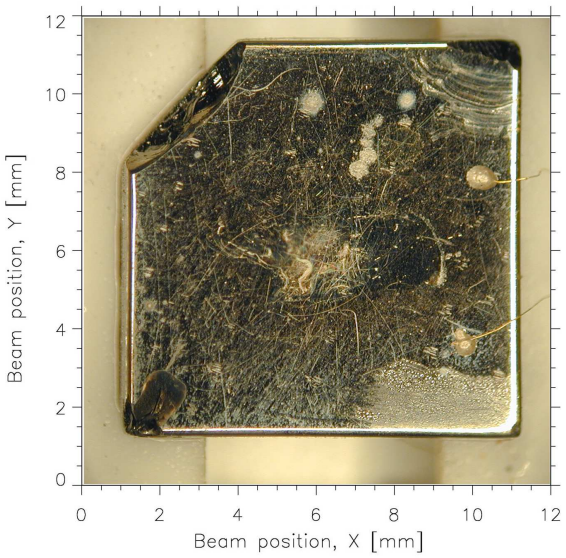

Figure 2.2 The X-ray scan covered a 12 mm×12 mm area. The orientation and the place of the detector surface in the scan area is approximately illustrated in the picture by using the scaled real detector image. The material piece missing in the left upper corner was lost after the scan. The detector crystal supplier was eV-product and the metal contacts were deposited by the firm Baltic Scientific Instruments (BSI). The material was specified as spectroscopic grade. It can be seen that the detector was not treated with care after the metal contacts were deposited by BSI. The company made a lot of scratches on the detector surface during the gluing and wire bonding processes.

would change the surface leakage current.

2.4.1 Experimental

An X-ray scan was arranged for this detector for the defect study. The scan was performed to the BSI-CZT-2 at the Space Radiation Laboratory at Caltech (in connection with this Ph.D. study). The detector itself was used to generate a X-ray map in order to show the grain boundaries. For the set-up, a compact detector electronic box containing first stage preamplifiers (7 x eV-products eV-5093) was used. Six preamplifiers for anode strips and one preamplifier for

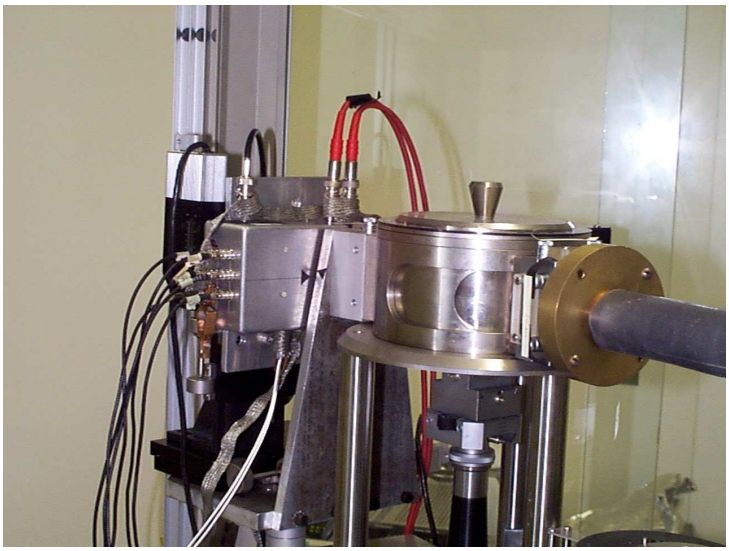

Figure 2.3 Picture showing the set-up for the X-ray scan of the BSI-CZT-2 detector. The box containing the BSI-CZT-2 detector and the preamplifiers is placed on a XY-table in front of the beam. The black thin cables connect the signal outputs from the preamplifiers with the shaping amplifiers. The red cables bias the detector with Vp and Vd from two high voltage power supplies. The cylindrical metal container contains the monochromatic crystal set-up, which selects the monochromatic energy of the K_α line (17.5 keV) from the Mo anode.

the planar electrode were mounted inside the box together with the detector. The cathode side of the detector was irradiated with a collimated X-ray beam. The beam source was a X-ray machine Philips XGR3100 with a water cooled Mo anode tube. The beam with energy of K_α line (17.5 keV) from Mo was isolated by dispersive geometry and collimated to a beam spot size of 300 x 200 μm^2 by two slits. The detector was protected by a thin (100 μm) Al window from visible light. The attenuation length for Al at 17.5 keV is ≈ 800 μm therefore $\approx 10\%$ intensity reduction was expected due to the Al window. The attenuation length for CdZnTe at 17.5 keV is ≈ 50 μm therefore photons are absorbed very close to planar electrode so the entire induced signal is due to the motion of the electrons. The X-ray machine was operated with a voltage of 25 kV and a current of 14 mA. Fig. 2.3 shows the set-up for the X-ray scan of the BSI-CZT-2 detector. The box is placed on a 2D XY-table in front of the beam. The black thin cables connect the signal outputs with the shaping

amplifiers. The white cables supply the DC voltages for the preamplifiers. The red cables supply the detector bias voltages, the planar electrode bias Vp and drift electrode bias Vd from two high voltage power supplies. The cylindrical metal device contains the monochromatic crystal set-up.

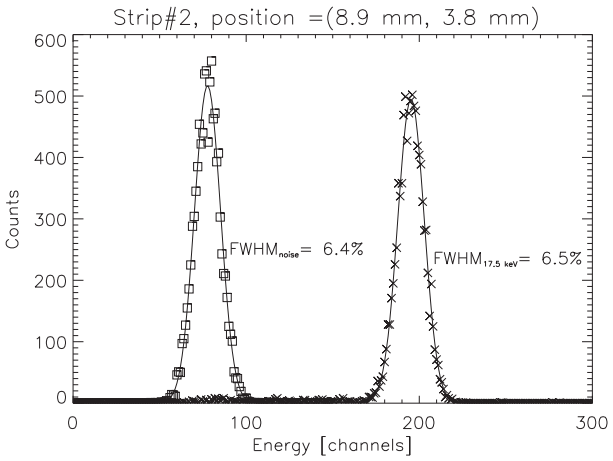

Figure 2.4 Plot showing the spectrum of the Mo K_α line (17.5 keV) together with the total readout electronic noise for the electronic chain of anode strip number 2. The peaks are fitted with a Gaussian peak. The energy resolution of 6.5% FWHM at 17.5 keV (right) was measured with a total electronic noise (left) of 6.4% FWHM.

An area of a 12 mm $\times$ 12 mm was scanned by stepping the detector in 2 dimension by the XY-table. The step in the x-direction and the y-direction were 300 μm and 200 μm, respectively. The detector box was aligned so that the detector crystal was in the center of the scan area with a $\approx$ 1 mm distance from the sides. Fig. 2.2 shows an illustration of the orientation and the approximately place of the irradiated detector surface in the scan area. In this orientation, the strips are parallel to the X-axis and numbered increasingly upward (see Fig. 2.8). Signals from all 7 electrodes (six anode strips electrodes and one planar electrode) are amplified, shaped and digitized. Each shaping amplifier output was connected to a Analogue to Digital Converter (ADC) on a 16 channels multi parameter analyzer system. A real time data acquisition and data recording program (also works as a controller program for the XY-table) was developed and used. The XY-table control program was developed and integrated in this data acquisition program (runs synchronously with it). Each preamplifier was connected to a shaping amplifier and the shaping time was adjusted to 1 μs for all shaping amplifiers. The gain was adjusted for all

the shaping amplifiers as well. The shaping time and the gain of the shaping amplifier were kept constant during the scan. Great effort and time have been used in order to solve the many problems under preparation of the scan. The read-out electronic was modified several times in order to reduce the total electronic noise and the pick-up noise. The detector bias voltages were -300 V and -80 V for Vp (planar electrode bias) and Vd (drift bias voltage) respectively.

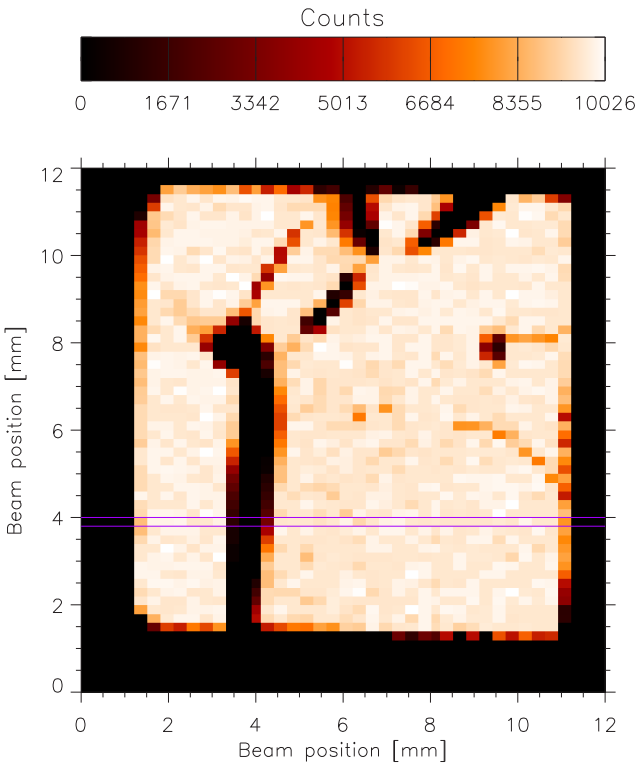

Figure 2.5 X-ray map showing the non-uniformity of the BSI-CZT-2. The picture shows the spatial distribution of the number of counts under the photo peak of the Mo K_α line (17.5 keV). This result shows the correlation between the detector response and the grain boundaries within the detector. The detector signals were small or disappeared completely when these zones were irradiated. Spectra for the beam positions between the thin, blue, horizontal lines were used to show effect of the grain boundaries on the measured spectrum later in this text.

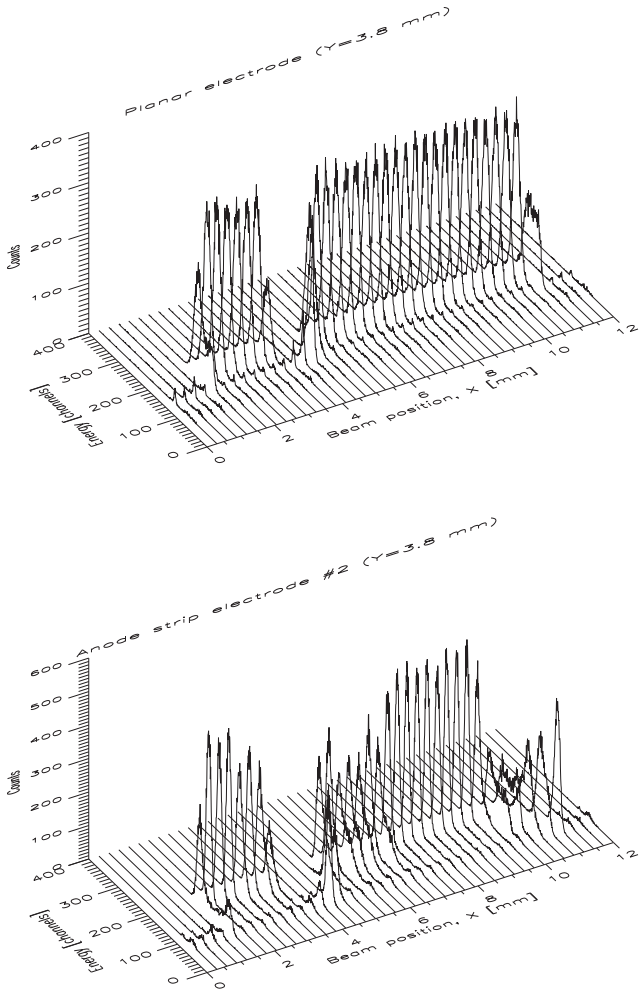

Figure 2.6 The effect of the grain boundaries to the spectral response of the BSI-CZT-2 detector . The upper part shows the spectra recorded by the planar electrode and lower part shows the spectra recorded by the strip number 2 for each position of the beam. These spectra were recorded when the beam was at the positions in x-direction 0 to 12 mm with a constant y-value of 3.8 mm (shown in Fig. 2.5 as thin blue lines). The non-uniformity of the material in this part of the detector influences the spectroscopic performance of the detector. Spectra with a double peak and/or photo peak position shift can be seen in both plots.

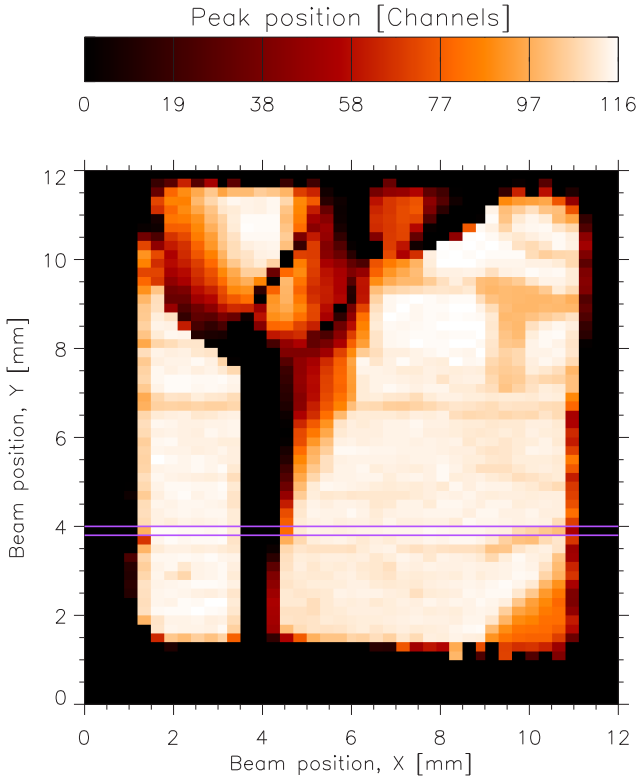

Figure 2.7 Picture showing the spatial distribution of the photo peak position of the Mo K_α line (17.5 keV). The spectra were obtained from the planar electrode. The result is displayed with the color code shown in the upper inset. The white areas indicate the best detector performance while the dark areas represent the poor detector performance which is due to the grain boundaries within the detector. The detector signals were small or disappeared completely when these zones were irradiated by the X-ray beam.

The beam intensity was moderate and was measured to be in the order of 300 photon/s on the good part of the detector (the beam was at the regions of the detector where no significant spectral degradation could be detected). Data from all seven detector signal were recorded in 60 second for each beam positions. The total scan time was several days. Three attempts failed. Each time modification of detector electronic, readout electronic calibration and mechanical alignment was repeated. The low energy threshold for each electronic detector-preamplifier- shaping amplifier-ADC chain was adjusted. The noise

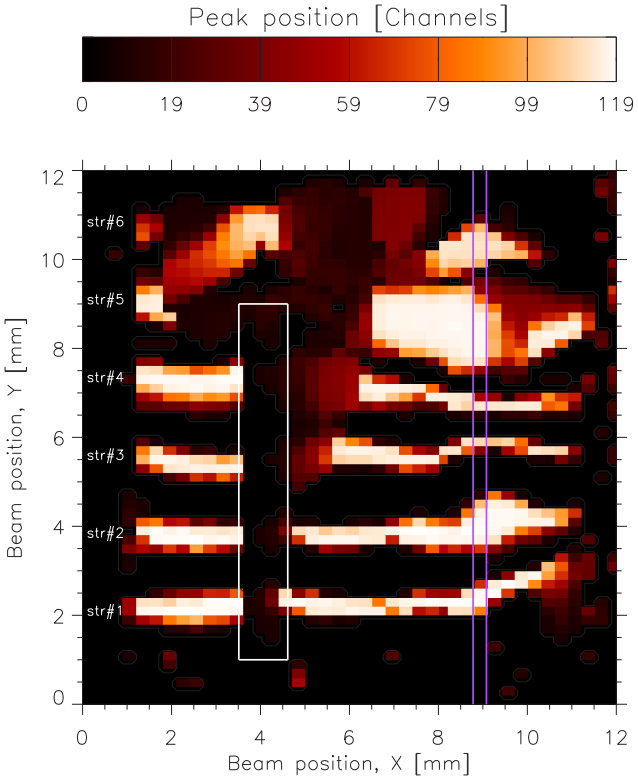

Figure 2.8 Plot showing the spatial distribution of the photo peak channel of the Mo K_α line (17.5 keV). The spectra were obtained from the anode strip electrodes. The result is displayed with the color code shown in the upper inset. The white areas indicate the best detector performance. A grain boundary in the detector is shown in the white rectangular. The photo peak obtained from the anode strip electrodes (1-5) have disappeared in this area. The dark areas between the anode strips represent the "dead-zone" within the detector. The detector signals were small or disappeared completely when these zones were irradiated by the X-ray beam.

spectra for each chain were also recorded in order to find the ADC offset and the electronic noise contribution to the photo peak.

Last scan attempt was successfully completed. Signals from all seven electrodes (six anode strips electrode and one planar electrode) were amplified, shaped and digitized correctly. All the coincident signals were recorded during the scan for each beam position. For each set of data, the measured spectra

obtained by each electrode were analyzed. The electronic noise and the photo peak of Mo K_α were fitted with a Gaussian function in order to determine the FWHM and the total number of counts under the peak. As an example, a typical recorded spectrum is shown in Fig. 2.4 when the beam was at position of (X,Y)= (8.9 mm; 3.8 mm) on the detector. The spectrum was recorded using the strip number 2. Electronic noise and the Mo K_α line (17.5 keV) was fitted with a Gaussian peak in Fig. 2.4. The Mo K_α line (17.5 keV)(right) energy resolution was measured as 6.5% FWHM with a total electronic noise (left) of 6.4% FWHM. After analyzing all the recorded data, a map was generated for the peak position data and the counts in the photo peak in order to show a picture of the grain boundaries existing in the BSI-CZT-2. Fig. 2.5 shows the spatial distribution of counts in the photo peak for the scanned area of 12 mm x 12 mm. This result shows the correlation between the detector response and the grain boundaries within the detector thus unveiling non-uniformity of the BSI-CZT-2. The detector signal is correlated with the carrier transport capacity in each grain. Therefore, the spectra for the beam position between the blue lines are used to show the effect of the grain boundaries on the spectral performance of the detector.

The spatial distribution of the photo peak position shift is shown in Fig. 2.7. The data were obtained from the planar electrode. The 17.5 keV peak position distribution within the BSI-CZT-2 recorded by the anode strips is shown in Fig. 2.8. The effect of grain boundaries are easily seen on the anode strip signals. The narrow dark area is marked with the white rectangle cover from anode strip 1 to anode strip 5 and represents the bad part of the detector material. The detector material under this area does not work properly and the detector signal is degraded. Fig. 2.9 shows the spatial distribution of the photo peak position of Mo K_α line (17.5 keV) measured by the planar electrode and the anode strip electrodes (1-6) at two different x-positions (shown in Fig. 2.8 as blue lines at x=9 mm and the white rectangular area at x=3.9 mm). The plot on the left shows (at x=3.9 mm) that the anode strip signals 1-5 have disappeared when compared to the plot on the right (at x=9 mm). The gap between the anode strip caused by the electric field is clear in the plot on the right (at x=9 mm).

2.4.2 Discussion

The spatial distribution of the photo peak position shift is shown in Fig. 2.7 for the scanned area of 12 mm x 12 mm. The data were obtained from the planar electrode. From the figure, one can see that the peak position shift is not significant for most of the detector area and is order of 10% variation. The peak positions in some places were shifted significantly which was correlated

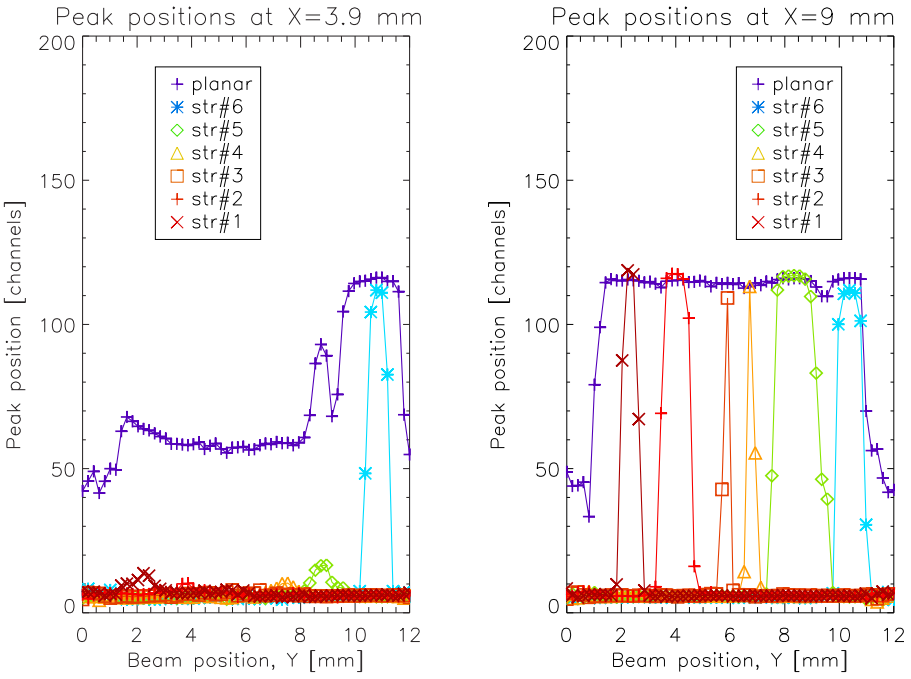

Figure 2.9 Plots showing the spatial distribution of the photo peak position of Mo K_α line (17.5 keV) measured by the planar electrode and the anode strip electrodes (1-6) in two different x-positions (shown in Fig. 2.8 as blue lines at x=9 mm and the white rectangular area at x=3.9 mm). The plot on the left shows (at x=3.9 mm) that the anode strips 1-5 have disappeared when compared to the plot on the right (at x=9 mm). The lines are made in order to facilitate reading the plots.

to the crystal grain boundaries with different charge trapping properties. This means that non-uniform charge trapping in crystal boundaries exist in BSI-CZT-2. The effect of these grain boundaries on detector performance which are related to the very poor charge transport properties within the defect area of the material is catastrophic. This can be observed as a deficit of counts in a spectrum. The effect is shown in Fig. 2.8. The plot on the left shows (at x=3.9 mm) that the anode strip signals 1-5 have disappeared when compared to the plot on the right (at x=9 mm). This type of material defect is very detrimental to the overall performance of the CdZnTe detector. Therefore, CdZnTe crystals to be use as detector material should be tested for this type of material defects with X-ray mapping. Besides this grain boundaries, it is

possible to see in the Fig. 2.7 that some area where the peak position shifted slightly and almost constant along the x-direction parallel to the strips. This effect can be explained by the electric field within the detector is in fact not uniform and the peak position shift in this area is correlated with the non-uniform electric field due to the varyings drift strips bias voltages. The electric field is determining the path of the charge carriers generated by the incident photon. Dependent on the operation voltages, the electric field causes the electrons being collected at other electrodes than the anode strip. The result is that a sinal is induced at the planar electrode but not on the anode strip. This area is named as "dead-zone" and more elaborated explanation is given in Chapter 3. In this dead-zone, due to the non-uniform electric field, the planar electrode signal can fluctuate. The dead-zone effect is shown in Fig. 2.8 as well. The dark area between the anode strips is in fact correlated with data shown in Fig. 2.7. In this dark area, the electrons are collected by other then the anode strip because of the electric field distribution.

3

CdZnTe drift strip detector

Detectors based on CdZnTe have many desirable properties. High average Z causing high probability for full-energy deposition; large energy band gap enabling operation at room temperature; low energy needed for creation of an electron-hole pair giving high energy resolution. These properties make CdZnTe a strong candidate as detector material for high energy X-ray and gamma ray instrument for space astronomy. The combination of large collecting area, and sensitivity to higher energy X-rays and gamma rays will make it possible for astronomers to uncover the high-energy nuclear line emission distributed in the space.

3.1 Introduction

Although CdZnTe material has many desirable properties for use as room temperature semiconductor detector material, it has also some drawbacks. Even for the best CdZnTe material available, the charge transport properties of holes are poor compared to that of electrons. The mobility-lifetime ($\mu\tau_h$) product for holes is much lower than the mobility-lifetime ($\mu\tau_e$) product for electrons in the CdZnTe crystals, which can result in poor charge collection and degraded energy resolution. For a given detector geometry and applied electric field, the mobility-lifetime products of the detector material determine the mean drift

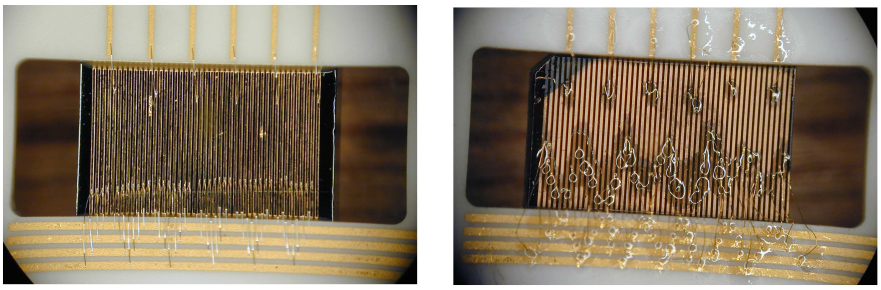

Figure 3.1 Electrical connections (wire bonded) and the drift strip configuration is shown for the GSFC-cZT-4 (left) and for the BSI-CZT-2 (right).

length λ of the charge carriers and are given by:

$$\begin{aligned} \lambda_e &= \mu\tau_e\mathbf{E} \\ \lambda_h &= \mu\tau_h\mathbf{E} \end{aligned} \tag{3.1}$$

where $\mathbf{E}$ is the electric field within the detector. If the mean drift lengths of the charge carriers are comparable to or smaller than the physical detector thickness, then incomplete charge collection will occur within the detector. Thus, the induced charge signal on the collecting electrodes that depends on the drift length of charge carriers, will be strongly influenced by the ionizing radiation interaction depth. The result of the incomplete charge collection effect in a conventional detector having planar electrodes is that the induced charge on the collecting electrodes will be reduced and the deposited energy cannot be obtained uniquely from the induced charge signal. This reduction will appear as a "tail" on the low-energy side of the peak on the spectrum.

The transport properties of electrons are much better than that of holes in a CdZnTe detector. The electron mean drift length λ_e in a CdZnTe detector is order of few cm under nominal operating conditions with a moderate mobility-lifetime product ($E \approx 1000\ V/cm$ and $\mu\tau_e \approx 5 \times 10^{-3}\ cm^2/V$). Therefore, the electrons are nearly fully collected for interactions occurring throughout the detector volume for a detector having thickness of few mm. However, the hole mean drift length λ_h is in the order of few hundred microns. Therefore the holes are severely trapped within the detector. For thick detectors ($d > 0.5$ cm) having a poor $\mu\tau_e$, the fluctuation in electron trapping as function of depth can affect the peak shape and degrade the energy resolution of the detector as

well.

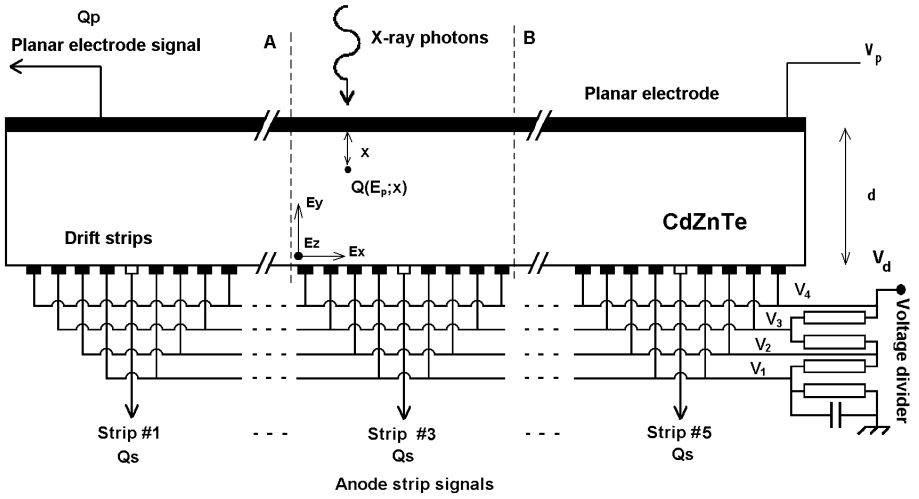

Figure 3.2 A cross-section of a detector using the principle of the drift strip method (DSM) is shown. The drift strip electrodes are biased in such a way that the electrons move to the anode strips.

In order to solve the problem with inefficient hole collection in a CdZnTe detector and knowing that the electrons are being efficiently collected, one can modify the electrode design with geometrically weighted contacts and can make the induced signal on collecting electrodes dependent primarily on the electrons´ drift. This detector concept was first introduced in 1987, by J. Kemmer and G. Lutz applied on Si. The detector consisted of a single-sided strip electrode structure configured as drift detector on one side and a planar electrode on the other side of a Si semiconductor material. Details can be found in [6] and [7].

In this thesis, this approach is applied on a number of CdZnTe detector material. In order to conduct the investigations three CdZnTe drift strip detectors and two CdZnTe drift pixel[1] detectors were designed and fabricated. The CdZnTe crystals were all obtained from eV-products. The detectors were specified to be spectrometer grade single crystals with a size of 10 mm x 10 mm x 3 mm. All the detectors were specified consistently to have a thickness of 3 mm, but in our laboratory, the thickness was measured as 2.7 mm for the

[1] The drift strip detectors have one dimensional position information while the pixel detectors have two dimensional pixel position using the same method as DSM's drifting electrode function in pixel form. These pixel drift detectors are elaborated in Chapter A.1.

GSF-CZT-1 detector [2]. These detectors were named as GSFC-CZT-1, GSFC-CZT-4, BSI-CZT-2, eV-CZT-1 and eV-CZT-2 after the company or the institute where the contacts were deposited on them (i.e., electrodes were deposited on GSFC-CZT-1 at Goddard Space Flight Center (GSFC)). All the CdZnTe drift strip detectors, fabricated at Goddard Space Flight Center, (GSFC) have the same electrode geometry. The deposited electrodes for the GSFC detectors were a Pt planar electrode with a size of 10 mm x 10 mm on one side and 9.5 mm long Pt/Au strips with 0.2 mm pitch and 0.1 mm wide on other side (total 45 strips). The strip electrodes consisted of sputtered platinum followed by a layer of gold for electrical connection by wire bonding. Detailed information concerning the fabrication of CdZnTe strip detectors can be found in [23]. All the CdZnTe drift strip detectors fabricated at Baltic Scientific Instruments[3] (BSI) have a Pt planar electrode with a size of 10 mm x 10 mm and 9.5 mm long Au strips with 0.2 mm pitch, 0.1 mm wide (total 49 strips). A number of ceramic supports were designed and fabricated for the detectors. All the detectors from GSFC and BSI were glued on a ceramic support. The electrical connections of the collecting electrodes and the bias arrangement of the drift strips were done by wire-bonding. In Fig. 3.1, two images showing the wire-bonding work for the GSFC-CZT-4 and the BSI-CZT-2.

These detectors were used commonly to investigate the functionality of the DSM. The main goal of this research was to investigate CdZnTe drift strip detector systems for space application. Therefore, the GSFC-CZT-1 detector was used to test the influence of the radiation damage induced by the energetic charged particles and to understand the effect of the radiation damage on the detector performance. Another research was conducted in connection with the negative impact of the grain boundaries on the detector performance. The BSI-CZT-2 detector was especially investigated for this purpose since it has shown a significant spectral non-uniformity behavior and is suspected to suffer spectral performance degradation caused by the grain boundaries. The results were presented in the previous chapter.

The DSM was applied as a pixel geometry and finally, the eV-CZT-1 and the eV-CZT-2 were designed and ordered from eV-products in the beginning of the last year of this research. The fabrication of the detectors were considerably behind schedule due to complicated electrode geometry and electrical connections which took longer time than planned. Furthermore, even though the detectors were fabricated, they could not be received in time, due to the unexpected obstacles such as formalities. While completing this thesis, the

[2] The GSF-CZT-1 detector was used for the radiation damage experiment. Therefore, the thickness of the detector was an important physical parameter. The experiment is elaborated in Chapter 4.

[3] Baltic Scientific Instruments is located in Riga, Latvia.

detectors were not received. It was planned to use an Application Specific Integrated Circuit (ASIC) chip from eV-products as a read-out electronic for the CdZnTe drift pixel detector. This project was planned and started in the last year of this Ph.D study, however, due to unforeseen circumstances (e.g., many redesigned test boards due to poor documentation from the ASIC manufacturer and lack of technician time due to priorities) the project was delayed and was finished only 3 weeks before the dead line of this thesis. The drift pixel geometry and the ASIC chip can be seen in Appendix A.

3.2 Drift strip method (DSM)

The drift strip method (DSM) is based on modified and geometrically weighted electrode design. The electrode design is changed so the weighting field within the detector is changed such that the contribution of the holes with their poor transport properties to the induced signal on the electron collecting electrode is reduced. This makes the drift strip detectors sensitive to electron charge carrier collection and less sensitive to hole charge carrier collection. Therefore, the DSM prevents degradation of the signal by inefficient hole collection. The principle of the DSM is shown schematically in Fig. 3.2. The structure consists of a planar electrode on one side and strips on the other[4]. Total number of strips are configured as drift detector cells with a group of 9 strips. A drift strip detector cell is shown between the dashed lines marked with A and B in Fig. 3.2. Each drift detector consists of 8 drift strip electrodes and one anode readout strip. The drift strip electrodes are biased by a voltage divider that supplies each drift strip with a bias of Vi=Vd*(i/4), whereas the anode strips are held at ground potential. The drift strip electrodes are named by Vi. The GSFC-CZT-1 detector has five independent drift detectors. This detector was designed and fabricated as the first DSRI strip detector. For the drift strip configuration, two V4 drift strips were used each for two adjacent drift detector cell in this detector. For the other detectors (GSFC-CZT-4 and BSI-CZT-2), only one V4 drift strip is used as a common drift strip for two adjacent drift detector cell. This is applied on all the other detectors fabricated and used in this thesis except the pixel drift detectors and the total number of independent drift detector cell is six on these detectors.

The DSM has two considerable characteristics which separate it from a conventional planar detector. The electric field and the weighting field in a DSM are not uniform as they are in a planar detector. The result of these characteristics are as follows:

[4] All the CdZnTe drift strip detectors fabricated and used in this thesis have this electrode geometry. The total number of strips are 45 or 49 for GSFC and BSI CdZnTe drift strip detectors respectively.

1. Due to the small-area anode strip relative to the thickness of the detector, the anode strip weighting potential is very low within most of the detector volume, and rises sharply to 1 near the anode strip. Therefore, the anode strip signal will not be dependent on the movement of the holes (unless the interaction occurs in the immediate vicinity near the anode strip where the total induced signal on the anode strip would be dependent on the both carriers movement) in the detector volume where weighting potential is small. Thus, the sensitivity to the trapping of holes is strongly reduced. In general, this weighting potential effect is called the "small pixel effect" in the field. If the trapping of electron is negligible, the anode strip signal is then independent of the interaction position. The detector is only sensitive to electrons and therefore is called a "single polarity charge sensing detector". For the planar electrode, the weighting potential within the detector is uniform. Therefore, the induced charge on the planar electrode is dependent on the both carriers´ movement within the detector volume. As the holes are trapped and the contribution to the induced signal can be neglected (assuming that the holes are completely trapped and can not contribute to the total induced signal on electrodes), the induced signal on planar electrode will be dependent on the depth of interaction. In fact, this characteristic of the planar electrode signal is important when providing depth of interaction is considered.

2. In practice, the finite size of the anode strip generates a non-ideal weighting potential distribution within the detector. In an ideal case, the weighting potential distribution will limit to a delta function as the anode strip size goes to 0. The electron-induced charge on the anode strip may fluctuate due to electron trapping and the non-ideal weighting potential within the detector. These fluctuations depend on the interaction positions within the detector due to the short electron mean drift length λ_e which depends on the electric field and the non-ideal weighting potential in the detector bulk. The fluctuation on the anode strip signal can be compensated using the depth information.

3. The electric field lines determine the drift path of the charge carriers during the collection process and the charge carriers are collected by those electrodes which the electric field lines start and end. Depending on the ratio of the operation voltages Vp/Vd and the electrode geometry of the drift detector cell, an undesirable effect, a so-called "dead-zone" can occur for the anode strip, due to the electric field. The dead-zone is defined as the positions within the drift detector cell where the electrons are being collected by other than the anode strip electrode (assuming that the holes are completely trapped). For the interactions in the dead-zone,

the electron-induced charge are induced only on the electron collecting drift strip and on the planar electrode. Due to the nature of the drift strip bias voltages, the mean drift length of the electrons can vary as the electric field can vary across the drift strips as well. Therefore, the signal can fluctuate in the dead-zone for the planar electrode. In contrast, a so-called "active-zone" is defined as the positions within the drift detector cell where the electrons are being collected by the anode strip electrode. The signal may also fluctuate due to electron drift path length fluctuation across the drift detector cell in the active-zone.

These characteristics are elaborated with calculations in the following:

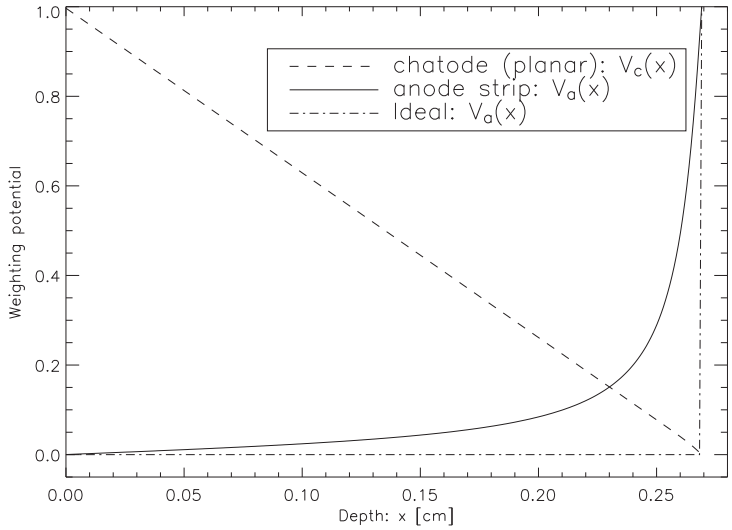

Figure 3.3 The weighting potential values for the planar electrode $V_c(x)$ and the anode strip electrode ($V_a(x)$)are calculated. The calculation is performed for the GSFC-CZT-1 drift detector. However, the results are shown for the center position on the anode strip for the drift detector cell between the dashed lines marked with "A" and "B" (shown in Fig. 3.2). The "ideal" case of the weighting potential function is also illustrated in the plot. For the ideal weighting potential function, the size of the strip determines the weighting function and as the strip size goes to zero the weighting function becomes zero for the bulk of the detector and becomes 1 at the strip electrode

The weighting potential values for the planar electrode $V_c(x)$ and the anode strip electrode ($V_a(x)$) are calculated and shown in Fig. 3.3. The calculation is

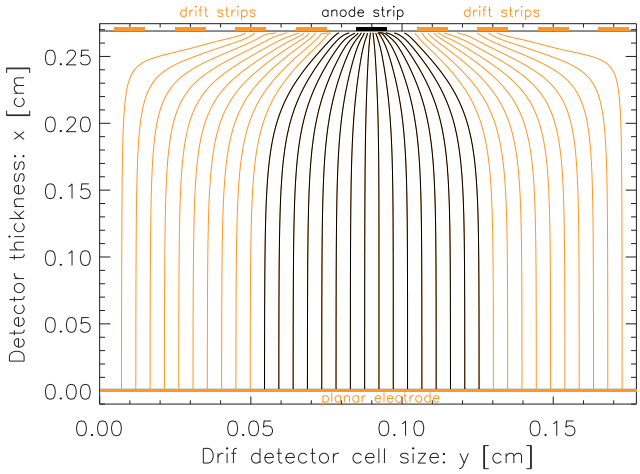

Figure 3.4 The electric field lines are calculated for Vp=-300V and Vd=-100V. These lines are also the carriers' drift path during the charge collection process. Almost 50% of the field lines end on the anode strip and the standard deviation of the drift path length across the detector cell is around $\sim 100\mu m$. Those field lines (red color) end on the drift strips covering an area (the dead-zone) in the detector. Contrary, those field lines (black color) end on the anode strip covering an area (the active-zone) in the detector. In the active-zone, the electrons are being collected by the anode strip electrode. The size of the dead-zone is dependent on the ratio of the operation voltages Vp/Vd and the electrode geometry of the drift detector cell, and it can be changed by changing the bias condition as illustrated in Fig. 3.5 or the electrode geometry.

performed for the GSFC-CZT-1 drift detector. Only the results are shown for the center position on the anode strip for the drift detector cell between the dashed lines marked with "A" and "B" (shown in Fig. 3.2). The "ideal" case of the weighting potential function is also illustrated in the plot. For the ideal weighting potential function, the size of the strip determines the weighting function and as the strip size goes to zero the weighting function becomes zero for the bulk of the detector and becomes 1 at the strip electrode.

The effect of the electron trapping and the non-ideal weighting potential can be adjusted to compensate the anode strip signal fluctuation as function of depth. For the weighting potential, a very small electrode size can be designed in order to achieve small weighting potentials for the bulk of the detector, which then sharply rises to 1 near the anode strip. In practical, this is difficult to achieve. Considering the technological limitation the size of the anode strip

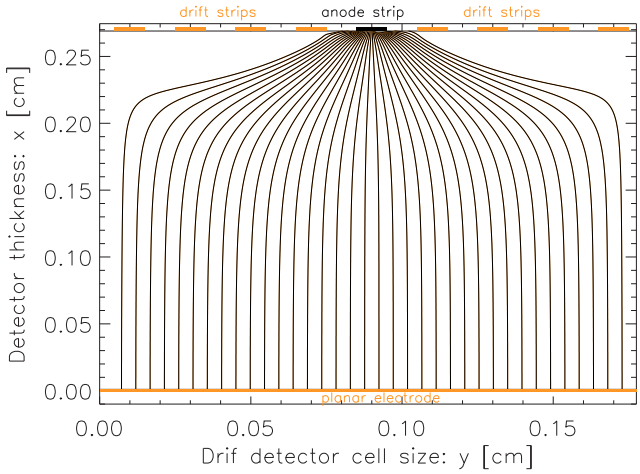

Figure 3.5 The electric field lines for (Vp,Vd)=(-150V,-100V) are calculated. All calculated field lines end on the anode strip. The standard deviation of the drift path across the detector cell is around $\sim 170\mu m$. The dead-zone is reduced across the detector cell.

can not be smaller than the area necessary to make electrical connection to the external electronic. The metal contact depositing process on the detector material has also its limitation with respect to making the uniform small area contacts on the detector surface. The electronic noise caused by the surface leakage current is also a design criterion for strip detectors. A higher surface leakage current is consequently a higher electronic noise in the read-out system. The electron trapping adjustment within the detector can be a material science issue (the charge transport properties of the detector material can be enhanced), but it can also be adjusted by changing the applied electric field. For the poor $\mu\tau_e$ values, an optimal detector operation bias voltages can be used in order to reduce the peak broadening caused by electron trapping as function of interaction depth. This is limited by the detector leakage current. For a detector with a good $\mu\tau_e$ value, the electron trapping effect can be negligible and then the non-ideal weighting potential effect will make the induced anode strip signal Qs dependent on the interaction depth.

To emphasize the variation of the carrier's drift path length as a function of operation voltage and the variation of the sensitive detector area, the electric field lines are calculated for the operation voltages (Vp,Vd)=(-300V,-100V) and (Vp,Vd)=(-150V,-100V). Fig. 3.4 shows the calculated electric field lines for (Vp,Vd)=(-300V,-100V). Almost 50% of the field lines end on the anode

strip with a standard deviation of the drift path length of $\sim 100\mu m$. When an interaction occurs in the dead-zone, the electrons will drift and be collected by any other electrode than the anode strip. Then the integrated current along the electron path will be equal to zero for the anode strip signal while the signal on the planar electrode will "see" the drifting electrons and full charge signal will be induced on it. The change of the dead-zone by changing the bias condition is illustrated in Fig. 3.5. Here, the electric field lines for the operation voltages (Vp,Vd)=(-150V,-100V) are calculated. For these operation voltages the dead-zone is reduced significantly. All calculated field lines end on the anode strip. The standard deviation of the drift path across the detector cell is around $\sim 170\mu m$.

The effect of the variation of the carrier's drift path length to the detector performance is illustrated with experimental data in section 3.7.3.

As can be seen, a number of detector parameters, in order to optimize the detector performance, are dependent on each other in a complex way. However, a detector model can be a powerful tool for designing a specific detector by optimizing those parameters.

3.3 The depth information and the bi-parametric distribution

The effect of the hole trapping combined with the single polarity charge sensing ability can be used to obtain the radiation interaction depth information between the planar electrode and the anode strip. The depth information can be obtained from the ratio R between the planar electrode signal Q_p and the anode strip signal Q_s. The planar electrode signal Q_p is linear dependent on the dept x, as shown in Fig. 3.3. Assuming that the holes are completely trapped and their contribution to the signal can be neglected then the ratio R becomes ≈ 1.0 for interactions close to the planar electrode or detector surface and becomes ≈ 0.0 for interactions near the strip electrodes. If the charge diffusion effect is ignored for the charge cloud generated by the photon interaction, then the accuracy of the depth resolution is primarily governed by the non-correlated electronic noise and by the limited accuracy of the pulse-hight measurements in the read-out system (independent read-out electronic for planar electrode and anode strips). This is true in most of the detector bulk but it becomes dependent on the non-ideal weighting potential close to the anode strip. On the other hand, for high energy photons, the photoelectron or the Compton electron range within the detector becomes significant parameter.

The depth information can be used to correct the anode strip signal fluctuation caused by the electron trapping effect and the non-ideal weighting potential

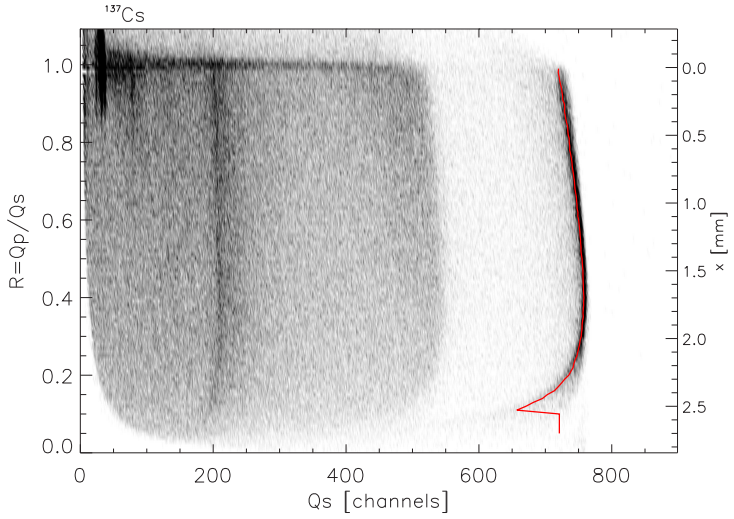

Figure 3.6 The bi-parametric distribution ($R = Qp/Qs$ versus Qs) recorded from a ^{137}Cs source. The detector is GSFC-CZT-1. The signal from anode strip 3 and the planar electrode is used. The peak position of 661.6 keV line distributed within the detector (located between 600 to 800 channels in Qs) was fitted with a Gaussian function for each R values. The mean value of the peak position as function of depth was shown with a red solid line. The operation voltages were $Vp = -100V$ and $Vd = -50V$ for the planar electrode and the drift bias respectively. The operating temperature was 22 ^oC. The shaping time was adjusted to 1 μs for all shaping amplifiers. The shape of the the mean value of the peak position as function of depth is due to the non-ideal weighting potential and the electron trapping effect within the detector.

effect. As an example, a bi-parametric distribution ($R = Qp/Qs$ versus Qs) recorded from a ^{137}Cs source using GSFC-CZT-1 detector is shown in Fig. 3.6. The peak position of 661.6 keV from the source (located between 600 to 800 channels in Qs along the R values) distributed within the detector was fitted with a Gaussian function for each R values (approximately down to 2.5 mm). The mean value of the peak position as function of depth R is shown with a red solid line. Electron trapping can be observed from the significant decrease in pulse hight with increasing electron drift distance as shown in Fig. 3.6. The detector was operated with a planar electrode bias of $Vp = -100V$ and a drift strip bias of $Vd = -50V$. These operation voltages were selected intensionally to show the effect of the electron trapping. The effect of the electron trapping is noticeable as the drift distance of the electrons is increased and it is the

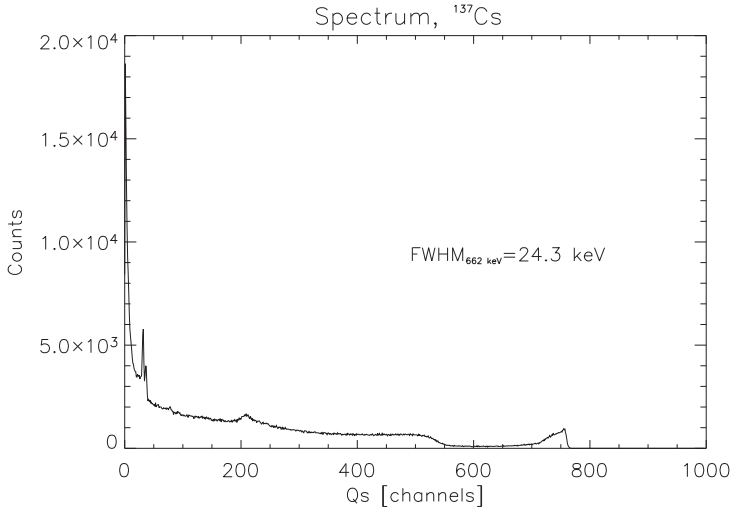

Figure 3.7 The energy spectrum of ^{137}Cs obtained from the whole bulk of the detector by the anode strip signal. The energy resolution is 24.3 keV FWHM at 661.6 keV.

dominant effect for the shape of the the mean value of the peak position as function of depth in Fig. 3.6. The effect of the non-ideal weighting potential is significant close to the anode strip. The sharp drop in photo peak height near the anode surface is caused by the non-ideal weighting potential in the vicinity of the anode strip surface.

The energy spectrum of ^{137}Cs obtained from the whole bulk of the detector by the anode strip signal is shown in Fig. 3.7. Here, the $Q_s(R)$ yielded energy resolution of 24.3 keV FWHM at 661.6 keV. This large value can be explained by the electron trapping effect within the detector.

The anode strip signal $Q_s(R)$ can be corrected for the electron trapping effect and the non-linear weighting potential effect using the bi-parametric distribution. The correction method is as follows: A tabulated R versus Qs relation $\overline{Q_s^t(R)}$ can be obtained by fitting 661.6 keV line with a Gaussian function for each R value in the bi parametric distribution, illustrated in the Fig. 3.6 as the solid red line. The red line is the mean peak position values as function of depth. The ratio value R_0, which corresponds to the physical surface of the detector is also obtained after the fitting process. Once the R versus Qs relation, which is dependent on detector geometry and operation voltages, is obtained it can be used for correction of $Q_s(R)$ for all energies.

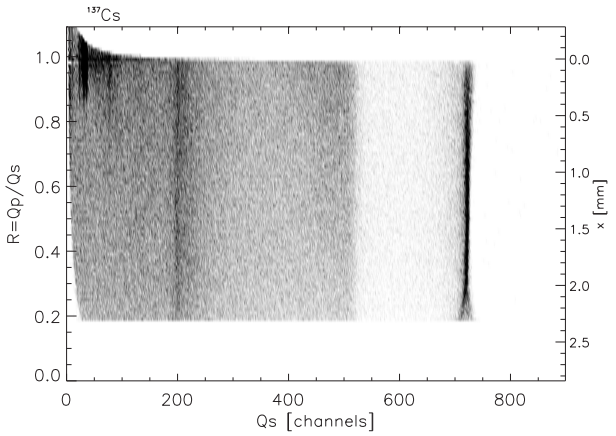

Figure 3.8 The bi-parametric spectra shown in Fig. 3.6 is corrected event by event using the algorithm given in Eq. (3.2). Correction was applied only for the depth between 0 and 2.3 mm.

The correction algorithm is described as:

$$Q_s^c(R) = \frac{\overline{Q_s^t(R_0)}}{\overline{Q_s^t(R)}} Q_s(R) \tag{3.2}$$

where $Q_s^c(R)$ is the corrected anode signal, $\overline{Q_s^t(R)}$ is the mean peak position as function of depth for 661.6 keV line and $\overline{Q_s^t(R_0)}$ is the mean peak position value at the surface of the detector.

The correction is performed for the bi-parametric distribution shown in the Fig. 3.6. Fig. 3.8 shows the corrected bi-parametric distribution event by event down to a depth of 2.3 mm. The correction fails for events close to the strips. Here, other effects play significant roles due to the electrode geometry (non-uniform electric field and non-ideal weighting potential close to the strips). These effects cause an asymmetric peak broadening for the R values between 0 to 0.3 as can be seen in Fig. 3.6. After the correction, the corrected spectrum was obtained by integrating $Q_s^c(R)$ for all R values in the corrected bi-parametric distribution. The result, as shown in Fig. 3.9, is yielded energy resolutions of 6.8 keV FWHM at 661.6 keV.

In general, this correction technique can also be applied for other novel electrode designs based on the single carrier charge sensing technique [29].

The drift strip method (DSM) applied to the CdZnTe detectors with moderate $\mu\tau_e$ leads to a dramatic improvement of the achievable energy resolution.

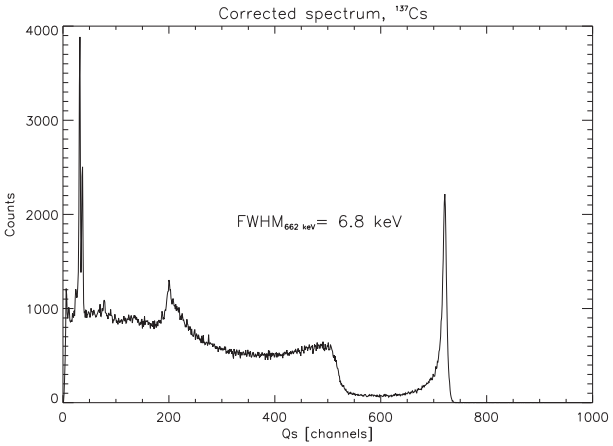

Figure 3.9 The corrected spectrum of ^{137}Cs for depth between 0 and 2.3 mm.

The DSM does not require event rejection as the pulse processing techniques does. This can be an important property especially for space applications for statistical reasons.

3.4 The electric field and the weighting field for the CdZnTe drift strip detectors

The electric field and the weighting field within the CdZnTe drift strip detector must be determined in order to describe the DSM with a numerical model. This section contains a numerical electrostatics analysis of the CdZnTe drift strip detector assumed to have Ohmic contacts. Although, in practice the contacts on the CdZnTe detector can deviate from pure Ohmic behave, this assumption was necessary to go trough the electrostatic calculation. The contacts on CdZnTe material was elaborated in Sec. 2.3.2.

The electrostatic analysis was performed on the GSFC-CZT-1 detector using the detector's physical dimensions and the electrode geometry. Numerical calculations have been performed using the 2D electric field simulation program ELFI [30], which is based on the theory of discrete Maxwell grid equations. With this program, using the simple geometrical components (e.g., line, rectangle, circle), a two dimensional detector geometry with a semiconductor material and a number of conductor describing the GSFC-CZT-1 was drawn. A semiconductor material representing the CdZnTe material was defined in the

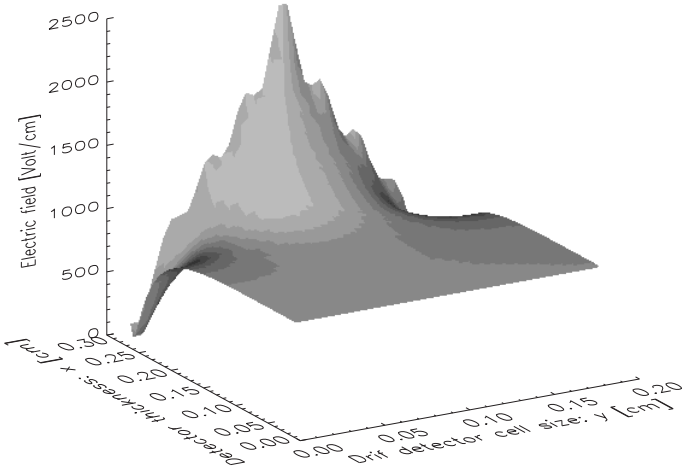

Figure 3.10 The calculated electric field distribution within the detector. The bias voltage settings were Vp=-300V and Vd=-100V.

ELFI using the CdZnTe permittivity of $\varepsilon_s = 10.9$ (from Tab. 1).

The electric field was then calculated for various operation voltages. The weighting potential distribution was calculated for the planar electrode and the anode strip electrode. For the weighting potential calculation, the collecting electrode potential was set to 1 volt and all the other electrodes were set to 0 volt.

The calculated electric field data is shown in Fig. 3.10 for the drift strip detector cell which is shown between the dashed line marked with A and B in the Fig. 3.2. The non-uniformity of the electric field can be seen close to the strips. Due to the relation $v = \mu\mathbf{E}(\mathbf{x})$, the electron drift velocity will be larger close to the anode strip. From the Eq. (3.1), the electron mean drift length $\lambda_e(\mathbf{x}) = \mu\tau_e\mathbf{E}(\mathbf{x})$ is therefore dependent on the depth.

The calculated weighting potential for the anode strip as the collecting electrode is shown in Fig. 3.11. Here, the weighting potential close to the anode strip rises rapidly to unity. Fig. 3.12 shows the calculated weighting potential for the planar electrode as collecting electrode. The weighting potential is linear dependent on the dept x.

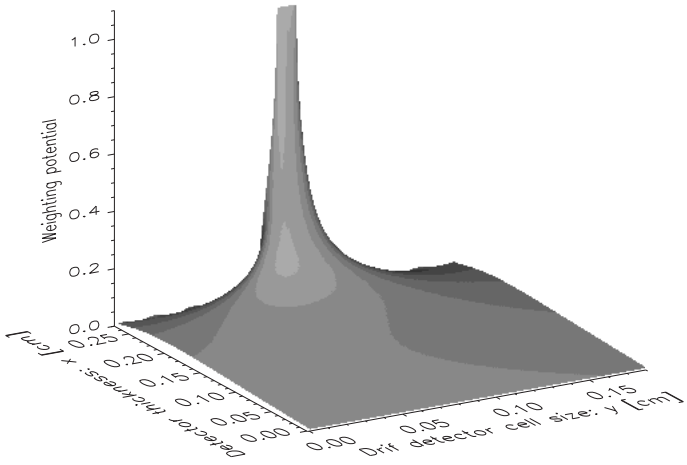

Figure 3.11 The weighting potential distribution within the detector calculated for the anode strip as the collecting electrode.

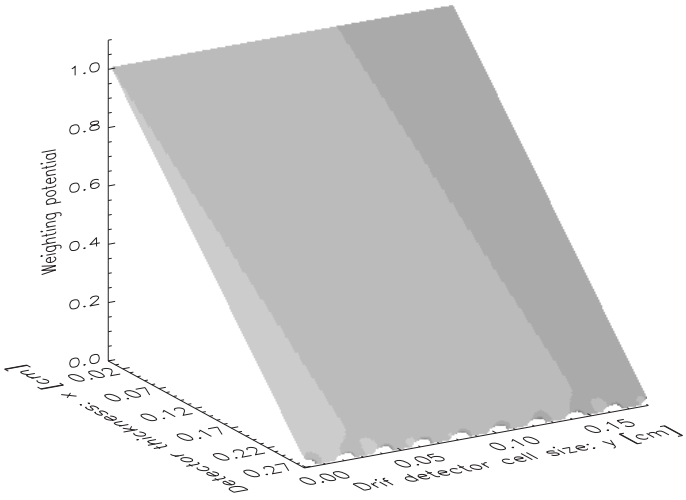

Figure 3.12 The weighting potential distribution within the detector calculated for the planar electrode as the collecting electrode.

3.5 A signal formation model for the drift strip detectors

In order to model the responds of the CdZnTe drift strip detector, the physical processes, the charge collection under the influence of the applied electric field and the signal formation must be described for a given detector geometry. The signal formation on the electrodes for the drift strip detector differs from a conventional planar electrode detector as the electric field and the weighting potential distribution are not uniform due to the electrode geometry. The equations, describing the charge collection for a detector with multi electrodes should ideally be solved for three-dimensional geometry. For the CdZnTe drift strip detectors, these equations are coupled to geometry in two-dimensional due to the parallel strip geometry (assuming long strips and uniform material properties). From the Fig. 3.2, one can see that the weighting potential and the electric field along the strips (in z-direction) would not vary if infinite uniform material and contacts are assumed. In practice, this assumption is partly true only for locations far from the detector edges otherwise the weighting potential and the electric field will be affected by the edge of the detector.

The equations, describing the charge collection for a detector with multi electrodes are as follows:

The total charge induced on an electrode due to the collection of $Q_e = -qN_0$ and $Q_h = qN_0$ (where $N_0 = E_p/\omega$ is the number of electron-hole pairs) can be obtained by integrating the change in the induced charge $\triangle Q_{ind}$ over the path of the charge from its origin to the collecting electrode for each carrier type and summing their contribution ($Q_{ind,e}$ and $Q_{ind,h}$) :

$$Q_{ind,tot}(E_p;\mathbf{x}) = Q_{ind,e}(E_p;\mathbf{x}) + Q_{ind,h}(E_p;\mathbf{x}) \tag{3.3}$$

The photon energy, E_p, determines the size of the primary charge cloud $Q(E_p;\mathbf{x})$. The induced charge signal on the collecting electrodes can be calculated by using the theorem of Ramo [13], which uses the weighting potential. The weighting potential (dimensionless) is defined as the potential that would exist in the detector with the collecting electrode at "unit" potential while holding all other electrodes at zero potential. The induced charge $Q_{ind}(E_p;\mathbf{x})$ is determined by the weighting field and it is independent of the operating electric field. The weighting field $\mathbf{E}_w(\mathbf{x})$ is the gradient of the the scalar weighting potential $V_w(\mathbf{x})$ and it is given by:

$$\mathbf{E}_w(\mathbf{x}) = -\nabla V_w(\mathbf{x}) \tag{3.4}$$

The trajectory of the charge carriers are determined by the operating electric field $\mathbf{E}$. The electric field $\mathbf{E}$ is the gradient of the scalar potential $V(\mathbf{x})$ and

it is given by :

$$\mathbf{E}(\mathbf{x}) = -\nabla V(\mathbf{x}) \tag{3.5}$$

The induced charge Q_{ind} at an electrode is the charge of the charge cloud $Q(E_p;\mathbf{x})$ times the weighting electric field integrated over the path of the charge cloud:

$$Q_{ind}(E_p;\mathbf{x}) = \int Q(E_p;\mathbf{x},\mathbf{s})\mathbf{E}_w(\mathbf{s}) \cdot d\mathbf{s} \tag{3.6}$$

where $\mathbf{s}$ is the center of the charge position of the charge cloud in the crystal. The effect of the trapping is taken into account by making $Q(E_p;\mathbf{x})$ a decreasing quantity in the integration. The amount of trapping at any point is governed by the trapping length of the charge carriers, which is given in Eq. (3.1). Taking non-uniformly distributed charge traps (e.g., reflecting the damage profile generated by the proton irradiation) into account, charge trapping lengths $\lambda(\mathbf{x})$ must be used, which are dependent on $\mathbf{x}$. The charge trapping are then described by:

$$Q(E_p;\mathbf{x},\mathbf{s}) = Q(E_p;\mathbf{x}) \exp(-\int_{\mathbf{x}}^{\mathbf{x}+\mathbf{s}} \frac{d\mathbf{t}}{\lambda(\mathbf{t})}) \tag{3.7}$$

where the integration is made over the trajectory of the charge cloud. The trapping length, $\lambda(\mathbf{x})$ of Eq. (3.7) can be expressed by:

$$\lambda(\mathbf{x}) = \mu\tau(\mathbf{x})\mathbf{E}(\mathbf{x}) \tag{3.8}$$

where $\mathbf{E}$ $(\mathbf{x})$ is the electric field inside the detector.

The induced charge Q_{ind} on any detector electrode can now be found solving Eq. (3.6) using Eq. (3.7) and Eq. (3.8). The following section describes a numerical computer model for the CdZnTe drift strip detector using these equations.

3.6 A numerical computer model for the CdZnTe drift strip detector

All the processes explained in the previous section are used to describe the CdZnTe drift strip detector´s response with a simple mathematical detector model. A numerical computer model for the CdZnTe drift strip detector using the mathematical detector model is developed. In order to reduce the complexity of the solution, the symmetry of the geometry together with a few assumption were used. First, the electric field and the weighting potential are assumed to be constant parallel to the strips. Therefore, the electric field and

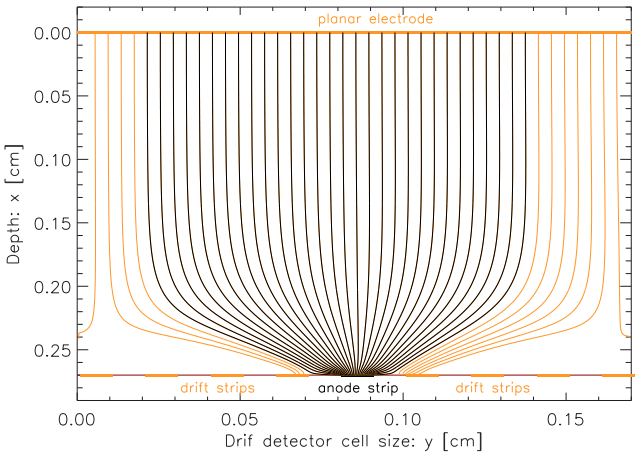

Figure 3.13 The model calculates a number of electric field lines for the GSFC-CZT-4 detector from the precalculated electric field data (calculated using ELFI program) for Vp=-150V and Vd=-100V. These lines are also the carriers' drift path during the charge collection process. Those field lines end on the drift strips (red color) covering an area in the detector which is called a dead-zone. When an interaction occurs in the dead-zone, the electrons will drift and be collected by other than the anode strip. In contrast, a so-called active-zone is defined as the positions within the drift detector cell where the electrons are being collected by the anode strip electrode. This is illustrated with field lines ending on the anode strips (black color). The induced charge on the planar electrode and the anode strip are calculated with a spatial step of 100 μm on these lines. The model result is illustrated as a bi-parametric distribution in Fig. 3.14 for comparison to the experimental data.

the weighting potential were calculated in two-dimensional for the cross-section of the drift detector cell. Secondly, the generated charge cloud was assumed to be point like and the charge diffusion effect was not taken in to account in the model.

The numerical computer model uses precalculated data from the electrostatic analysis using the detector geometry and the operation voltages. The precalculated data are the electric field $\mathbf{E}(\mathbf{x})$, the weighting potential $\mathbf{V}w, a(\mathbf{x})$ data for the anode strip electrode and the weighting potential $\mathbf{V}w, c(\mathbf{x})$ data for the planar electrode. The transport properties for the electron $\mu\tau_e$ and the hole $\mu\tau_h$ are also the input parameters for the model. The $\mu_e = 1000\ cm^2/Vs$ and the $\mu_h = 80\ cm^2/Vs$ for the CdZnTe material are used as constants in the computer model (from Tab. 1).

The model calculates the Q_{tot} on the detector electrodes by simulating the

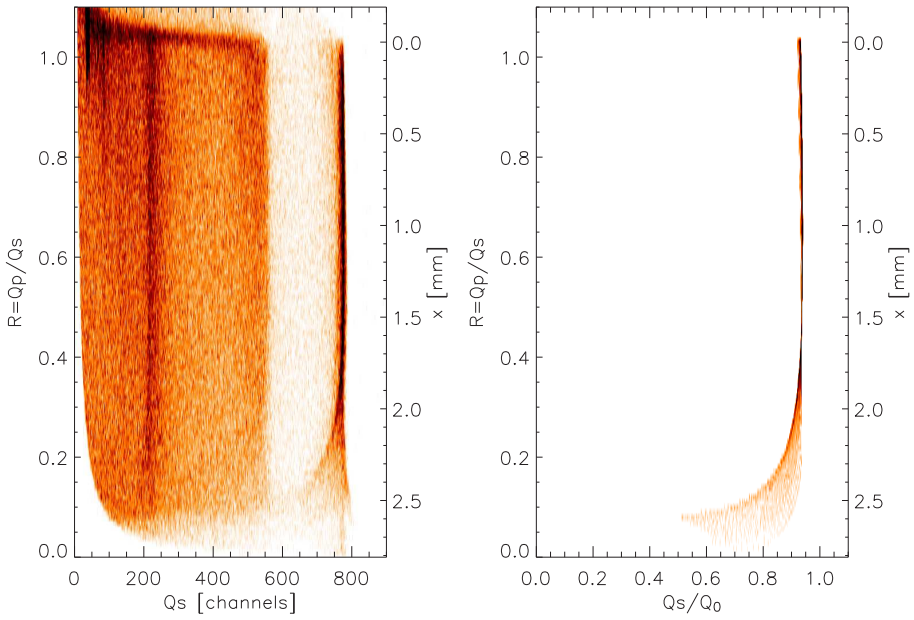

Figure 3.14 Comparison between the experimental data and the numerical computer model for the CdZnTe drift strip detector. The left plot is the bi-parametric distribution of a ^{137}Cs source obtained by the GSFC-CZT-4 detector. The applied bias voltages are Vp=-150 V and Vd=-100 V. The operating temperature is 22 ^oC. The shaping time is $1\mu s$ for all the shaping amplifiers. The right plot is the numerical computer model data. The $\mu\tau_e = 8 \times 10^{-3}$ (cm^2/V) was measured for the GSFC-CZT-4 detector and used in the model. The $\mu\tau_h = 5 \times 10^{-5}$ (cm^2/V), the $\mu_e = 1000$ cm^2/Vs and the $\mu_h = 80$ cm^2/Vs for the CdZnTe material are used as constants in the computer model (from Tab. 1). The right hand axis show the depth in mm.

charge carriers´ collection from the start position to the collecting electrodes and takes the charge trapping into account during the collection process. The equations Eq. (3.6), Eq. (3.7) and Eq. (3.8) were used in the model. The model calculates a number of electric field lines (e.g., illustrated in Fig. 3.13) for the detector from the precalculated electric field data (ELFI program). The model first calculates for each electric field lines, between the planar electrode and the anode strip electrode, a trajectory (drift path) of the charge carriers, $\mathbf{s}$ ($\mathbf{s}$ is a set of points on electric field lines) with a constant spatial step of $|d\mathbf{s}| = 0.9\mu m$ in the direction of the electric field line $\mathbf{E}(\mathbf{s}_i)$.

For each trajectory, the model calculates four variables corresponding to

that trajectory: a weighting potential distribution $\mathbf{V}w, a(\mathbf{s}_i)$ for the anode strip electrode, a weighting potential distribution for the planar electrode $\mathbf{V}w, c(\mathbf{s}_i)$, a charge trapping length distribution $\lambda_e(\mathbf{s}_i)$ for electrons and finally, a charge trapping length distribution $\lambda_h(\mathbf{s}_i)$ for holes. The model simulates the charge carriers´ collection from a start position to the collecting electrodes and computes the contributions of the displaced charge to the charge induced at the electrodes as $dQ(\mathbf{s}_i) = Q_i \mathbf{V}w(\mathbf{s}_i) \cdot d\mathbf{s}_i$, where Q_i is the displaced charge at step i between $\mathbf{s}_i$ and $\mathbf{s}_i + d\mathbf{s}_i$. The sum of these contributions along the trajectory gives the total induced charge at each electrode. The charge trapping, along the trajectory for each step i, is calculated by modifying Q_i after each step as:

$$Q_{i+1} = Q_i \exp(-\tfrac{d\mathbf{s}_i}{\lambda(\mathbf{s}_i)}) \tag{3.9}$$

where $\lambda(\mathbf{s}_i) = \mu\tau\mathbf{E}(\mathbf{s}_i)$ is the charge trapping length distribution. The total induced charge at an electrode as:

$$Q_{tot} = \sum_i dQ(\mathbf{s}_i) = \sum_i Q_i \mathbf{V}w(\mathbf{s}_i) \cdot d\mathbf{s}_i \tag{3.10}$$

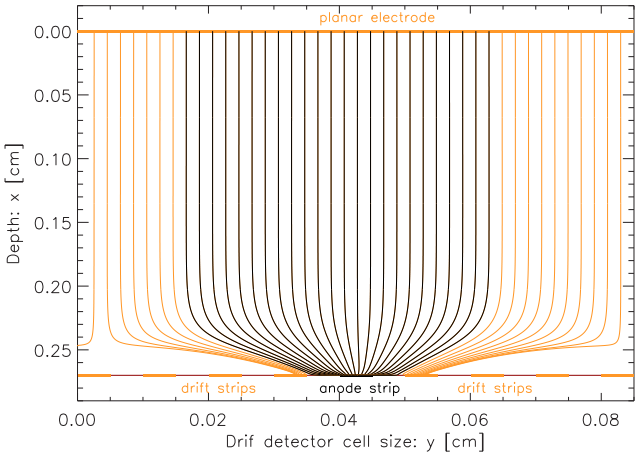

Figure 3.15 The model calculation of electric field lines performed for the GSFC-CZT-4 detector from the precalculated electric field data (calculated using ELFI program) for Vp=-150V and Vd=-100V. The electrode geometry was changed from strips with 0.2 mm pitch and 0.1 mm wide to strips with 0.1 mm pitch and 0.05 mm wide. The bi-parametric distribution is shown in Fig. 3.16, for comparison to the model data shown in Fig. 3.14.

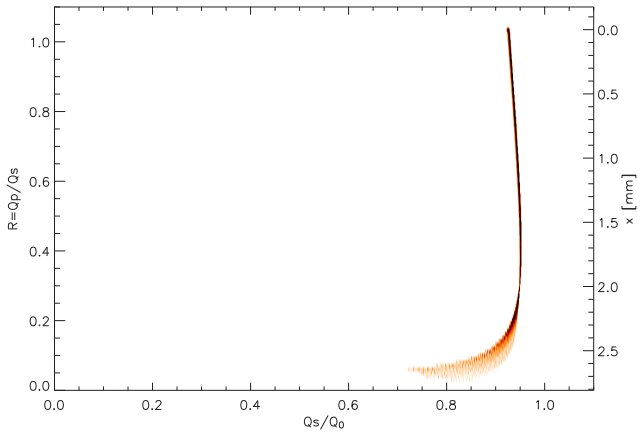

Figure 3.16 The sharp drop caused by the non-ideal weighting potential in curve near the anode surface is now at depth of $\sim$ 2.3 mm compare to the bi-parametric distribution shown in Fig. 3.14. Only the electrode geometry is changed for the GSFC-CZT-4 detector. All other detector parameters are the same.

As an example, comparison between the experimental data and the numerical computer model for the CdZnTe drift strip detector is shown in Fig. 3.14. The left plot is the bi-parametric distribution of a ^{137}Cs source obtained by the GSFC-CZT-4 detector. The applied bias voltages are Vp=-150 V and Vd=-100 V. The operating temperature is 22 ^oC. The shaping time is 1μs for all the shaping amplifiers. The rightmost curve is generated by photo absorption of ^{137}Cs 661.6 keV photons. Compton, backscatter and Ba X-ray events can also be seen towards lower Qs values. The shape of the 661.6 keV line corresponds to the electron trapping and the weighting potential effects. The shape of the 661.6 keV is simulated. The right plot is the numerical computer model data. The $\mu\tau_e = 8 \times 10^{-3}$ (cm^2/V) was measured for the GSFC-CZT-4 detector and used in the model (more detail for the $\mu\tau_e$ measurements can be found in Chapter. 4 section 4.7.2). The $\mu\tau_h = 5 \times 10^{-5}\,(cm^2/V)$, the $\mu_e = 1000\ cm^2/Vs$ and the $\mu_h = 80\ cm^2/Vs$ for the CdZnTe material are used as constants in the computer model (from Tab. 1). The curve in the model data agrees with the shape of the 661.6 keV line in the experimental data except that the model data does not take the electronic noise and the statistical noise components into account. The effect of the non-ideal weighting potential is significant close to the anode strip in both plots. The sharp drop in photo peak height near the anode surface (depth of $\sim$ 2.0 mm is caused by the non-ideal weighting potential. This effect can be reduced by changing the electrode geometry as

illustrated in Fig. 3.15 and Fig. 3.16. The model calculation is repeated using different electrode geometry for the GSFC-CZT-4 detector. The electrode geometry was changed from strips with 0.2 mm pitch and 0.1 mm wide to strips with 0.1 mm pitch and 0.05 mm wide. From the bi-parametric distribution shown in Fig. 3.14, one can see that the sharp drop caused by the non-ideal weighting potential in the curve near the anode surface is now at a depth of ~ 2.3 mm compare to the bi-parametric distribution shown in Fig. 3.14.

3.7 Experimental

Common investigation for all detectors used in this thesis was the functionality of the DSM. The GSFC-CZT-1 and the GSFC-CZT-4 detectors were characterized in detail. The performance of the detectors for X-ray and gamma-ray spectroscopy was evaluated. The spectral response for each detector were measured. Noise measurements were made under optimal operating conditions using a pulse generator. From the standpoint of noise, the optimal amplifier shaping time was found $1\mu s$. This setting was also found to yield the best spectral resolution at 661.6 keV (^{137}Cs) and was used for all of the measurements and spectra presented in this thesis. The conventional read-out electronic (NIM module and standard charge sensitive preamplifiers from ORTEC and eV-products used for nuclear detectors) were used for all the characterization work. All characterization results for the detectors have shown that the energy resolution below 100 keV was limited by the electronic noise. The electronic noise for the conventional read-out electronic at 22^oC were measured to be 2-5 keV FWHM depending on the type of the charge sensitive preamplifier. Therefore, the electronic noise is reduced by designing a read-out electronic, the criteria of the noise sources taken into account. This read-out electronic could perform as low as 0.8 keV FWHM total electronic noise at -10^oC. This is achieved mainly by putting the first stage input FET for the charge sensitive preamplifiers very close to the electrodes. This approach is made in order to investigate the theoretical resolution limit for the CdZnTe drift strip detectors.

3.7.1 Read-out electronic

For the analogue data processing, the standard NIM (Nuclear Instrument Module) system [5] was used for all the spectral measurements and the characteriza-

[5] This is a nuclear instrumentation standard commonly used for differential pulse hight spectrum from a radiation detector. NIM modules designed for the processing of linear pulses are signal compatible only if they share a common classification for the dynamic range of the signals. In this way the measurement result can be reproduced if consistent system is used again.

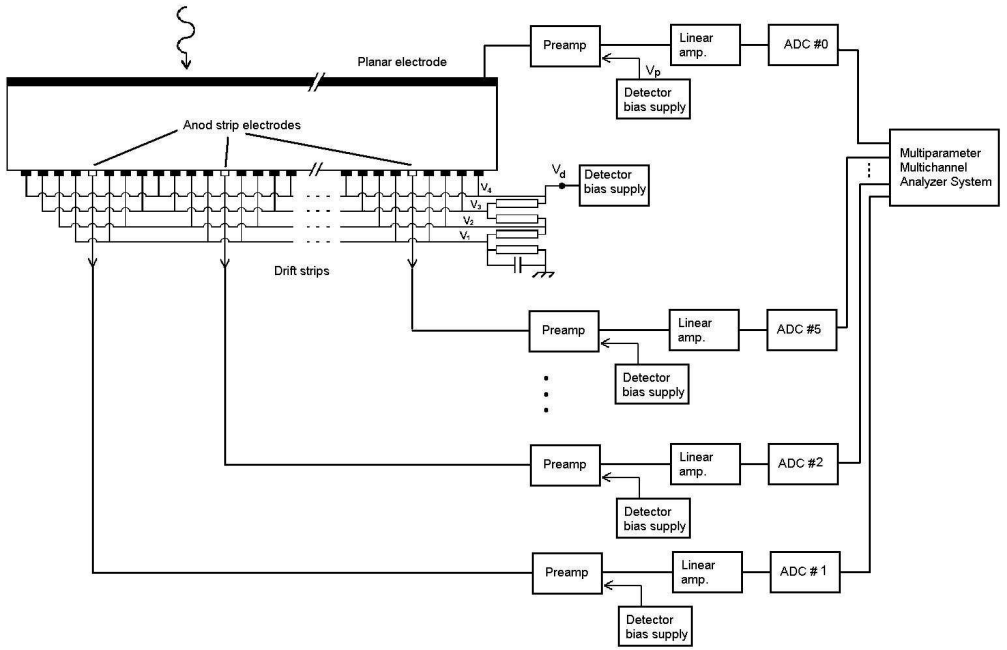

Figure 3.17 Set-up for the CdZnTe drift strip detectors using NIM (Nuclear Instrument Module) system. In this set-up, two ORTEC-142A preamplifiers and four eV-550 preamplifiers were used. An ORTEC-556 is used for the planar electrode bias. An ORTEC-456 is used for the drift strip biases. An ORTEC-459 is used as common bias supply for all the anode strip preamplifiers. ORTEC-572 linear amplifiers were used for all the preamplifiers output signal in order to shape the signals. All the amplified and shaped signals were than digitized with analogue to digital converters (ADC) and analyzed with multi parameter multi channel analyzer.

tion work. Two types of first stage charge sensitive preamplifier were used in this thesis. The first type was eV-5093 ultra low noise charge sensitive hybrid preamplifier in a eV-550 house. Fig. 3.17 shows the set-up for the CdZnTe drift strip detectors using a NIM system. In this set-up, two ORTEC-142A preamplifiers and four eV-550 preamplifiers were used. An ORTEC-556 is used for the planar electrode bias. An ORTEC-456 is used for the drift strip biases. An ORTEC-459 is used as common bias supply for all the anode strip preamplifiers. ORTEC-572 linear amplifiers were used for all the preamplifiers output signal in order to shape the signals. All the amplified and shaped signals were then digitized with analogue to digital converters (ADC) and analyzed with multi parameter multi channel analyzer (MPMCA).

Besides the standard charge sensitive preamplifiers from ORTEC and eV-products, a new front-end electronic containing 7 charge sensitive preamplifiers was designed and fabricated by BSI. This electronic box was named as BSI-electronic. Three considerable characteristic in this electronic box are: The field effect transistors (FET) for each charge sensitive preamplifiers were placed very close to the electrodes therefore pick-up noise and noise caused by the stray capacitance is minimized. A vacuum chamber was implemented in order to avoid problems connected with humidity and cooling. The detectors are mounted in side the vacuum chamber on a controllable peltier coolers which are capable of cooling the devices to $\sim -35^{o}C$. The signal from each detector

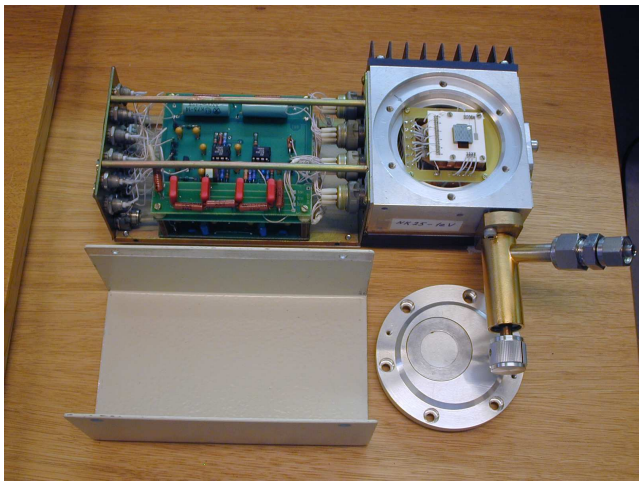

Figure 3.18 BSI-electronic box contains a vacuum chamber, a peltier cooling element, seven charge sensitive preamplifiers and a voltage divider.

is extracted from the electrodes by a preamplifier whose front end FET is also maintained at the detector temperature.

The rest of the analog chain consists of a NIM system (ORTEC 572 spectroscopy amplifier that shapes and amplifies the signal prior to digitization and the high voltage supplies). The signal amplitudes are digitized by a Canberra ADCs and processed and stored by a PC.

Fig. 3.18 shows a picture of the BSI-electronic with the GSFC-CZT-4 detector connected. The ceramic support for the detectors BSI-CZT-2 and GSFC-CZT-4 were specially designed for this BSI-electronic box. The GSFC-CZT-1 was the first detector designed and fabricated in this thesis and it has a different ceramic support therefore could not be installed in the BSI-electronic box.

3.7.2 Electronic noise

Electronic noise in semiconductor detectors is described in detail in the literature [1] [31] [32]. The electronic noise related to the preamplifier, is due to two main sources: (1) the *series thermal* noise generated in the channel of the input Field Effect Transistor (FET) of the preamplifier (2) the *parallel thermal* noise due to the detector leakage current (also referred to as *shot* noise). Expressions quantifying these noise components are listed below [33] [34], and the total noise is then a quadratic sum of the individual noise component. The *series thermal* noise from the input FET channel is given by:

$$ENC_s = \frac{e}{q} C_{in} \sqrt{\frac{kT}{2\tau} [\frac{0.7}{g_m}]} \tag{3.11}$$

The *parallel thermal* noise from the detector leakage current is given by:

$$ENC_p = \frac{e}{2} \sqrt{\frac{\tau I_d}{q}} \tag{3.12}$$

And the total noise becomes:

$$ENC_t = \sqrt{ENC_s^2 + ENC_p^2} \tag{3.13}$$

where ENC is in electrons rms, τ is the integration time of the shaping amplifier. I_d is the detector leakage current, g_m is the transconductance of the preamplifiers FET, k is Boltzmann's constant, q is the electronic charge, e is 2.718.., C_{in} is the input capacitance of the preamplifier (sum of the detector, gate and stray capacitance). The additional noise components (e.g., $1/f$ components and noise components associated with the feedback and the bias

resistors) are ignored due to their negligible noise contribution when compared with the thermal noise due to the detector leakage current [1].

The noise contribution of these individual noise sources (the *series thermal* noise and the *parallel thermal* noise) can be calculated by measuring the detector leakage current I_d, and the total input capacitance C_{in} of the preamplifier. Following is an example for the estimation of the two major detector noise contribution: The detector leakage current $I_d \simeq 3.0\ nA$ was measured for the GSFC-CZT-1 (anode strip 3) at temperature 22^oC. The detector was biased with Vp=-300V and Vd=-100V. The strip capacitance was calculated (using ELFI) for the GSFC-CZT-1 as ~ 1 pF. Adding a ~ 2 pF capacitance for the gate and the stray capacitance, C_{in} becomes ~ 3 pF. The FET transconductance $g_m = 0.5\ mS$ is found in [34] for similar FET used in eV-550 and this value is adopted in the calculations. The shaping time $\tau = 1\ \mu s$ was used in the calculations. The *series thermal* noise from the input FET channel is calculated as:

$$ENC_s \simeq 85 \quad e^- \quad rms \tag{3.14}$$

The *parallel thermal* noise from the detector leakage current is calculated as:

$$ENC_p \simeq 152 \quad e^- \quad rms \tag{3.15}$$

And the total noise:

$$ENC_t \simeq 174 \quad e^- \quad rms \tag{3.16}$$

This corresponds to a linewidth (FWHM) due to the total electronic noise (in keV) when $\omega = 4.64$ eV is the mean energy required for creation of an electron-hole pair :

$$FWHM_{elc} = 2.355 \cdot \omega \sqrt{ENC_p^2 + ENC_s^2} \simeq 1.9 \quad keV \tag{3.17}$$

The main electronic noise source of a CdZnTe drift strip detector system is the leakage current of the detector with ~ 1.7 keV FWHM.

The electronic noise for the NIM system with the eV-550 and the ORTEC-142A as the first stage preamplifiers was measured.

Fig. 3.19 shows a multi plot showing the ^{137}Cs spectra obtained by GSFC-CZT-1 detector. The total electronic noise for the system for each signal chain was measured using a test pulse generator and resulted peaks can be seen in the figure on the right side of the 661.6 keV lines. A typical electronic noise of 2.0 keV to 3.8 keV FWHM (at room temperature) was measured for the signal chains (detector was operated with Vp=-300V and Vd=-100V and $1\mu s$ shaping time). All the spectra obtained by the anode strips were corrected. The corrections were performed using the method explained by Eq. (3.2). The data from test pulse generator was added after the correction process. The

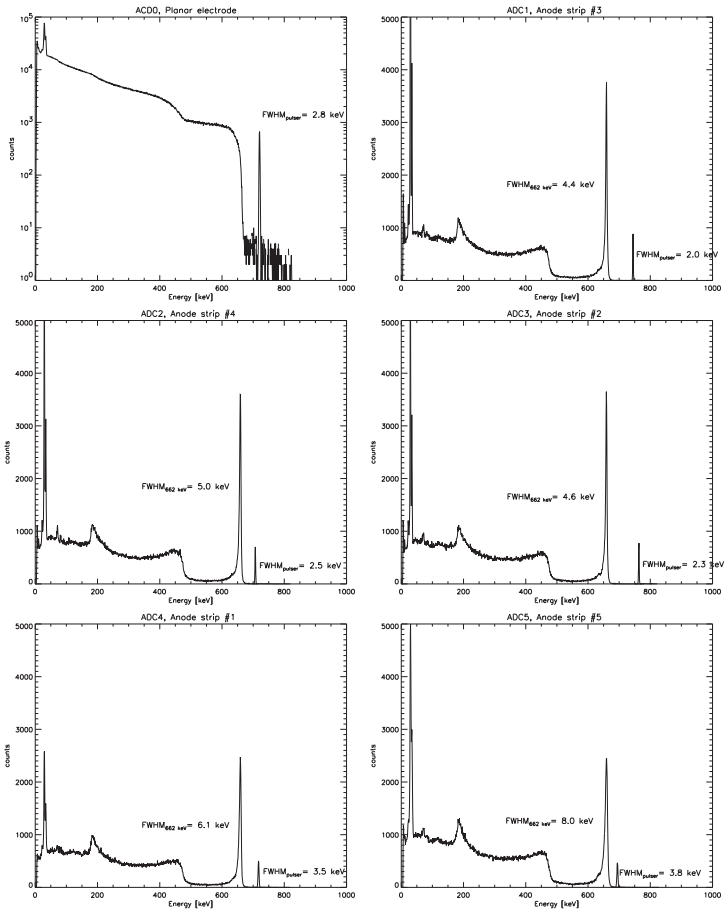

Figure 3.19 The spectral resolution and the total electronic noise were measured for GSFC-CZT-1 using the set-up shown in Fig. 3.17. For the anode strip 1 (connected to ADC 4) and 5 (connected to ADC 5), ORTEC-142A preamplifiers were used. The total electronic noise was measured slightly higher for these preamplifiers compared to the eV-550 preamplifiers. All spectra are energy calibrated and corrected except the data from the test pulse generator. Typical electronic noise for the ev-550 preamplifiers was 2.0 to 2.8 keV and for the ORTEC-142A preamplifiers, the noise was 3.5 to 3.8 keV at temperature 22^oC. The detector was operated with Vp=-300V and Vd=-100V and $1\mu s$ shaping time. For the energy calibration, the detector was illuminated with a ^{137}Cs source. The spectra from all anode strips in coincident with the planar electrode were recorded.

anode strip 3 (ADC1) resulted in the best spectra with a total electronic noise of 2.0 keV FWHM. This is close to the calculated total electronic noise given in Eq. (3.17).

3.7.3 Variation of the carrier's drift path length

In order to illustrate the variation of the charge carriers' drift path length as a function of the operation voltage with the experimental data, ^{241}Am scans were conducted on the GSFC-CZT-1. A beam was collimated from a ^{241}Am source with a slit of 0.5 mm wide and 10 mm long. The collimated ^{241}Am source was placed on a 2D XY-table and the beam aligned parallel to the strips. A length of a 12 mm was scanned by stepping the beam in the direction perpendicular to the strips by the XY-table. The step was 200 μm. The detector box was aligned so that the detector crystal was placed in the center of the scan area with a $\approx$ 1 mm distance from the sides. Signals from all 6 electrodes (5 anode strips electrodes and 1 planar electrode) were amplified, shaped and digitized. The set-up used for this scan can be seen in Fig. 3.17. A real time data acquisition and a data recording program (also works as a controller program for the XY-table) are developed using the LabView [6] (LABoratory Virtual Instrument Engineering Workbench)package. Scans were completed using two different sets of detector bias voltages, (Vp,Vd) = (-300V,-100V) and (Vp,Vd) = (-150V,-100V) in order to show the effect of dead-zone to detector performance. The operating temperature was 22 ^oC. The shaping time was 1μs for all the shaping amplifiers.

Fig. 3.20 shows the scan result for the bias voltages, (Vp,Vd) = (-300V,-100V). Fig. 3.20a) shows the variation in the total counts as a function of the beam position for the planar electrode and all the anode strips. For the anode strips, the total counts drop between two adjunct drift detector cells. This drop corresponds to the dead-zone within the detector and dependent on the operation voltages (Vp,Vd). In this area, the electrons were being collected by other than the anode strip electrode. For the interactions in the dead-zone, the electron-induced charge was induced only on the electron collecting drift strip and on the planar electrode. Fig. 3.20b) shows the variation of the photo peak position channels (60 kev) due to the nature of the drift strip bias voltages, which resulted in variation of the electric field across the drift strips. Therefore, the mean drift length of the electrons can vary and the signal can fluctuate in the dead-zone area for the planar electrode. The photo peak position variation in plot b) was correlated with the dead-zone area between two adjunct drift detector cells. Fig. 3.20c) shows the variation of the FWHM of the photo peak (60 kev). The variation was due to the fluctuation of the mean drift length of

[6] © National Instruments

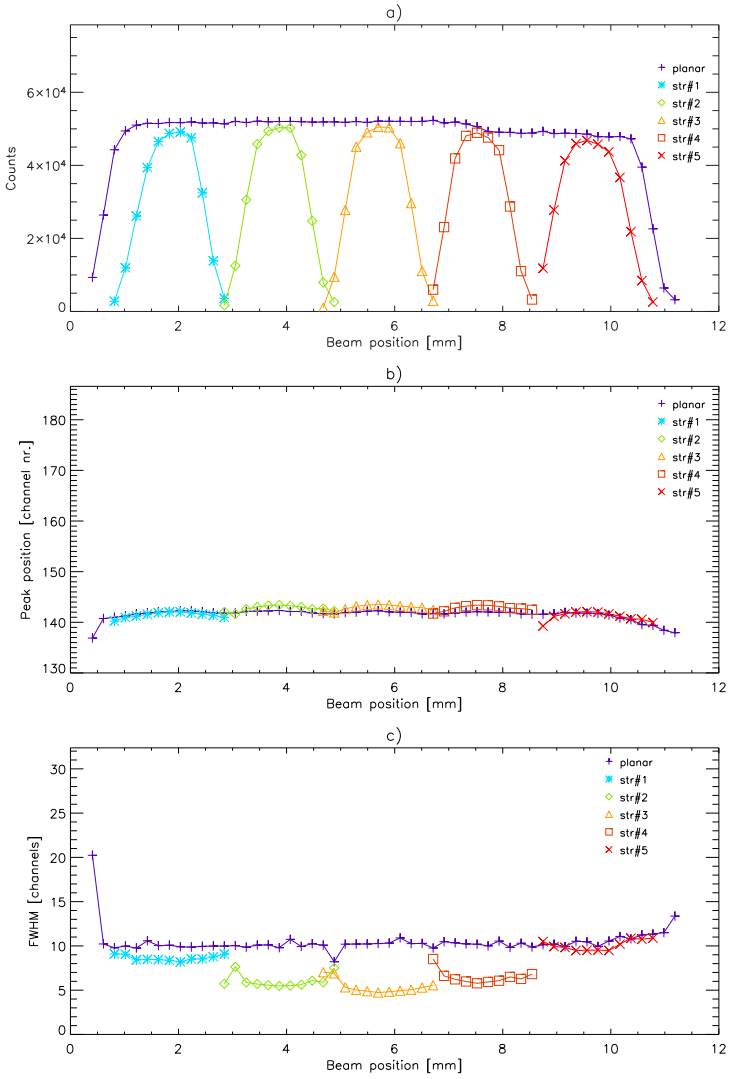

Figure 3.20 ^{241}Am scan. The detector bias voltages are (Vp,Vd) = (-300V,-100V). The operating temperature is 22 ^{o}C. The shaping time is 1μs for all the shaping amplifiers. a) the plot shows the total counts recorded by all 6 electrodes (5 anode strips electrodes and 1 planar electrode) for each beam position. b) the plot shows the mean peak channel for 60 keV line from the ^{241}Am source. c) the plot shows the FWHM at 60 keV (in channels).

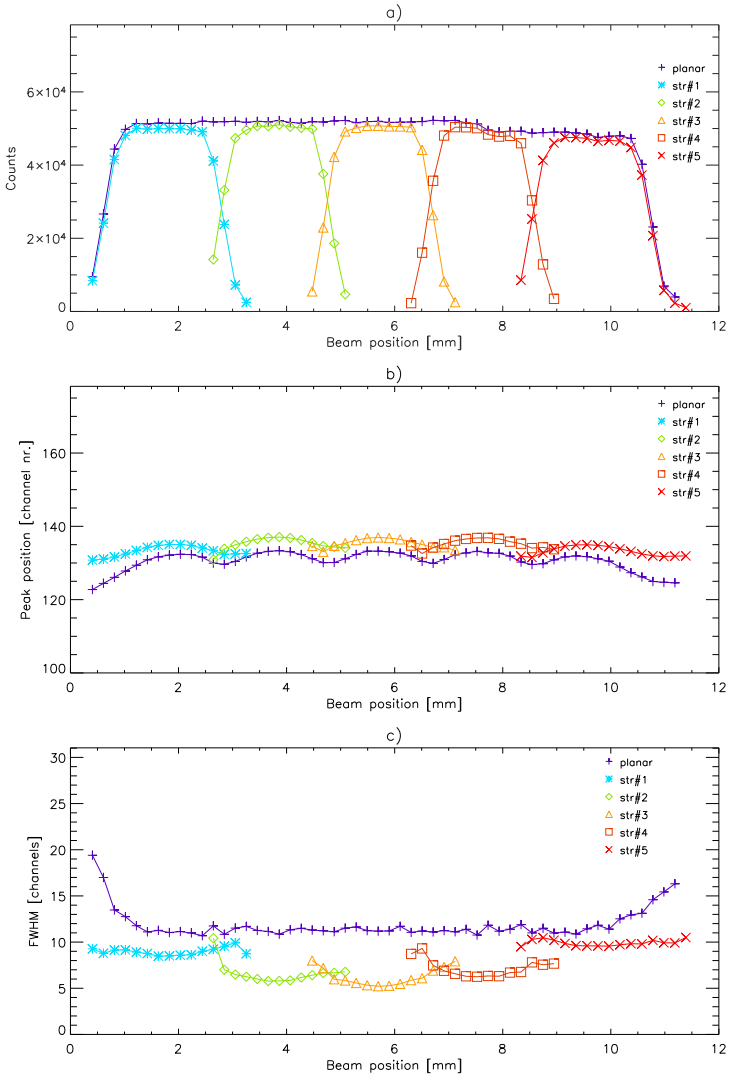

Figure 3.21 ^{241}Am scan. The detector bias voltages were (Vp,Vd)=(-150V,-100V). The operating temperature was 22 ^{o}C. The shaping time was 1μs for all the shaping amplifiers. a) the plot shows the total counts recorded by all 6 electrodes (5 anode strips electrodes and 1 planar electrode) for each beam position. b) the plot shows the mean peak channel for 60 keV line from the ^{241}Am source. c) the plot shows the FWHM at 60 keV (in channels).

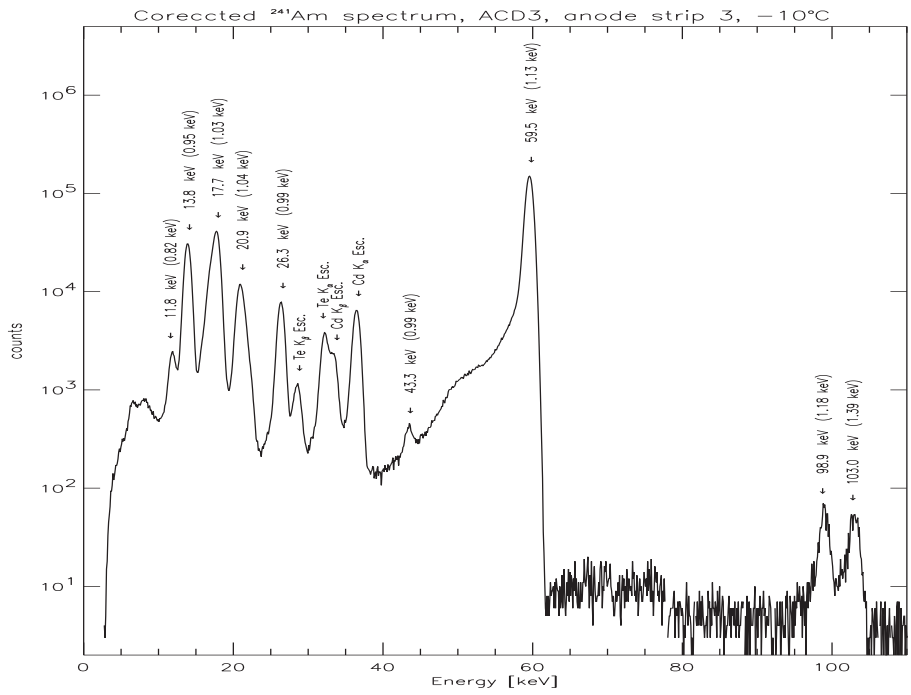

Figure 3.22 ^{241}Am spectrum was measured by the GSFC-CZT-4 using the read-out box shown in Fig. 3.18. The spectra were recorded from the anode strip 3 and the planar electrode in coincident. The spectrum from the anode strip 3 is energy calibrated and corrected. Total electronic noise was 0.8 keV FWHM for the anode strip number 3. The operation temperature was -10^oC. The operation voltages were Vp=-300V and Vp=-120V.

the electrons and the best resolutions were obtained at the center of the drift detector cells.

Fig. 3.21 shows the scan results completed using detector bias voltages, (Vp,Vd) = (-150V,-100V) in comparison to the scan with the detector bias voltages (Vp,Vd) = (-300V,-100V). Fig. 3.21a) shows that the dead-zone is now reduced compared to the detector bias voltages (Vp,Vd) = (-300V,-100V). The change of the dead-zone by changing the bias condition is illustrated in Fig. 3.5 as well. Fig. 3.21b) shows the variation of the photo peak position channels (60 kev) and it is more pronounced due to the reduced electric field across the drift strips. Fig. 3.21c) shows the variation of the FWHM of the photo peak (60 kev) and the variation across the detector cell is more pronounced due to

the change in the mean drift length of the electrons.

3.7.4 Spectral response

In order to investigate the spectral response of the detectors, energy resolution using ^{241}Am, ^{109}Cd, ^{133}Ba and ^{137}Cs calibration sources were measured for the GSFC-CZT-1 and GSFC-CZT-4. The BSI-CZT-2 showed a non-uniform spectral response and was suspected to suffer spectral performance degradation caused by the grain boundaries. Therefore, the BSI-CZT-2 was only investigated in connection with the material uniformity. The spectral response of the GSFC-CZT-1 and GSFC-CZT-4 has shown uniform behavior. The $\mu\tau_e$ for the GSFC-CZT-1 and the GSFC-CZT-4 were measured as 5×10^{-3} cm^2/V and

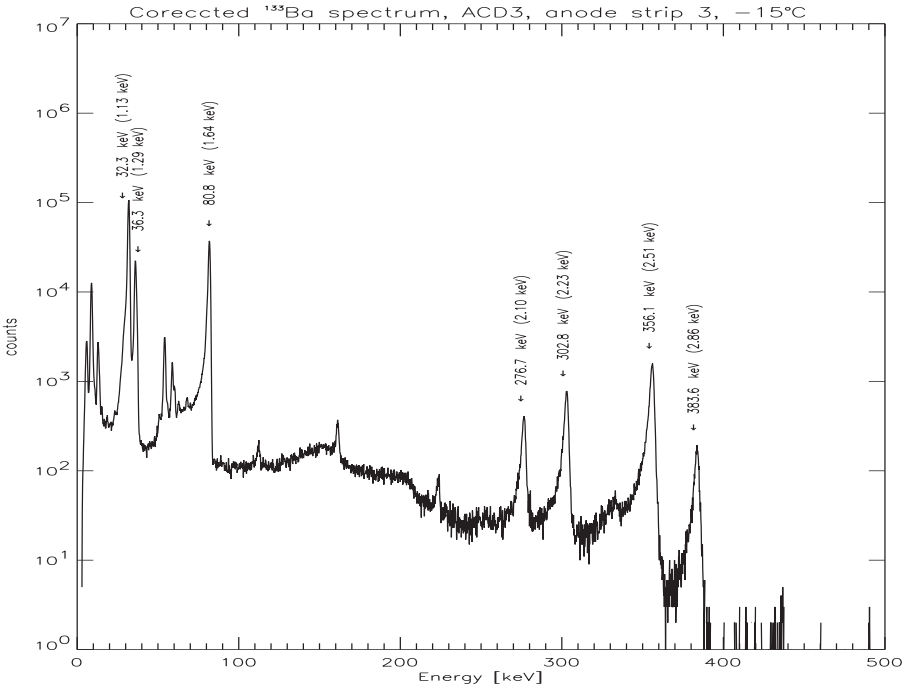

Figure 3.23 ^{133}Ba spectrum was measured by the GSFC-CZT-4 using the read-out box shown in Fig. 3.18. The spectra were recorded from the anode strip 3 and the planar electrode in coincident. The spectrum is energy calibrated and corrected. Total electronic noise was 0.8 keV FWHM for the anode strip number 3. The operation temperature was -15^oC. The operation voltages were Vp=-300V and Vp=-120V.

$8 \times 10^{-3}\ cm^2/V$, respectively. The best results, in terms of energy resolution, were obtained from these detectors. All measurements have shown that the resolution was limited by the total electronic noise below 100 keV.

The aim of the spectral measurements was to find out the detectors' spectral response to wide energy range and to determine the intrinsic energy resolution as a function of the photon energy. For the best spectral response, the GSFC-CZT-4 was characterized using the NIM system with the BSI-electronic box as the first stage preamplifiers (only the GSFC-CZT-4 could fit in the BSI-electronic box). Energy resolution of the GSFC-CZT-4, using ^{241}Am, ^{109}Cd, ^{133}Ba and ^{137}Cs calibration sources was measured at temperature -10^oC. The measurements were carried out under uniform illumination with calibration sources. The operation voltages were Vp=-300V and Vp=-120V. Only the spectra recorded by the center drift detector cell of the GSFC-CZT-4 is shown in Fig. 3.22, Fig. 3.23, Fig. 3.24 and Fig. 3.25. The total electronic noise at the anode strip readout was measured as 0.8 keV FWHM at -10^oC using a pulse generator. All these spectra are corrected as described in section 3.3.

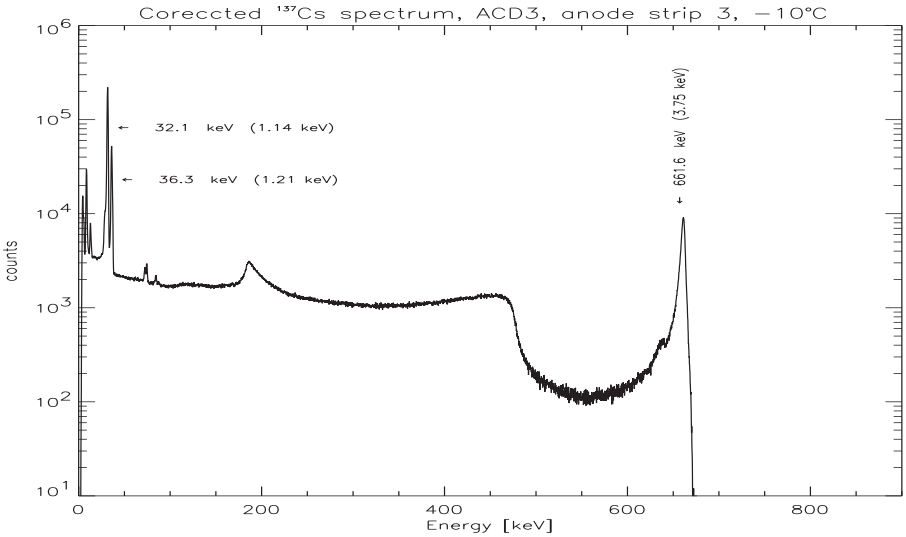

Figure 3.24 ^{137}Cs spectrum was measured by the GSFC-CZT-4 using the read-out box shown in Fig. 3.18. The spectra were recorded from the anode strip 3 and the planar electrode in coincident. The spectrum is energy calibrated and corrected. Total electronic noise was 0.8 keV FWHM for the anode strip number 3. The operation temperature was -10^oC. The operation voltages were Vp=-300V and Vp=-120V.

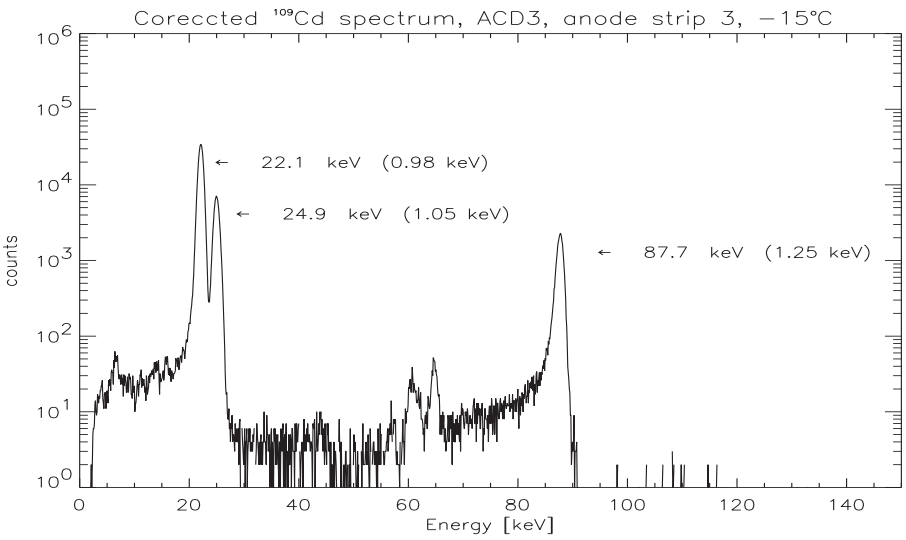

Figure 3.25 ^{109}Cd spectrum was measured by the GSFC-CZT-4 using the read-out box shown in Fig. 3.18. The spectra were recorded from the anode strip 3 and the planar electrode in coincident. The spectrum is energy calibrated and corrected. Total electronic noise was 0.8 keV FWHM for the anode strip number 3. The operation temperature was -15^oC. The operation voltages were Vp=-300V and Vp=-120V.

The corrected spectra contains all events ($\sim 75\%$) with ratio R values between 0.25 and 1.0. In these spectra all lines from the sources are detected. Some of the lines are identified and energies with corresponding resolution are included in the spectra. The energy resolution function of the detector was determined from these spectra. The intrinsic energy resolution as a function of photon energy is shown in Fig. 3.26 for the GSFC-CZT-4 detector. The energy resolutions shown here have been corrected for the electronic noise which is 0.8 keV. The solid line indicates the statistical limit from the Fano noise using Fano factor of F=0.1. The result shows that DSM can achieve energy resolutions which are within a factor of 2 of the Fano-limited resolution for the CdZnTe material.

3.7.5 Discussion and conclusions

The GSFC-CZT-4 yields some of the best performance figures yet reported for full illumination. For example, at 356 keV the FWHM energy resolution was 2.87 keV at detector temperature of -15^oC. At 60 keV, the corresponding

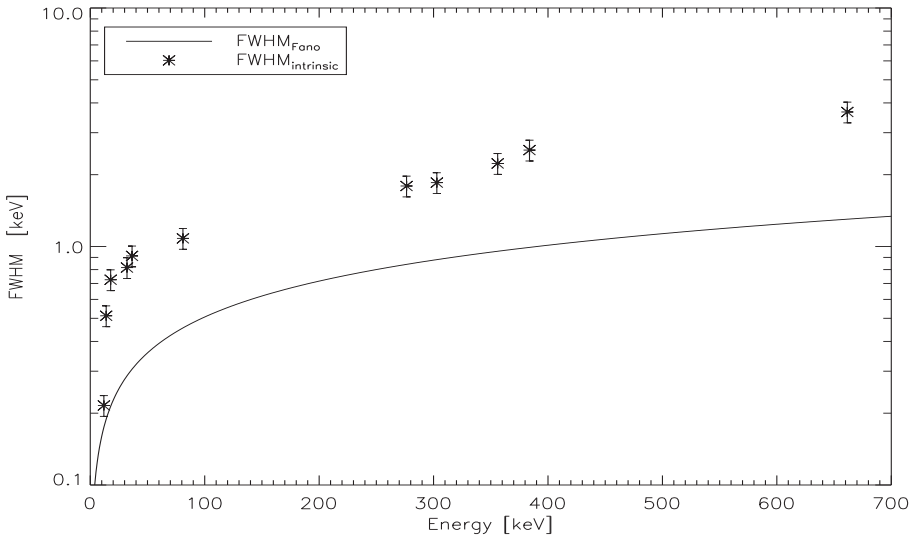

Figure 3.26 The intrinsic energy resolution as a function of photon energy, for the GSFC-CZT-4 detector. The energy resolutions shown here have been corrected for the electronic noise which is 0.8 keV. Data points are presented for one anode strip (anode strip number 3) of the GSFC-CZT-4 detector. The solid line indicates the statistical limit from Fano noise. The detector operation temperature was -15^oC for the ^{109}Cd and ^{133}Ba spectra, and -10^oC for the ^{241}Am and ^{137}Cs spectra.

resolution was 1.1 keV at detector temperature of -10^oC. These should be compared to the calculated Fano resolution 500 eV at 60 keV. At lower energies, the measured resolution is dominated by the noise component due to the detector leakage current. However, at medium and high energies, Fano noise becomes an appreciably fraction of the resolution function. The present results suggest that DSM can achieve energy resolutions which are within a factor of 2 of the Fano-limited resolution for the CdZnTe material.

4

Radiation damage effect in CdZnTe drift strip detectors

For a long-term space operation of an instrument based on CdZnTe detectors it is important to know the influence of the particle induced radiation damage on the detector performance. During a space mission a detector will be exposed to energetic particle radiation fluences up to $2 \times 10^9 p^+/cm^2$ *per year. A low-earth orbit with moderate inclination is assumed.*

4.1 Introduction

Although the spectroscopic properties of the CdZnTe strip detectors are almost independent of the hole collection efficiencies ($\mu\tau_h$) of the detector materials, they are of course very dependent on the electron collection efficiencies. Especially materials with fluctuating electron mean drift length λ_e will result in degraded detector performance. A serious concern for space use of the CdZnTe strip detectors is therefore, the particle induced radiation damage that is known to influence the electron collection efficiency. DSRI in collaboration with DTU and the cyclotron facility at Copenhagen University Hospital have initiated a study of radiation effects by exposing a CdZnTe strip detector to proton fluences of up to $60 \times 10^8 p^+/cm^2$ with energy of 30 MeV. Even for such high dose loads, which had a dramatic effect on the spectroscopic performance of

the detector, the detector was able to recover after an appropriate annealing procedure. The CdZnTe drift strip detector offers interesting new information on radiation damage since it can be studied as function of the depth inside the detector material.

This chapter focuses on ground-based testing of the CdZnTe drift strip detector and the subsequent predictions of the detector performance degradation as a function of proton fluence.

4.2 Radiation damage

The following section is based on books by G. Messenger [35] and G. Lutz [7] and deals with general radiation damage effects in semiconductors. The theory of the radiation damage explained in these books are also valid for the CdZnTe semiconductor detector material.

The radiations of interest, in the study of the radiation damage effect in the detector materials, are energetic particles (i.e., electrons, protons, neutrons or ions). The origin of these particles may be particle accelerators, the natural space radiation environment, nuclear reactions, or secondary mechanisms such as Compton electrons produced by gamma rays. Because they have mass, energy and possibly charge, these particles or other particles generated by them can interact in several ways with materials. In general, the dominant interactions are:

- **Inelastic collisions with atomic electrons:** Inelastic collisions with bound atomic electrons are usually the predominant mechanism by which an energetic charged particle loses kinetic energy in an absorber. In such collisions, electrons experience a transition to an excited state (excitation) or to an unbound state (ionization).

- **Elastic collisions with atomic nuclei:** Energetic charged particles may have coulombic reactions with the positive charge of the atomic nucleus through Rutherford scattering. In some cases the amount of energy transferred to the atom will displace it from its position in a crystalline lattice. Energetic particles may also interact directly by a hard sphere collision with the nucleus. If sufficient energy is transferred to displace an atom from its lattice site, that atom may be energetic enough to displace other atoms.

- **Inelastic collisions with atomic nuclei:** This general category of interactions includes several processes which are important in radiation damage studies. High energy protons undergo inelastic collisions with the atomic nucleus. In this process, the energetic proton interacts with the

nucleus and leaves it in an excited or activated state. The excited nucleus emits energetic nucleons and the recoiling nucleus is displaced from its lattice site. This process is also referred to as spallation. The recoiling nucleus in turn cause more displacements. Absorption of thermal (slow) neutrons followed by a nuclear reaction by nuclei can also be included in this group.

4.2.1 Radiation damage mechanism

The major type of radiation damage mechanisms in the CdZnTe detector material are the ionization damage and the atomic displacement. In general, semiconductor devices are affected by two basic radiation damage mechanism:

- **Displacement damage:** Displacement damage effects occur in bulk semiconductor materials because of scattering interactions of heavy particles, such as protons and neutrons, with the atoms of the semiconductor lattice. In the initial scattering event, the bombarding particle displaces an atom from its lattice site, and this "primary knock-on" may produce an additional cascade of displacements, the magnitude of which depends on the amount of kinetic energy transferred to the primary knock-on by the proton or neutron. The resulting defects alter the electronic characteristics of the semiconductor crystal. Displacement damage depends on energy and momentum transfer to lattice atoms, which depends on the mass and energy of the incident radiation.

- **Ionization damage:** The energy, absorbed in semiconductor crystal liberates charge carriers leading to unintended concentrations of charge and, as a consequence, parasitic fields. Ionization effects depend primarily on the absorbed energy, independent of the type of radiation. In general, the ionization is the dominant absorption mechanism so that ionization damage can be measured in terms of energy absorption per unit volume, usually expressed in rad or gray (1 rad= 100 erg/g, 1 Gy= 1 J/kg= 100 rad). Since the charge liberated by a given dose depends on the absorber material, the ionizing dose must be referred to a specific absorber.

It is important to emphasize that this thesis does not deal with microscopic effects of particle induced damage in semiconductors, e.g., the vacancy type or the deep trap levels in the forbidden gap. However, the thesis investigates the macroscopic effects of particle induced radiation damage on the measurable material properties e.g., the change of the electron trapping and the leakage current. These are related to the detector performance.

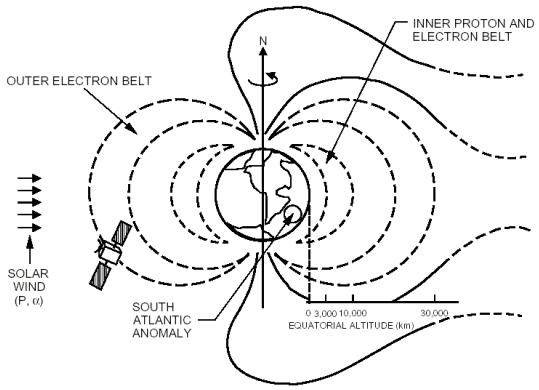

Figure 4.1 Schematic diagram of the Earth's Van Allen radiation belts formed by the Earth's magnetosphere [36].

4.3 The space radiation environment

Space missions could last as long as 10 years from launch to end-of-mission. During this time, the detector material will be exposed to radiation in the form of energetic particles. The total dose depends on a number of factors, including mission duration, path in space, solar activity, shielding, and the radiation environment during the mission.

The space environment is detrimental to materials functioning in space. A material's life in a specific environment is best determined by real-time exposure in that environment. In practice, long lasting missions reduce the practicality of real-time exposure testing and will have to rely on accelerated ground-based exposure testing and modelling to generate material life predictions.

The space radiation environment near Earth consists of the following types of radiation:

- radiation belts
- solar wind
- galactic cosmic rays (GCR)

For the low altitude orbits, the primary sources of radiation are electrons and protons trapped by the Earth's magnetosphere, as shown in the highly simplified diagram in Fig. 4.1. This region is known as the Van Allen belts

(discovered in 1958 by Explorer 1 space mission). The Van Allen radiation is usually responsible for most of the ionizing dose damage to electronics and materials. The trapped particles in the Earth's magnetic field are constantly in motion. Their motions in the field consist of a gyration about field lines, a bouncing motion between the magnetic mirrors found near the Earth's poles, and a drift motion around the magnetic field lines [11]. The Van Allen belts is significant between the altitudes of approximately 1000 km and 32,000 km. The particle fluence rate levels drop rapidly outside this altitude range. The altitude distributions of electrons and protons are significantly different.

The solar wind consists of electrons, protons and a small percentage of heavier ions. The energy and the fluence of these particles are strongly dependent on the solar conditions. Solar particle events (flares), which can produce high intensity proton and heavy ion fluence rates lasting from hours to several days, are significant for the total dose. The August 1972 event produced a peak fluence rate in excess of $10^6 p^+/cm^2/sec$ above 10 MeV energy [37]. Such events are unpredictable in their time of occurrence, magnitude, duration or composition. The earth's magnetic field shields a region of near-earth space from these particles (geomagnetic shielding), but they easily reach polar regions and high altitudes such as the geostationary orbit. The galactic cosmic rays (GCR), consisting of about 85% protons, approximately 14% alpha particles, and about 1% heavy nuclei [38]. These particles originate outside the solar system and are believed to be distributed uniformly throughout the galaxy. GCR can be very energetic, reaching energies as high as 10 GeV/nucleon. While ions as heavy as uranium have been observed, the incidence of ions with atomic numbers greater than iron is rare. The heavier ions like Fe are present in much smaller densities. However, because the heavy ions deposit so much energy as they pass through a semiconductor device circuit, they can be more damaging overall even though they are much rarer in occurrence.

When high-energy radiation passes through a material such as a radiation shield, nuclear interactions occur with nuclei of the material resulting in the emission of secondary radiation in the form of a continuous energy spectrum of energetic photons (Bremsstrahlung), gamma rays, electrons, alpha particles, and neutrons. These secondary particles can also cause damage to materials in the same manner as the primary radiation. Thus, in determining the total radiation flux that reaches the detector material, secondary radiation must be taken into account, especially if thick, high atomic number materials are present. For the radiation damage test explained in this chapter, the CdZnTe material was directly exposed with 30 MeV protons. Therefore, secondary particle effects from the surrounding material of the CdZnTe is ignored.

4.4 Findings in the literature

The radiation damage studies on the CdZnTe material have been carried out by several independent researchers using different radiation sources, producing charged particles and neutrons over a wide energy range. Up to now, few experimental data are available on the response of CdZnTe detectors (e.g., Wong *et al.* [39], Varnell *et al.* [40]). A brief review is given by Franks *et al.* [41] for the radiation damage measurements in room-temperature semiconductor radiation detectors. For the CdZnTe material, these studies conclude that significant changes in detector performance, due to radiation damage, can occur for prompt doses corresponding to 200 MeV proton fluences ranging from $5 \times 10^8 p^+/cm^2$ and $50 \times 10^8 p^+/cm^2$. Detector response changes following high-energy proton irradiation are consistent with increased electron trapping and the associated decreases in the $\mu\tau_e$. A worst case degradation by a factor of 4.4 in $\mu\tau_e$ is reported by Wong *et al.* [39] for proton dose ranging from 0 to $50 \times 10^8 p^+/cm^2$. This effect may be partially corrected in drift strip detectors, which is designed to compensate for electron trapping. It has also been reported in the above-mentioned articles that the performance of the CdZnTe detector can be recovered by annealing at room temperature or elevated temperatures.

4.5 Computer software calculation of damage using TRIM

Calculations using the computer-code Stopping and Range of Ions in Matter (SRIM) [42] show that the lateral straggling as a result of stopping of 30 MeV protons (H^+) in 3.0 mm thick CdZnTe is about 240 μm, and longitudinal straggling is about 150 μm. The stopping range of 30 MeV protons is about 2.95 mm in the CdZnTe. The calculation results can be seen in Appendix. C section C.2. The TRIM Monte Carlo calculations [42] show that the creation of damage mainly occurs near the end of the ion tracks, at a depth of 2.95 mm. This shows that the damage is confined to a small volume at a certain depth. In this work, the lateral damage distribution is not determined by the beam-spot size. The beam is scanned with a zigzag path in order to get a homogenous proton fluence throughout the detector area thus, uniform lateral damage profile within the detector. The TRIM calculations also show that the ionization takes place along the full ion track with a maximum at a depth of about 2.95 mm.

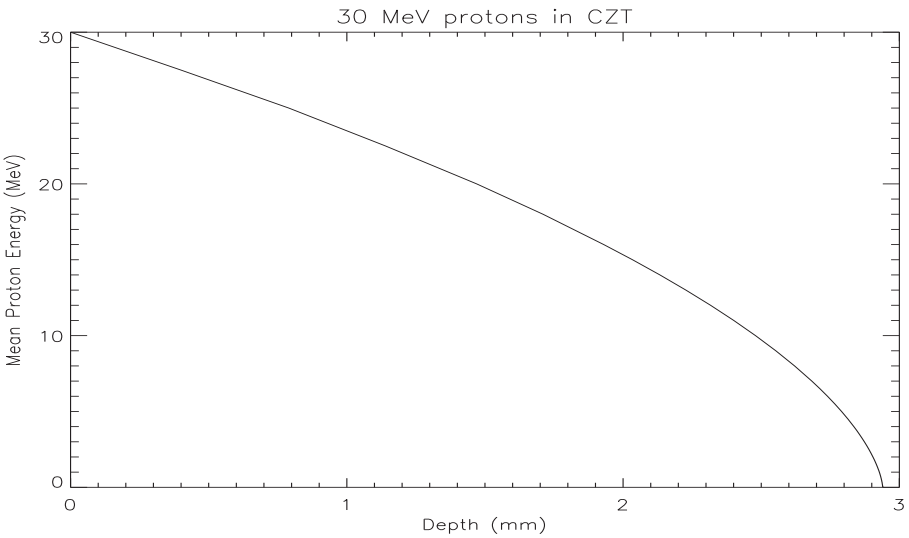

Figure 4.2 Calculated mean proton energies in CdZnTe material having a thickness of 3.0 mm and a density of 5.8 g/cm^3. The proton energy is 30 MeV.

4.6 Experimental

4.6.1 Set-up

Great effort and time were used for developing software and an XY-table to ensure correct fluences for the detector. A mechanical chopper were developed in order to achieve suitable beam currents. The XY-table moved the detector in a zigzag path in order to ensure a uniform irradiation. A Faraday Cup (FC) was attached to the system in order to measure the beam intensity and the beam profile just before the irradiation procces. The beam parameters from the beam profile were used to calculate the proton fluence given to the detector. The beam was moved with constant speed in a zigzag path thus, the area of 40x40 mm2 was covered during the irradiation process. The detector was placed in the center of the rectangle area with the planar electrode facing the beam. The irradiation of the detector lasted typically 40 s. All electrodes of the detector were held at ground potential during the irradiation process. The detector was irradiated in several steps to the proton fluences given in tab. 4.1. Immediately after each irradiation the gamma activity of the detector was measured for 10 min with a Ge detector situated at the Cyclotron facility.

Then the detector was quickly moved back to the detector lab at DSRI, where it was biased and the detector itself was used to record the produced activity in the CdZnTe material (delay of 30 min). These measurements lasted typically a few days. The $\mu\tau_e$ was then determined from the detector pulse height response measurements using ^{137}Cs and ^{109}Cd radiation sources. Pulse height spectra were recorded for a set of bias voltages: (Vp,Vd) = (-350V,-117V), (-300V,-100V), (-250V,-85V), (-200V,-66V), (-150V,-50V). The detector was then scanned (2D) with an 400 μm ^{241}Am X-ray beam in order to determine the uniformity. Finally, the bulk and surface leakage current of the CdZnTe detector material were measured.

For the analogue data processing, the standard NIM system with two ORTEC-142A preamplifiers and four eV-550 preamplifiers were used. An ORTEC-556 is used for the planar electrode bias. An ORTEC-456 is used for the drift strip biases. An ORTEC-459 is used as common bias supply for all the anode strip preamplifiers. ORTEC-572 linear amplifiers were used for all the preamplifiers output signal in order to shape the signals. All the amplified and shaped signals were then digitized with analogue to digital converters (ADC) and analyzed with multi parameter multi channel analyzer (MPMCA). More detail information is given in section 3.7.1.

4.6.2 The detector

The selected detector (GSFC-CZT-1), which was to be irradiated with protons, was a spectroscopic grade material with a size of $10 \times 10 \times 2.7$ mm^3 from eV-products and it consisted of a planar electrode on one side and strips on the other. The strip contacts were deposited on one side of the detector with great success in terms of achieving high surface resistivity at Goddard Space Flight Center with their own developed method. Detailed information concerning the fabrication of the CdZnTe strip detectors can be found in [23]. The detector electrode geometry is as follows: The strip pitch is 200 μm with a 100 μm strip width and consists of a double layer of Pt/Au. The planar electrode (cathode) is Pt 10×10 mm^2. Total number of strips are configured as drift detectors with a group of 9 strips. Each drift detector cell consists of 8 drift strip electrodes and one anode readout strip. The GSFC-CZT-1 detector has five independent drift detector cells. The readout strips are held at ground potential and the drift strips are negatively biased by a voltage divider providing: Vi=Vd*(i/4). The common planar electrode, through which the detector is irradiated, is biased negatively at Vp.

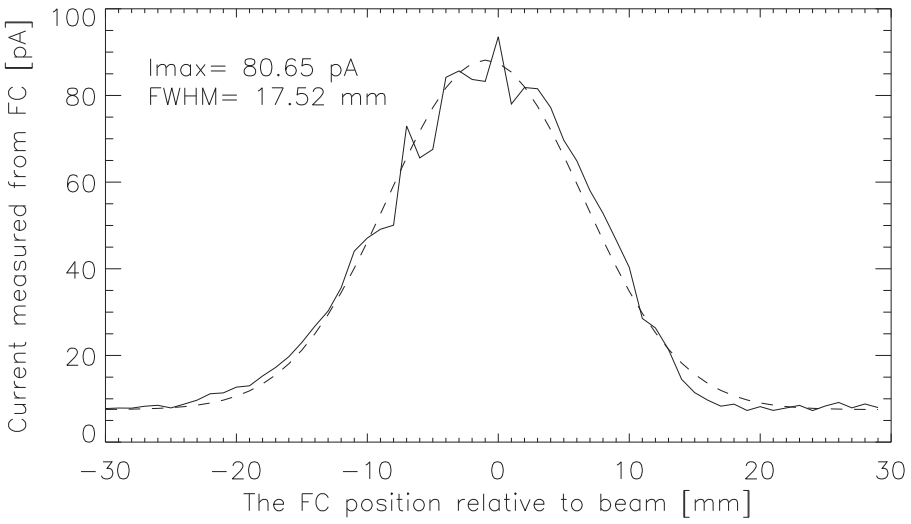

Figure 4.3 Current to the Faraday Cup when passing trough a proton beam from the cyclotron at the Copenhagen University Hospital.

4.6.3 The proton beam

A series of proton beam irradiation measurements have been carried out on a CdZnTe drift strip detector (the GSFC-CZT-1 detector) to study the effect of the proton damage. The proton irradiation reported in this thesis was performed at the cyclotron facility at the Copenhagen University Hospital using a Scanditronic MC32-NI cyclotron. The exit beam energy of the cyclotron was calibrated to be 31.3 ± 0.5 MeV. The beam energy was attenuated by a 25 μm Havar window ($\sim$ 0.4 MeV), 50 cm air ($\sim$ 0.8 MeV), and then by a 100 μm Al ($\sim$ 0.4 MeV) foil in front of the detector. Thus, the detector itself was irradiated with protons of 29.7 ± 0.7 MeV. The energy uncertainty is unfortunate because the range of protons, in the CdZnTe at this energy, is quite close to the thickness of the detector. Although, the test set-up and the dedicated software are specific to the purpose of the proton irradiation of the CdZnTe drift strip detector, they can be used to irradiate other materials as well.

Fig. 4.3 shows a measurement of the proton beam profile (current distribution) from the cyclotron at the Copenhagen University Hospital. The proton beam current was measured with a Faraday Cup (FC) during the passage of the proton beam. The FC was placed on an XY-table. The beam was in the

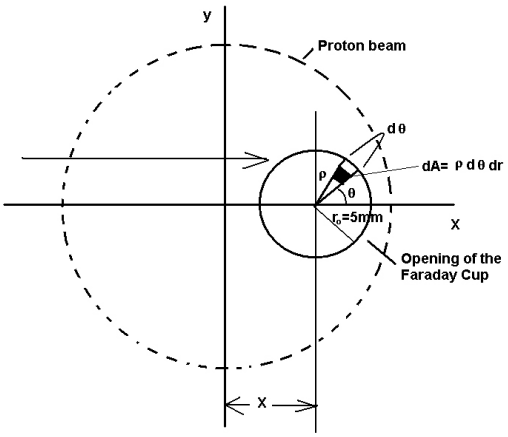

Figure 4.4 The Faraday Cup is moving trough the proton beam with constant velocity at y=0.

z-axis direction, i.e., horizontal and perpendicular to the XY-table. The aperture of the FC is circular with a diameter equal to 10 mm. The measurement was done after a number of beam scan in x- and y-direction using the software developed for the irradiation experiments. The software and the hardware are explained in detail in Appendix B. The FC current distribution in Fig. 4.3 is almost symmetric and with a good approximation it could be described by a Gaussian (peak) curve. The current I(x) to the FC is approximated by a Gaussian (peak) curve as follows:

$$I(x) = I_0 \cdot \exp(-x^2/(2 \cdot s^2)) \tag{4.1}$$

where I_0 is the current when the FC is placed at the beam center. x is the position of the (center of the) FC opening. s is a width parameter related to Full Width at Half Maximum (FWHM) as:

$$FWHM = s \cdot 2.3548 \tag{4.2}$$

The current distribution I(x) is not proportional to the proton fluence rate $\phi(r) \quad [p^+/(cm^2 \cdot s)]$ because a large (10 mm diameter) FC opening is "folded" with the proton fluence rate to give the current. In order to determine the fluence rate distribution, the current distribution should be "unfolded".

The beam shape was reported not smooth and not symmetrical in [43] and therefore, not well approximated by Gaussian curve[1]. However, for determina-

[1]According to the author, this is based on a set of measurements of the proton beam

tion of approximate values of proton fluence the Gaussian approximation may suffice. Assuming that the beam fluence rate distribution could be approximated by a Gaussian function then the fluence rate $\phi(r)$ as a function of radius r (the distance from the beam center), therefore, could be described as:

$$\phi(r) = \phi_0 \cdot \exp(-r^2/(2 \cdot z^2)) \tag{4.3}$$

In order to calculate the proton fluence, the beam width parameter z must be "unfolded" for the fluence rate distribution. The beam current I(x) is a folding of $\phi(r)$ with the FC. Therefore $z < s$. From the measured current distribution, the beam current width parameter s can be extracted using Eq. (4.1). The diameter of the FC opening[2] was 10 mm. The relation between the measured beam current distribution and the fluence rate distribution can be simplified by two width parameters, a beam current width parameter s and a beam width parameter z. The relationship between s and z can be solved numerically as follows: Fig. 4.4 shows an illustration of the moving FC with a diameter of 10 mm across the proton beam with constant velocity at y=0 (i.e., the center of the beam is passed). The flow of protons to a small area $dA = \rho d\theta dr$ is given by:

$$\triangle F = \phi_0 \cdot \exp(\frac{-(x + \rho\cos\theta)^2 - (\rho\sin\theta)^2}{2z^2})\rho d\theta dr \tag{4.4}$$

The total flow of proton to FC is given by:

$$F = \int\int dF = \int_{\theta=0}^{\theta=2\pi}\int_{\rho=0}^{\rho=5mm} \phi_0 \cdot \exp(\frac{-(x + \rho\cos\theta)^2 - (\rho\sin\theta)^2}{2z^2})\rho d\theta dr \tag{4.5}$$

Numerical solutions for different beam width parameter z is calculated and corresponding beam current width parameter s is shown in Fig. 4.5.

Fig. 4.6 shows the relationship between beam width parameter z and calculated corresponding beam current width parameter s. It is almost linear and with a good approximation, it was described by a equation z=a*s+b (z between 3 mm and 10 mm).

4.6.4 Irradiation of a "large" area with protons

The methods described in a note by Korsbech [43] were used to prepare the irradiation experiment set-up system and the theoretical calculations for deter-

(using photographic paper and Charge Coupled Device CCD camera). In our case, the beam shape was assumed to be the same as the beam source was the same cyclotron.

[2]Measurements with a smaller Faraday Cup opening would give current distribution I(r) almost proportional to the fluence rate distribution $\phi(r)$ -and the distributions would have the same width parameter and FWHM [43]

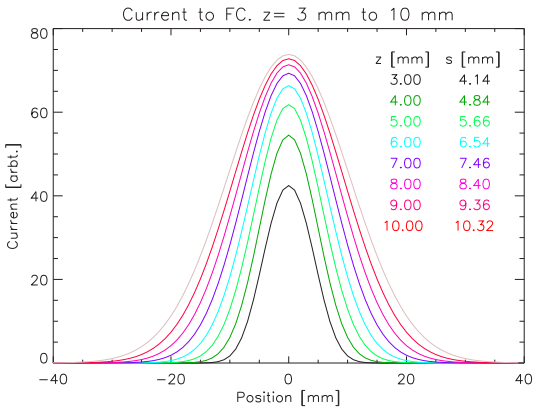

Figure 4.5 Numerical solutions for different beam width parameter z is calculated and the corresponding beam current width parameter s is shown.

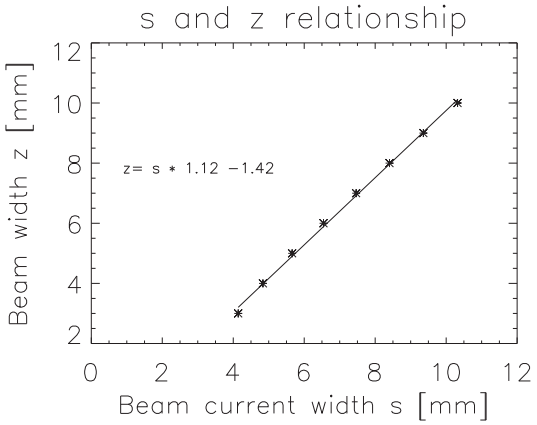

Figure 4.6 The relationship between beam width parameter z and calculated corresponding beam current width parameter s is shown. It is almost linear and with a good approximation, it was described by an equation in form of z=a*s+b (z between 3 mm and 10 mm).

mination of the proton fluences used in the irradiation experiments. The total surface area of the CdZnTe drift strip detector to be irradiated was 1 cm^2. As the circular proton beam was not (see Fig. 4.3) wide enough to expose the detector to an almost homogeneous fluence of protons with stationary beam position, the detector swept across the proton beam in a zigzag path. This is based on moving the detector across the circular proton beam with constant velocity v and with vertical steps $\triangle y$ as illustrated in Fig. 4.7. The fluence Φ can be calculated as follows: Consider the little rectangular area with equal side lengths $\triangle y$ and $\triangle x$. The circle shown in the figure indicates a limit (an iso-fluence rate curve), where the proton fluence rate is 5% (or 1%) of the maximum fluence rate obtained at the center of the proton beam. It is important to emphasize that the vertical steps $\triangle y$ should be selected small enough that the beam is considered sufficiently homogenous within little square equal to $\triangle y \times \triangle x$. The little square is exposed to each part of beam with velocity v for a time $\triangle t$ where $\triangle t = \triangle x/v$. A typical velocity is an order of few mm/s, and typical $\triangle x$ is an order of few mm. For a beam current I (C/s), the beam flow F_{p^+} (p^+/s) (number of particles per time unit) is given by:

$$F_{p^+} = \frac{I}{1.6 \times 10^{-19} \quad C/p^+} \tag{4.6}$$

The fluence to the detector is given by:

$$\Phi = \frac{F_{p^+}}{(\triangle y \times \triangle x)} \cdot \triangle t \tag{4.7}$$

4.7 Results and discussions

This section mainly focuses on the results obtained in connection with the detector charge collection properties as a function of the received proton fluence.

4.7.1 Irradiation

The detector was irradiated from the planar side of the detector in several steps to the proton fluences given in Tab. 4.1 and with an energy of $29.7 \pm 0.7 MeV$. The proton range in CdZnTe as determined with TRIM is 2.89 ± 0.12 mm which is slightly larger than the detector thickness of 2.70 mm. The gamma activity of the detector was measured for 10 min immediately after each irradiation with a Ge detector situated at the Cyclotron facility. The detector was then moved quickly (30 min after the irradiation process) back to the detector laboratory at DSRI, where it was biased and the detector itself was used to

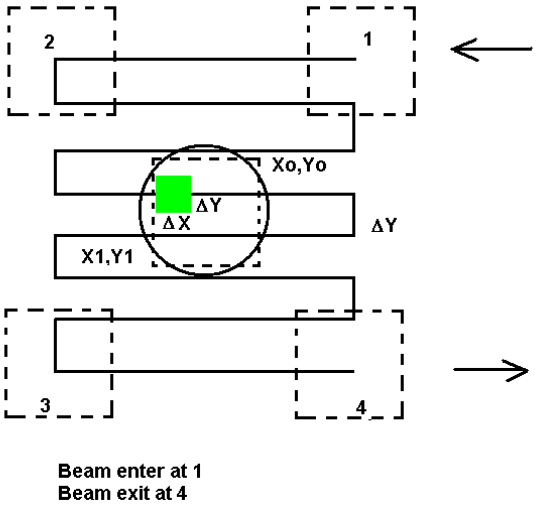

Figure 4.7 The zigzag path. Part of a chip $\triangle y \times \triangle x$ moving in a zigzag path trough the proton beam with constant velocity.

record the produced activity in the CdZnTe material. These measurements lasted typically a few days. The electron mobility-life time product ($\mu\tau_e$) was as the next determined from detector pulse height response measurements using ^{137}Cs and ^{109}Cd radioactive sources. Pulse height spectra were recorded for a set of bias voltages: (Vp,Vd)=(-350V,-117V), (-300V,-100V), (-250V,-85V), (-200V,-66V), (-150V,-50V). The detector was then scanned (2D) with an ~ 400 μm ^{241}Am X-ray beam in order to determine the uniformity of the detector response. Finally, the bulk and surface resistivities of the detector CdZnTe material were measured at room temperature.

The analysis of the detector charge collection properties as a function of proton fluence was based on the detector response measured with the ^{137}Cs and ^{109}Cd sources after the proton irradiation. As an example, Fig. 4.8 compares the bi-parametric distributions of R=Qp/Qs versus Qs measured prior to exposure (left) and after the detector has received a fluence of $60 \times 10^8 p^+/cm^2$ (right). The quantity R is almost linearly dependent on the photon interaction depth, x, with a value close to unity for interactions close to the planar electrode and a value close to zero for interaction near the strip electrodes. The depth axis is also shown (right hand) in Fig. 4.8. Both plots in Fig. 4.8 were obtained irradiating the detector with ^{137}Cs photons and biasing the detector with (Vp,Vd)=(-350V, -117V). The rightmost curves are generated by photo

$\triangle\Phi \quad [p^+/cm^2]$	$\Phi \quad [p^+/cm^2]$	$\mu\tau_e^0 \quad [cm^2/V]$	$\alpha \quad [cm^{-1}]$
Reference	0	4.9×10^{-3}	0
2.3×10^8	2.3×10^8	3.3×10^{-3}	-0.94
4.0×10^8	6.3×10^8	2.4×10^{-3}	-1.01
9.5×10^8	15.8×10^8	1.3×10^{-3}	-1.30
5.7×10^8	21.5×10^8	1.0×10^{-3}	-1.22
38.7×10^8	60.2×10^8	4.9×10^{-4}	-1.06
Annealing	$22h@100^oC$	5.8×10^{-3}	0

Table 4.1 Summary of proton fluencies given to the detector and the derived $\mu\tau_e$ values. The depth dependence of $\mu\tau_e$ was assumed to obey: $(\mu\tau_e(x))^{-1} = (\mu\tau_e^0)^{-1}(1+\alpha x)$, see section 4.7.2, Eq. (4.11)

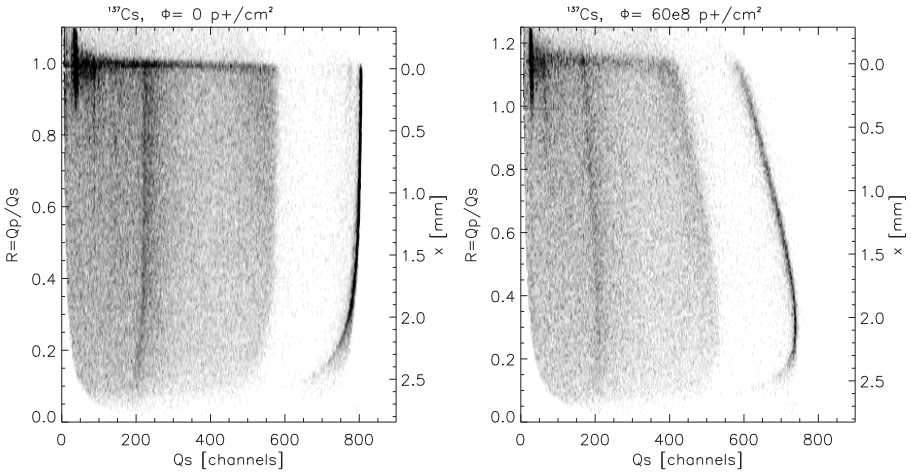

Figure 4.8 The bi-parametric distributions (R versus Qs) measured prior (left) to exposure and after (right) the detector received a fluence of $60 \times 10^8 p^+/cm^2$. The spectra were recorded with the ^{137}Cs source. The right hand axis shows the depth in mm.

absorption of ^{137}Cs 661.6 keV photons. Compton, backscatter and Ba X-ray events can also be seen towards lower Qs values.

The shape difference between the left and right plots, most clear for the 661.6 keV lines, is caused by the higher electron trapping probability in the detector after irradiation. The effect becomes more pronounced the longer the electrons must drift towards the readout strip. Therefore, as seen in the right plot, photons absorbed close to the planar electrode suffer the highest pulse height reduction. Observe also that the width of the 661.6 keV band is larger

for the proton irradiated detector. This is also a consequence of the increased electron carrier trapping since it is a function not only of x; but is determined by the path length of the electron trajectory to the readout strip.

4.7.2 Determination of $\mu\tau_e$

The computer model was developed in order to describe all the measured bi-parametric distributions (Qs,R) both as a function of proton fluence and as a function of the applied bias settings (Vp,Vd). The model is described in previous chapter. In the model, the generated charge cloud was assumed to be point like and the charge diffusion effects were not taken in to account. In the present case, it is expected that the charge traps will be non-uniformly distributed reflecting the damage profile generated by the proton irradiation. Therefore, the model operates with charge trapping lengths, $\lambda(x)$, which are dependent on x. The charge trapping is then described by:

$$Q(E_p;\vec{x},s) = Q_0(E_p)\exp(-\int_x^{x+s}\frac{dt}{\lambda(t)}) \tag{4.8}$$

where the integration is made over the trajectory of the charge cloud. Here, it was assumed that the trapping length $\lambda(x)$ of Eq. (4.8) was given by:

$$\lambda(x) = \mu\tau E(x) \tag{4.9}$$

where E(x) is the electric field inside the detector. E(x) was modelled taking space charge effects into account [44]:

$$E(x) = E_0(x) + (\frac{2V_{dep}x}{d^2} - \frac{V_{dep}}{d}) \tag{4.10}$$

where $E_0(x)$ is the space charge free electric field and V_{dep} is the minimum voltage needed for full depletion. $E_0(x)$ was calculated using the 2D simulation program ELFI. V_{dep} was experimentally determined irradiating the detector from both the planar side (cathode) and the strip side (anode) with photons and alpha particles (^{109}Cd, ^{241}Am) and varying the bias voltage. From these measurements it was found that the detector material is n-type with $V_{dep} = 20 \pm 5$ V.

Fig. 4.9 shows the calculated electric field distribution (across the detector at the center position of the anode strip) within the GSFC-CZT-1 detector. The dashed line shows the calculated electric field using ELFI without taking the space charge effect. The solid line shows the effect of space charge using the model in Eq. (4.10)

The induced signal on the planar (Qp) and the anode strip electrodes (Qs) were calculated using Eq. (4.8) combined with Eq. (4.9). The integrals of

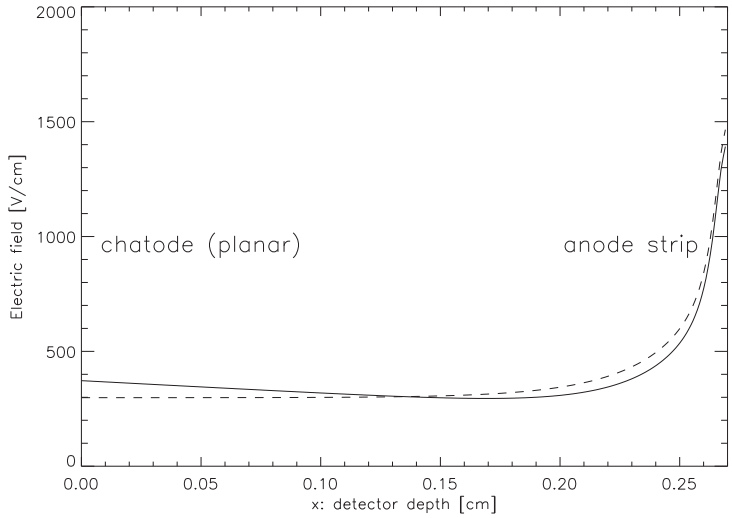

Figure 4.9 The electric field within the GSFC-CZT-1 detector. The dashed line shows the calculated electric field using ELFI without taking the space charge effect. The solid line shows the effect of space charge using the model in Eq. (4.10)

Eq. (4.8) and Eq. (4.9) were numerically evaluated using the precalculated weighting potential Vw(x,y) and electric field E(x,y) (calculated with ELFI using the detector geometry). The model includes the hole contribution to the induced charges, however, this term was in all cases very small, i.e., $\mu\tau_h << \mu\tau_e$. Therefore, it is assumed that $\mu\tau_h$ is zero in the model. A detailed description of the model is given in section 3.6.

As an example of the model calculations, Fig. 4.10 shows (upper) the calculated correlation between Qs and R for mono energetic photons assuming the present detector geometry and $\mu\tau_e = 0.6 \times 10^{-3}\, cm^2/V$. The detector bias voltage was selected to be -350V.

This figure is to be compared with the right plot in Fig. 4.8. The lower part of Fig. 4.10 displays the near linear dependence of the correlation between the depth parameter, x and R.

The model was used to derive $\mu\tau_e(x)$ from the experimental Qs versus R relations measured for all proton fluences and all bias settings. The present analysis is based on the Qs versus R relations obtained for the ^{137}Cs 661.6 keV photons. The full curves in Fig. 4.11 compares the Qs versus R relations measured for all the different proton fluence levels, but for the same detector bias of (Vp,Vd)=(-250V,-85V). The data were derived from the bi-parametric

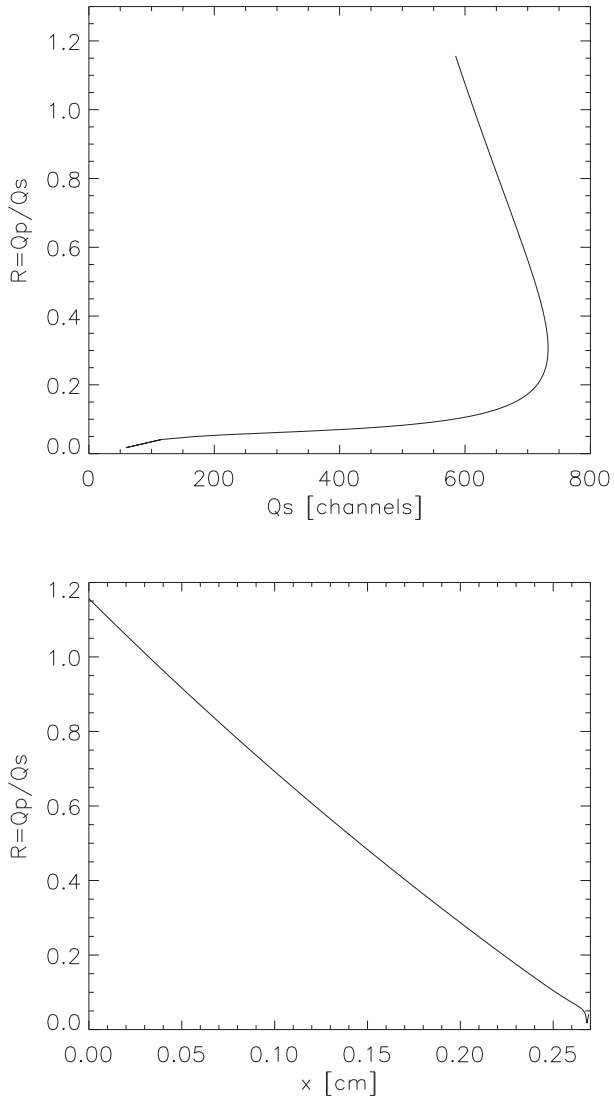

Figure 4.10 Model simulations. The upper plot shows the calculated Qs versus R correlation for the $\mu\tau_e = 0.6 \times 10^{-3}\ cm^2/V$ and Vp=-350V. The lower plot shows the calculated correlation between x and R.

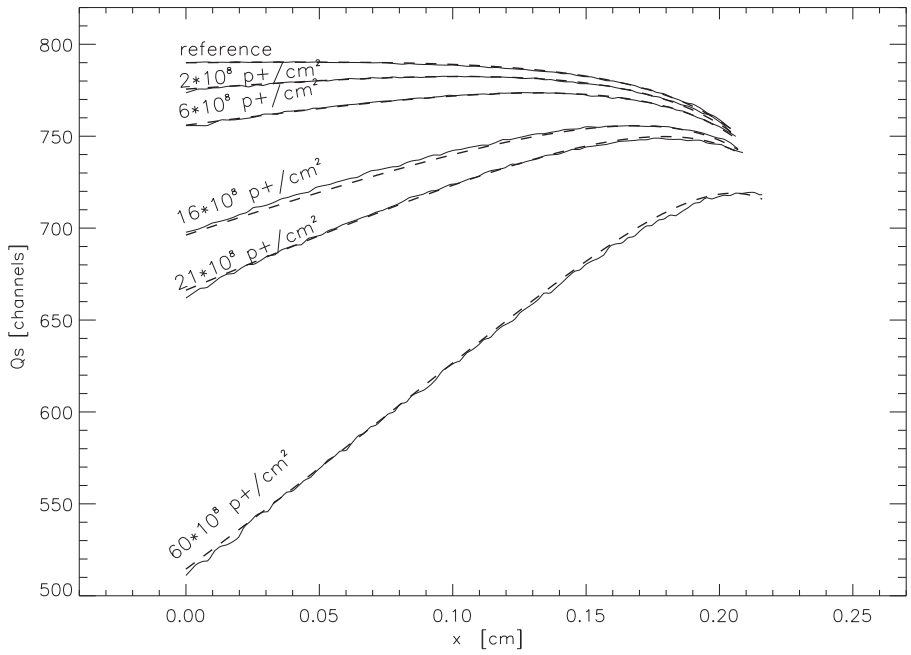

Figure 4.11 The Qs versus depth x relations measured (full lines) for the different proton fluence with a detector bias of (Vp,Vd)=(-250V,-85V). The dashed lines show the model results.

distributions as shown in Fig. 4.8 from which the 661.6 keV line positions for each R value were determined by Gauss fitting. The detector model was adjusted to the experimental data treating $\mu\tau_e(x)$ as a free parameter. Initially, it was expected that the shape of the trapping probability could be estimated from the Monte Carlo simulations of the radiation damage profile as calculated by the simulation program TRIM [42]. Fig. 4.12 (upper) shows the calculated damage profile for 30 MeV protons in the detector assuming a density of 5.8 g/cm3 for the CdZnTe material. Notice that the damage increases towards the strip side of the detector. However, it was impossible to achieve good agreement with the experimental data assuming a shape of $(\mu\tau_e)^{-1}$ (proportional to the trapping probability) like the shown damage profile. An excellent agreement, however, could be obtained assuming a depth dependence of the form:

$$(\mu\tau_e(x))^{-1} = (\mu\tau_e^0)^{-1}(1 + \alpha x) \tag{4.11}$$

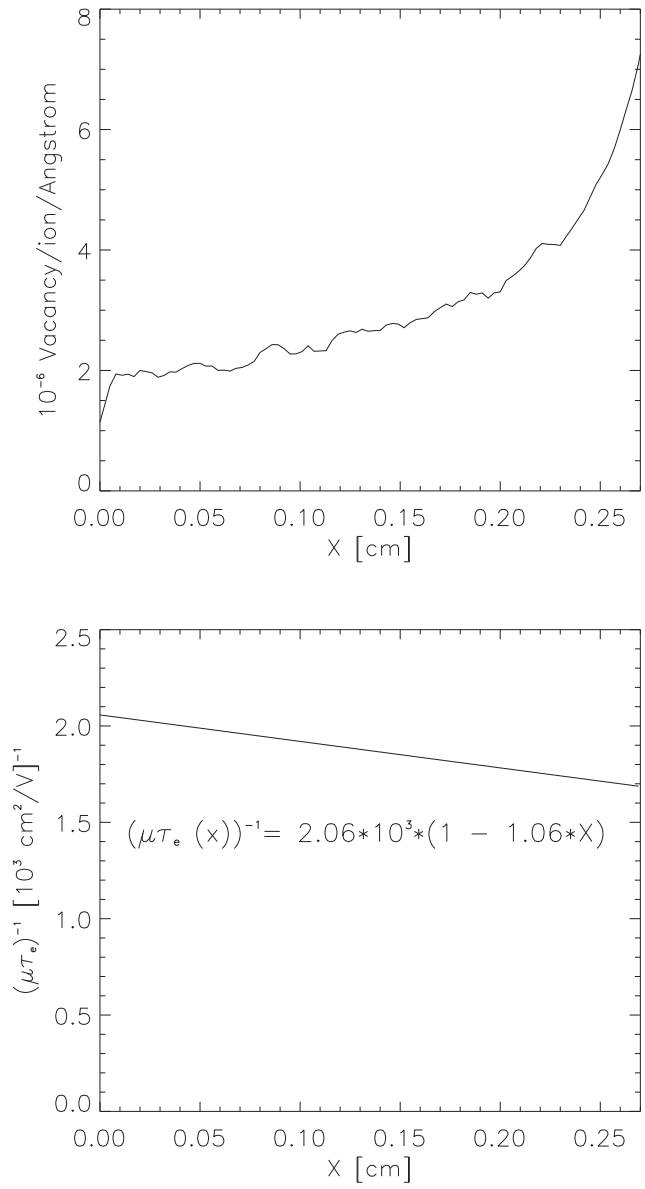

Figure 4.12 Upper: The proton induced damage profile calculated using the Monte Carlo simulation program TRIM [42]. Lower: The derived $(\mu\tau_e)^{-1}$ behavior for a proton fluence of $60 \times 10^8 p^+/cm^2$.

The good agreement can bee seen in Fig. 4.11, where the dashed lines show the model results. The resulting $\mu\tau_e^0$ and slope (α) values are presented in Tab. 4.1. The behavior of $(\mu\tau_e)^{-1}$ obtained after a proton fluence of $60 \times 10^8 p^+/cm^2$ is shown in the lower part of Fig. 4.12. It is surprising that the present results shows that the electron trapping probability decreases with depth rather than increases as predicted by TRIM simulation. The reason for this is at present not clear. As a possibility, part of the radiation damage may be created by nuclear reactions, mainly (p,xn) reactions, which are not included in the TRIM. The recoiling nucleus following a nuclear reaction may produce many lattice defects during slowing down. The damage yield from these processes will obviously approach zero as the proton energy decreases.

The measured dose dependence for the electron trapping is illustrated in Fig. 4.13, where the depth averaged reciprocal $\mu\tau_e$ values are plotted versus the proton fluence. The relation is linear with an offset value given by the detector before proton irradiation and a slope, which yields the contribution to the electron trapping, produced by the proton irradiation:

$$(\mu\tau_e(x))^{-1}_{rad} = (2.5 \pm 0.2) \times 10^{-7} \cdot \Phi \quad [V/cm^2] \tag{4.12}$$

with Φ in $[p^+/cm^2]$. The equation can be expressed as a function of received proton dose, D assuming an initial proton energy of 30 MeV:

$$(\mu\tau_e(x))^{-1}_{rad} = (0.8 \pm 0.1) \times 10^3 \cdot D \quad [V/cm^2] \tag{4.13}$$

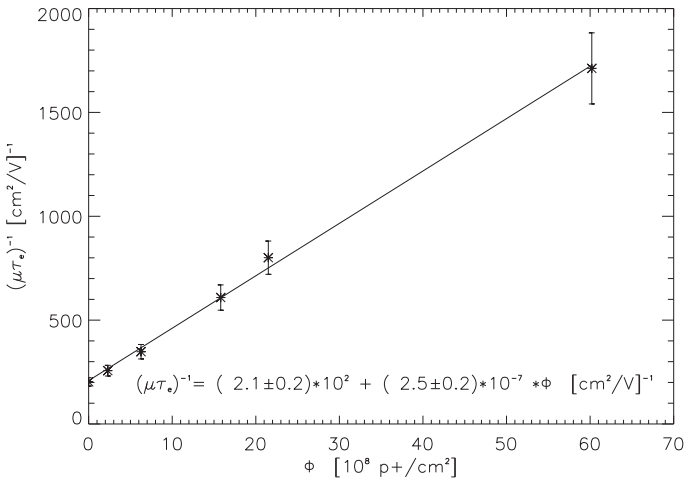

Figure 4.13 Average $(\mu\tau_e)^{-1}$ values as a function of the proton fluence.

with D in [$krad$]. This equation is of general use also, when proton radiation effects for other types of CdZnTe detector types have to be estimated.

4.7.3 The leakage current measurements

The bulk and the surface leakage current of the detector were measured before and after each proton irradiation. All the leakage current measurements were taken at 22 ± 1^oC. A Keithley instrument (602 solid-state electrometer) and a ORTEC 556 HV power supply was used for the measurements. In the case of bulk leakage current, the planar electrode bias was varied in steps from -100V to +100V and the current flowing through all the strips (connected as one electrode) was measured. In the case of surface leakage current, the V1 drift electrode bias was varied in steps from -25V to +25V and the current flowing through each of the readout strips was measured. The slopes of the measured I-V curves changed with bias polarity and the following results shown in Fig. 4.14 and Fig. 4.15 refer to the polarities used during normal detector operation. The leakage currents were found to increase slightly with the detector proton irradiation and we found that the detector bulk resistance decreased from 88 $G\Omega$ to 68 $G\Omega$ after the last irradiation whereas the typical inter strip resistance decreased from 12 $G\Omega$ to 7.5$G\Omega$ during the irradiation. The detector bulk resistance decreased to 56 $G\Omega$ after the detector was annealed 22h at 100^oC whereas the inter strip resistance decreased to 4.7 $G\Omega$. Further investigation is needed in order to explain the dramatic increase of the leakage current after the annealing. One possible explanation can be metal diffusion through the oxide layer and into the semiconductor at higher temperature make the contacts more ohmic.

4.7.4 Energy resolution vs proton fluences

The decreased values of $\mu\tau_e$ induced by the proton damage lead to down shifts of the detector line peaks. This effect was illustrated in Fig. 4.8 and can also be seen in Fig. 4.16, which compares a ^{137}Cs spectrum taken before proton irradiation with a spectrum taken after the last irradiation. The spectra were obtained from the bi-parametric data shown in Fig. 4.8 and were corrected for the R dependence of Qs in a manner described in Chapter 3, section 3.3 and such that Qs is normalized to the value it has close to the common planar electrode (x=0). The spectra in Fig. 4.16 include all events within the detector. The 661.6 keV line for the damaged detector is shifted downwards by $\sim 25\%$; but even more remarkably is the large increase of a factor 5 of the width of the 661.6 keV peak. It should be underlined that the spectra, using the depth sensitivity of the present detector, is corrected for the electron trapping effect as function of x. Detectors without the depth sensitivity will suffer from

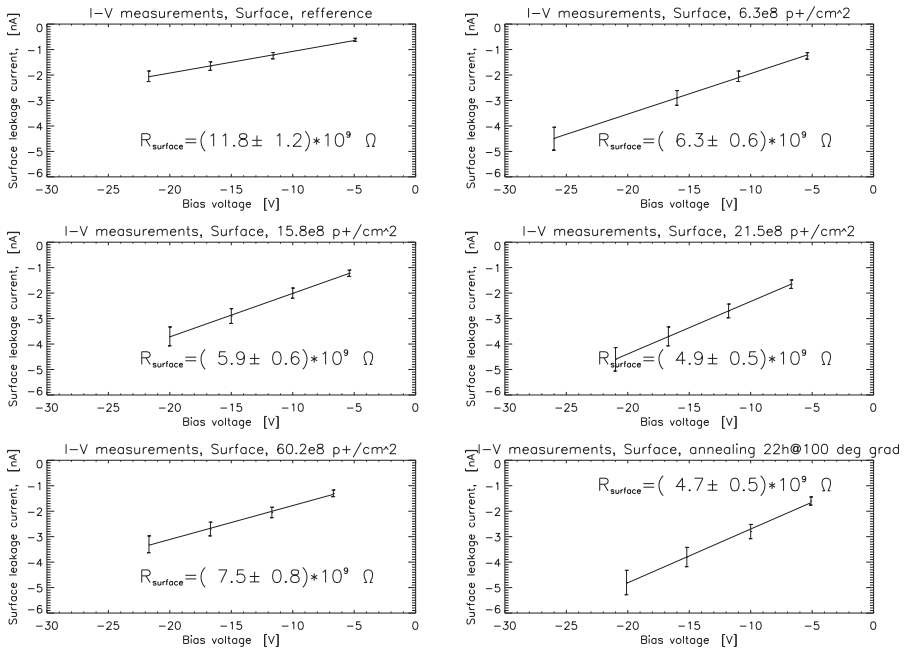

Figure 4.14 Detector surface leakage current measurements after each irradiation process.

a contribution to the energy resolution which is directly proportional to the spread of the photon absorption depths. However, Fig. 4.16 shows that even with implementation of the correction, there is a significant energy resolution degradation after irradiation. The effect of proton damage is further illustrated in Fig. 4.17. Here, the detector relative energy resolutions Δ_{rad}(FWHM) measured at three different energies are plotted as function of proton fluence. The detector was biased with Vp=-350,Vd=-117 V and was subsequently illuminated with photons from an ^{241}Am source (60 keV), ^{109}Cd source (88 keV) and a ^{137}Cs source (661.6 keV). Δ_{rad} is given for those events which interacts close to the planar electrode (x=0) and for which the electron carriers drift all the way through the detector volume. Furthermore, the widths measured for the undamaged detector have been quadratic subtracted. Δ_{rad} is thus the contribution to the energy resolution produced by the radiation damage. From Fig. 4.17 one can see that Δ_{rad} is independent of photon energy and is vary-

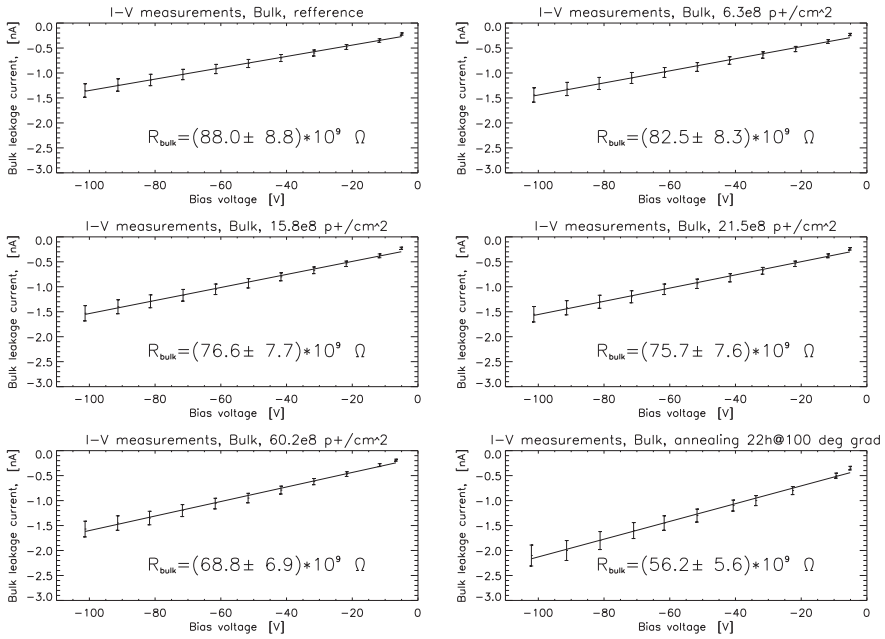

Figure 4.15 Detector bulk leakage current measurements after each irradiation process.

ing proportional to the proton fluence. The behavior is rather well explained when the variance of the length of the electron drift path is considered. With help of the simulation program ELFI, it was determined that the drift length for electrons following the electric field lines through the detector fluctuates with a standard deviation of $\sigma(x) = 0.10$ mm. The resulting charge collection fluctuation can be expressed by:

$$\Delta_{rad} = 2.35 \cdot (\mu\tau_e)^{-1}\sigma(x)/E(x) \tag{4.14}$$

The contributions calculated from this expression using our measured $(\mu\tau_e)^{-1}_{rad}$ values are plotted as square symbols in Fig. 4.17. The agreement with the measured energy resolution is good and we conclude that the radiation damaged detector energy resolution is determined by the change of $\mu\tau_e$.

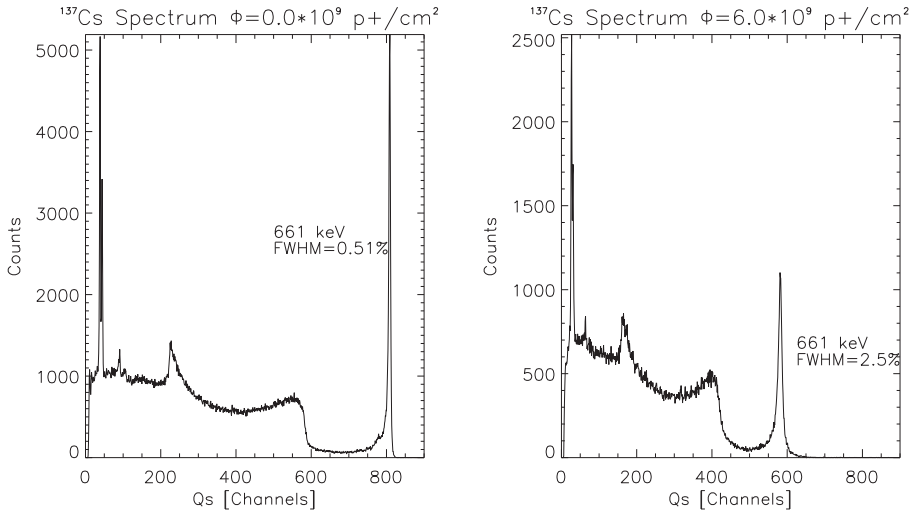

Figure 4.16 ^{137}Cs spectrum before proton irradiation (left) and after the last irradiation (right). The spectra were obtained from the bi-parametric data shown in Fig. 4.8 and were corrected for the R dependence of Qs in a manner described in Chapter 3. The 661.6 keV line for the damaged detector is shifted downwards by 25%; but even more remarkably is the large increase of a factor 5 of the width of the 661.6 keV peak.

4.7.5 Activation spectra

As stated above, the detector was after each irradiation step moved to the detector laboratory, biased and the activity of the produced radioactive isotopes in the CdZnTe material were recorded by the detector itself. Recording of the activation spectra was started 30 min after the proton irradiation was stopped. Fig. 4.18 shows a log plot of the activation spectrum which was recorded after the last irradiation step ($\Delta\Phi = 3.9 \times 10^9\ p^+/cm^2$). Although the detector energy resolution at this state was severely degraded, three lines stemming from the decay of meta stable states of ^{112m}In, ^{113m}In and ^{115m}In, respectively are clearly visible. These nuclei are produced by (p,xn) reactions (x=1,2,3) on the available Cd isotopes in the detector material. The meta stable nuclei decay mainly by internal conversion [45] and their decay is detected by conversion electrons rather than photons. The conversion electrons have a short range ($< 100\ \mu m$) in CdZnTe. The R distributions obtained by the drift strip detector can therefore be used to determine the production yields of the isotopes as function of depth, x in the detector. Fig. 4.19 shows the depth dependence

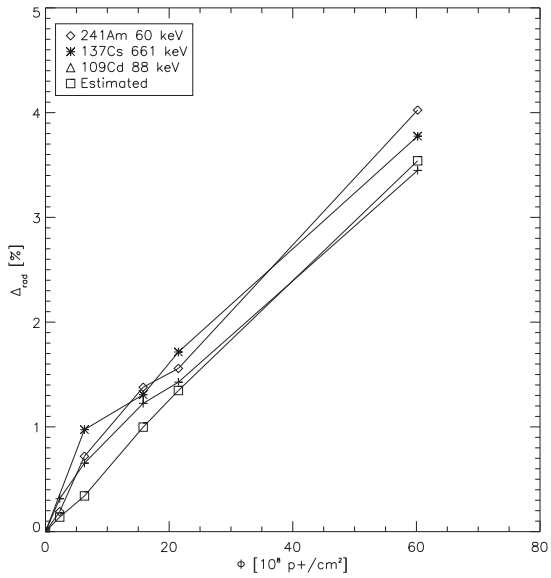

Figure 4.17 The detector relative energy resolutions Δ_{rad}(FWHM) measured at three different energies are plotted as function of proton fluence. The detector was biased with Vp=-350,Vd=-117 V and was subsequently illuminated with photons from an ^{241}Am source (60 keV), ^{109}Cd source (88 keV) and a ^{137}Cs source (661.6 keV).

of the production yields derived for the three isotopes. The yields reflect the available proton energy as function of depth. The (p,3n) reactions are energetically possible ($Ep > 22$ MeV) for depth values less than 1 mm. However, since both ^{115}Cd and ^{117}Cd are absent (unstable) in the detector material 113mIn and 115mIn are not produced by (p,3n) reactions. This explains the difference between the ^{112m}In yield and those for ^{113m}In and ^{115m}In.

4.7.6 Annealing

The detector was exposed to an annealing process after the proton irradiations and the detector evaluations were finished. The annealing was performed in steps of 2h duration at 100 ^oC and subsequent determination of $\mu\tau_e$ in the same manner as described above. The process was stopped after 22 hours´ total annealing time when $\mu\tau_e$ did not change anymore. The detector response was completely recovered with a $\mu\tau_e$ of $5.8 \times 10^{-3} cm^2/V$, which in fact is slightly higher than the value (reference) found before the radiation

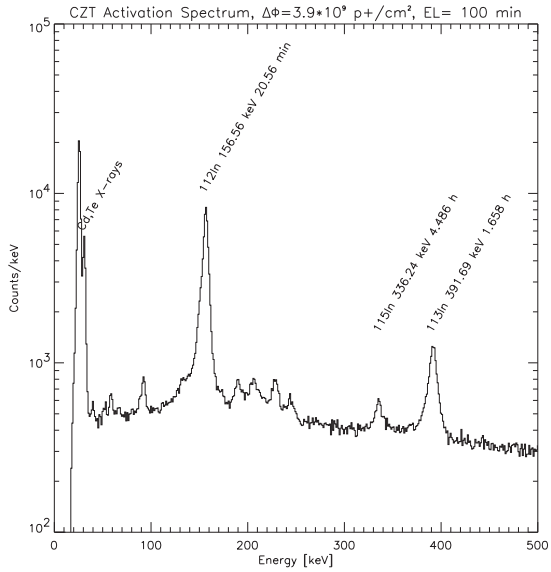

Figure 4.18 The activation spectrum which was recorded after the last irradiation step ($\Delta\Phi = 3.9 \times 10^9\ p^+/cm^2$). Although the detector energy resolution at this state was severely degraded, three lines stemming from the decay of meta stable states of ^{112m}In, ^{113m}In and ^{115m}In, respectively are clearly visible.

process was started. Also the detector energy resolution was recovered with a width (FWHM) of 4.04 keV for the ^{137}Cs 661.6 keV line measured with a bias of (Vp,Vd)=(-350V,-150V) and in good agreement with the reference data. Thus, the present work confirms the annealing properties for radiation damaged CdZnTe detectors reported by Wong *et al.* [39].

4.7.7 Discussion

A study of radiation effects exposing a 2.7 mm thick CdZnTe drift strip detector to 30 MeV protons was performed for fluences up to $60 \times 10^8 p^+/cm^2$. Even for the highest fluences, which had a dramatic effect on the spectroscopic performance, it was possible to recover the detector response after an appropriate annealing procedure. The radiation damage was studied as a function of depth inside the detector material. $\mu\tau_e$ of the CdZnTe detector material was determined as a function of the proton fluence. The analysis showed that the electron trapping increased proportional with the proton fluence and the radiation contribution to the electron trapping obeyed the rela-

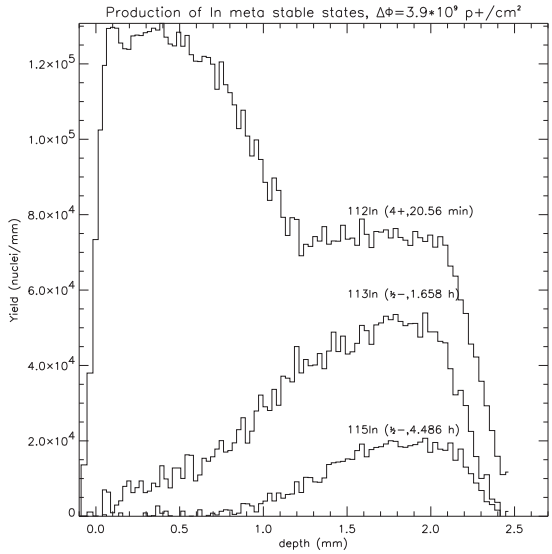

Figure 4.19 The depth dependence of the production yields derived for the three isotopes in Fig. 4.18. The yields reflect the available proton energy Ep as function of depth.

tion: $(\mu\tau_e)^{-1}_{rad} = (2.5 \pm 0.2) \times 10^{-7} * \Phi \qquad [V/cm^2]$ with the proton fluence, Φ in p^+/cm^2. The trapping depth dependence, however, did not agree well with the damage profile calculated using the Monte Carlo simulations, TRIM [42], for the proton induced radiation effects. The present results suggest that proton induced nuclear reactions may contribute significantly to the radiation damage. More work is needed in order to elaborate on these effects.

The leakage currents were found to increase slightly with the detector proton irradiation and it was observed that the detector bulk resistance decreased from 88 $G\Omega$ to 68 $G\Omega$ after the last irradiation whereas the typical inter strip resistance decreased from 12 $G\Omega$ to 7.5 $G\Omega$ during the irradiation. The detector bulk resistance decreased to 56 $G\Omega$ after the detector was annealed 22h at 100 ^oC whereas the inter strip resistance decreased to 4.7 $G\Omega$.

Results show that the damage below the surface of the material caused by the primary knock-on atom (primary atom in the collision cascade) is obtained from the collision of the incident particle and the stationary atom is significant. Energy, transferred to the stationary atom, is dependent on the mass and energy of the incident particle. The results of this investigation are insufficient to determine the primary cause of damage. The series of tests using higher

proton energy is required to begin to formulate conclusions about the primary cause of the radiation.

After an annealing process in steps of 2h duration at 100 ^oC with a total annealing time of 22 hours', the detector response was completely recovered with a $\mu\tau_e$ of $5.8 \times 10^{-3} cm^2/V$, which in fact is higher than the value $4.9 \times 10^{-3} cm^2/V$ (reference) found before the radiation process was started. Also the detector energy resolution was recovered with a width (FWHM) of 4.04 keV for the ^{137}Cs 661.6 keV line measured with a bias of (Vp,Vd)=(-350V,-150V) and in good agreement with the data reported by Wong *et al.* [39].

Summary

This work covers a comprehensive investigation of the issues confronting radiation damage in the CdZnTe drift strip detectors planned for use as space instrumentation. Five main problems requiring investigation are identified and addressed including requirement specification with particular emphasis on device material properties, particle induced radiation damage, energy resolution improvement, noise minimization, and electron sensitive detector geometry.

Correlation of large area CdZnTe crystal with detector performance

One of the critical challenges for using large area CdZnTe detector material is to get a material with uniform imaging and spectroscopic responds. Commercially available CdZnTe crystals are usually polycrystalline in nature. Cracks and macroscopic structural defects in the material related to the crystal growing are present in these crystals. These defects (the grain boundaries) are important issues, which are known to trap charge carriers and degrade the performance of the detector. One of the strip detectors (BSI-CZT-2) was investigated related to this problem. The detector material was classified by the manufacturer.

The detector has shown a significant spectral non-uniformity and was suspected to suffer spectral performance degradation caused by the grain boundaries.

A material defect study was conducted on the detector by an X-ray scan in order to show the negative impact on the detector performance. The scan was performed to the BSI-CZT-2 at the Space Radiation Laboratory at Caltech (in connection with this Ph.D. study). It was found that the peak positions in some places were shifted significantly which was correlated to the crystal grain boundaries with very poor charge transport properties within the defect area of the material. The X-ray scan unveiled a non-uniform material. The effect of the grain boundaries on the detector performance was catastrophic. Therefore, the CdZnTe crystals which are to be used as detector material should be tested for this type of material defects with an X-ray mapping.

CdZnTe drift strip detectors

The drift strip method (DSM) applied to the CdZnTe detectors with moderate $\mu\tau_e$ leads to a dramatic improvement of the achievable energy resolution. The DSM does not require event rejection as the pulse processing techniques does. This can be an important property especially for space applications for statistical reasons.

Three CdZnTe drift strip detectors were designed and fabricated. The CdZnTe crystals were all obtained from eV-products. The detectors were specified to be spectrometer grade single crystals with a size of 10 mm x 10 mm x 3 mm. All the detectors were specified consistently to have a thickness of 3 mm.

A numerical computer model for the CdZnTe drift strip detector using the mathematical detector model is developed. In order to reduce the complexity of the solution, the symmetry of the geometry together with a few assumption were used. First, the electric field and the weighting potential are assumed to be constant parallel to the strips. Therefore, the electric field and the weighting potential were calculated in two-dimensional for the cross-section of the drift detector cell. Secondly, the generated charge cloud was assumed to be point like and the charge diffusion effect was not taken in to account in the model.

The numerical computer model uses precalculated data from the electrostatic analysis using the detector geometry and the operation voltages.

The electrostatic analysis was performed on the GSFC-CZT-1 and the GSFC-CZT-1 detector using the detectors' physical dimensions and the electrode geometries.

Comparison between the experimental data and the numerical computer model for the CdZnTe drift strip detectors showed good agreement. This model is mainly used to determine electron transport properties of CdZnTe material. Especially, the model was used to derive $(\mu\tau_e)(\mathrm{x})$ of the CdZnTe material from the experimental Qs versus R relations measured for all proton fluences and all bias settings for the irradiation experiments.

The $\mu\tau_e$ for the GSFC-CZT-1 and the GSFC-CZT-4 were measured as $5 \times 10^{-3}\ cm^2/V$ and $8 \times 10^{-3}\ cm^2/V$, respectively.

The performance of the detectors for X-ray and gamma-ray spectroscopy was evaluated. The spectral response for each detector was measured. Noise measurements were made under optimal operating conditions using a pulse generator. All measurements have shown that the resolution was limited by the total electronic noise below 100 keV.

The GSFC-CZT-4 yields some of the best performance figures yet reported for full illumination. For example, at 356 keV the FWHM energy resolutions were 2.87 keV at detector temperatures of -15^oC. At 60 keV, the corresponding resolution was 1.1 keV at detector temperatures of -10^oC. These should be

compared to the calculated Fano resolutions 500 eV at 60 keV.

The best results, in terms of energy resolution, were obtained from these detectors. For the best spectral response, the GSFC-CZT-4 was characterized using the NIM system with the BSI-electronic box as the first stage preamplifiers. Energy resolution of the GSFC-CZT-4, using ^{241}Am, ^{109}Cd, ^{133}Ba and ^{137}Cs calibration sources was measured at temperature range between -10^oC and -15^oC. The GSFC-CZT-4 yields some of the best performance figures yet reported for full illumination of wide energy range. For example, at 356 keV the FWHM energy resolution was 2.87 keV at modest detector temperatures of -15^oC. At 60 keV, the corresponding resolution was 1.1 keV FWHM at detector temperature of -10^oC. These should be compared to the calculated Fano resolution 500 eV FWHM at the 60 keV. At the lower energies, the measured resolution was dominated by leakage current. However, at medium and high energies, the Fano noise became an appreciably fraction of the resolution function. The present results suggest that DSM can achieve energy resolutions which are within a factor of 2 of the Fano-limited resolution for the CdZnTe material.

Radiation damage in the CdZnTe drift strip detector

The research described in this dissertation mainly concerns the experimental studies of the radiation damage effects of a 2.7 mm thick CdZnTe drift strip detector, exposed to 30 MeV protons in order to describe the effect on the electron trapping characteristic of the material. The experimental studies have been performed at DSRI, in collaboration with the cyclotron facility at Copenhagen University Hospital. The detector characteristics were evaluated after exposure to a number of proton fluences in the range from 2×10^8 to $60 \times 10^8 p^+/cm^2$. A significant part of this work is devoted to the research and development of new data-acquisition and hardware for use with irradiation experiment. An XY-table and a mechanical chopper were developed in order to achieve suitable beam currents. A Faraday Cup (FC) was attached to the system in order to measure the beam intensity and the beam profile, just before the irradiation process. A new system for set-up control, multiparameter data-acquisition, monitoring, and data analysis were developed. At present, this system is routinely used in all irradiation experiments at the cyclotron facility at Copenhagen University Hospital, including the irradiation experiments described in this work.

The radiation damage was studied as a function of the depth inside the detector material. $\mu\tau_e$ of the detector CdZnTe material was determined as a function of the proton fluence. The analysis showed that the electron trapping increased proportional with the proton fluence and the radiation contribution

to the electron trapping obeyed the relation:

$(\mu\tau_e)^{-1}_{rad} = (2.5 \pm 0.2) \times 10^{-7} * \Phi \qquad [V/cm^2]$

with the proton fluence, Φ in p^+/cm^2.

The trapping depth dependence, however, did not agree well with the damage profile calculated using the Monte Carlo simulations, TRIM [42], for the proton induced radiation effects. The present results suggest that proton induced nuclear reactions contribute significantly to the radiation damage. Energy, transferred to the stationary atom, is dependent on the mass and the energy of the incident particle. Obtained damage profile results indicate that the damage is significant below the surface of the material caused by the primary knock-on atom (primary atom in the collision cascade). Further investigation is needed to to elaborate on these effects.

The detector energy resolution was investigated as function of proton fluence. It was found that the observed degradation is well explained by the decrease of $\mu\tau_e$ when the fluctuations of the electron path length are taken into account.

The leakage currents were found to increase slightly with the detector proton irradiation and it was observed that the detector bulk resistance decreased from 88 $G\Omega$ to 68 $G\Omega$ after the last irradiation whereas the typical inter strip resistance decreased from 12 $G\Omega$ to 7.5 $G\Omega$ during the irradiation. The detector bulk resistance decreased to 56 $G\Omega$ after the detector was annealed 22 hours at 100 ^oC whereas the inter strip resistance decreased to 4.7 $G\Omega$.

Even for the highest proton fluences ($60 \times 10^8 p^+/cm^2$), which had a dramatic effect on the spectroscopic performance of the detector, it was able to recover the detector performance after an appropriate annealing procedure. The detector response was completely recovered with a $\mu\tau_e$ of $5.8 \times 10^{-3} cm^2/V$, which in fact is higher than the value $4.9 \times 10^{-3} cm^2/V$ (reference) found before the radiation process was started. Also the detector energy resolution was recovered with a width (FWHM) of 4.04 keV for the ^{137}Cs 661.6 keV line measured with a bias of (Vp,Vd)=(-350V,-150V) and in good agreement with the reference data.

A

Appendix

A.1 CdZnTe drift pixel detector

A.1.1 Introduction

The DSM was applied as a pixel geometry and finally, the eV-CZT-1 and the eV-CZT-2 were designed and ordered from eV-products in the beginning of the last year of this research. The fabrication of the detectors were considerably behind schedule due to complicated electrode geometry and electrical connections which took longer time than planned. Furthermore, even though the detectors were fabricated, they could not be received in time, due to the unexpected obstacles such as export license. While completing this thesis, the detectors were not received yet.

The detector pixel size was specified in connection with a proposal, The Atmosphere-Space Interaction Monitor (ASIM). The pixel detector proposed in this mission specified as having 16 pixels on 1 cm^2 CdZnTe. Optimal electrode geometry was obtained using a model and electrostatic calculations. The drift pixel electrode geometry is shown in Fig. A.1. The pixel pitch is 2 mm. The crystal size is 10×10 mm^2. The center electrode radius is 0.2 mm. Inner and outer radius for the first surrounding drift electrode is 0.5 mm and 0.6 mm, respectively. The rectangular common drift electrode is 0.1 mm width. The first drift electrodes are interconnected externally by flip-chip technique.

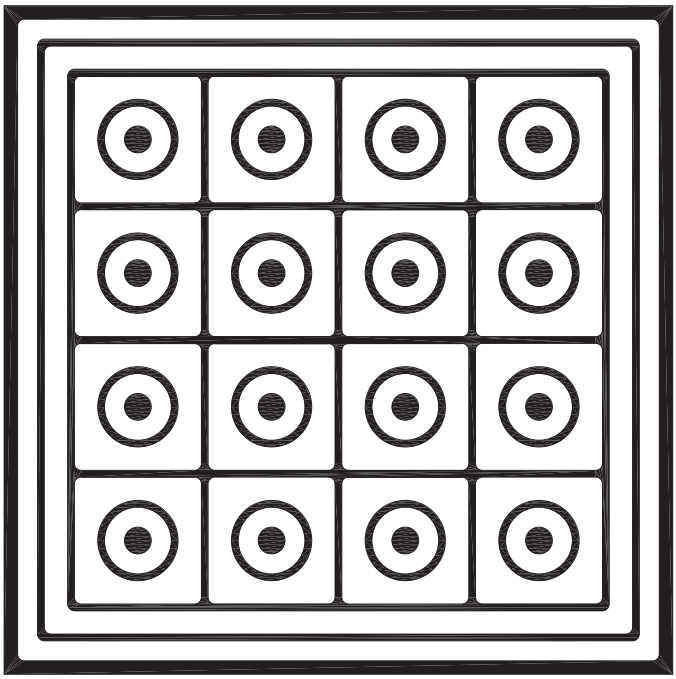

Figure A.1 The drift pixel electrode geometry. The pixel pitch is 2 mm. The crystal size is $10 \times 10\ mm^2$. The center electrode radius is 0.2 mm. Inner and outer radius for the first surrounding drift electrode is 0.5 mm and 0.6 mm, respectively. The rectangular common drift electrode is 0.1 mm width. The first drift electrodes are interconnected externally by flip-chip technique.

A.2 ASIC detector read-out electronic

A low-noise low-power 16 channel preamplifier/shaper Application Specific Integrated Circuit (ASIC) chip designed at eV-products is described in this chapter.

A.2.1 Introduction

It was planned to use an Application Specific Integrated Circuit (ASIC) chip from eV-products as a read-out electronic for the CdZnTe drift pixel detector. This project was planned and started in the last year of this Ph.D study, however, due to unforeseen circumstances (e.g., many redesigned test boards

due to poor documentation from the ASIC manufacturer and lack of technician time due to priorities) the project was delayed and was finished only 3 weeks before the dead line of this thesis. Nevertheless, noise measurements were conducted at room temperature with a CdZnTe drift strip detector (GSFC-CZT-4) connected to the ASIC chip.

A.2.2 ASIC chip

The ASIC operates on a +3Volt power supply and incorporates both a charge-sensitive preamplifier and a five pole shaping amplifier (unipolar). The Gaussian output signal is proportional to the incident X- or gamma ray collected by the detector. The ASIC can be used in the 10keV to 1.5MeV energy range.

The shaping time is selectable between 0.6, 1.2, 2.4 and 4 μs, so that an optimum noise performance can be achieved over a wide range of detector leakage currents. The noise is limited to 75 electrons rms for 1.2 μs shaping, plus 15 electrons rms per pF. The gain is selectable between 33, 50, 100 200 mV/fC.

A.2.3 The test-board

In order to employ the ASIC chip, a test-board was designed and built. The GSFC-CZT-4 is coupled to this ASIC chip trough connectors and the whole structure is mounted in an aluminium housing. Fig. A.2 shows the ASIC chip mounted on a Printed Circuit Board (PCB) special designed for the ASIC chip. The detector is placed on the other side of the PCB.

A.2.4 Experimental Results

In order to investigate the noise contribution to the line spread function, the internal eV-ASIC pulser circuit connected to the inputs of the ASIC was used. This measurement is made by using the test pulse input of the ASIC chip. This pin provides the ability to connect a test pulse to the input of each preamplifier/ shaper channel and requires no additional components. This signal is coupled to the pre-amplifier input via an on-chip C_{test} = 100 fF series capacitor and a 50 Ω shunt termination resistor. The charge injected by the test pulse can be calculated by using the equation $Q_{test} = C_{test} * V_{step}$. To calculate the expected output of an ASIC channel the equation Output = Q_{test}*Ch*Gain(mV/fC) is used. Only 6 channels of the 16 channels were used during the measurements. Each of these 6 channels were connected to each of the 6 anode strips of the GSFC-CZT-4. The operation voltages of (Vp,Vd)=(-300V,-100V) were used. Noise characteristic of the 6 channels were measured with combination of gain and shaping time.

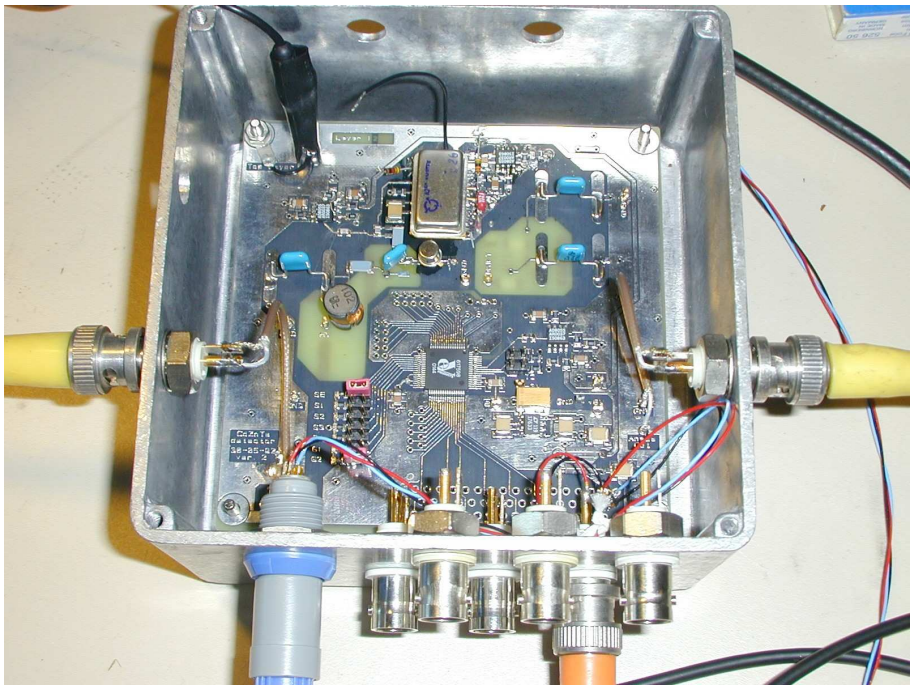

Figure A.2 The ASIC chip mounted on a Printed Circuit Board (PCB). The detector is placed on the other side of PCB.

The measured total electronic noise (in keV) as a function of shaping time with different gain settings are plotted in Fig. A.3.

Total electronic noise measurements of the ASIC alone show a line spread function of less than 2.0 keV, indicating that noise generated within the ASIC electronics is not the dominant component of the noise contribution. Pulser resolution measurements with the CdZnTe detector connected to the ASIC inputs are indicating that the dominant source of noise contributing to the energy independent noise term is external to the ASIC and mainly comes from the detector leakage current.

Spectra using ^{137}Cs was recorded from the detector system. The result shows that the eV-ASIC works as predicted. Spectrum is shown in Fig. A.4 for ^{137}Cs. Due to the lack of time, only a few spectra were obtained from the detector system and only shaping time of 1.2 μs and gain of 200 mV/fC are used for the measurements. The operation temperature was 22^oC. The operation voltages were Vp=-300V and Vp=-100V. A full characterization is

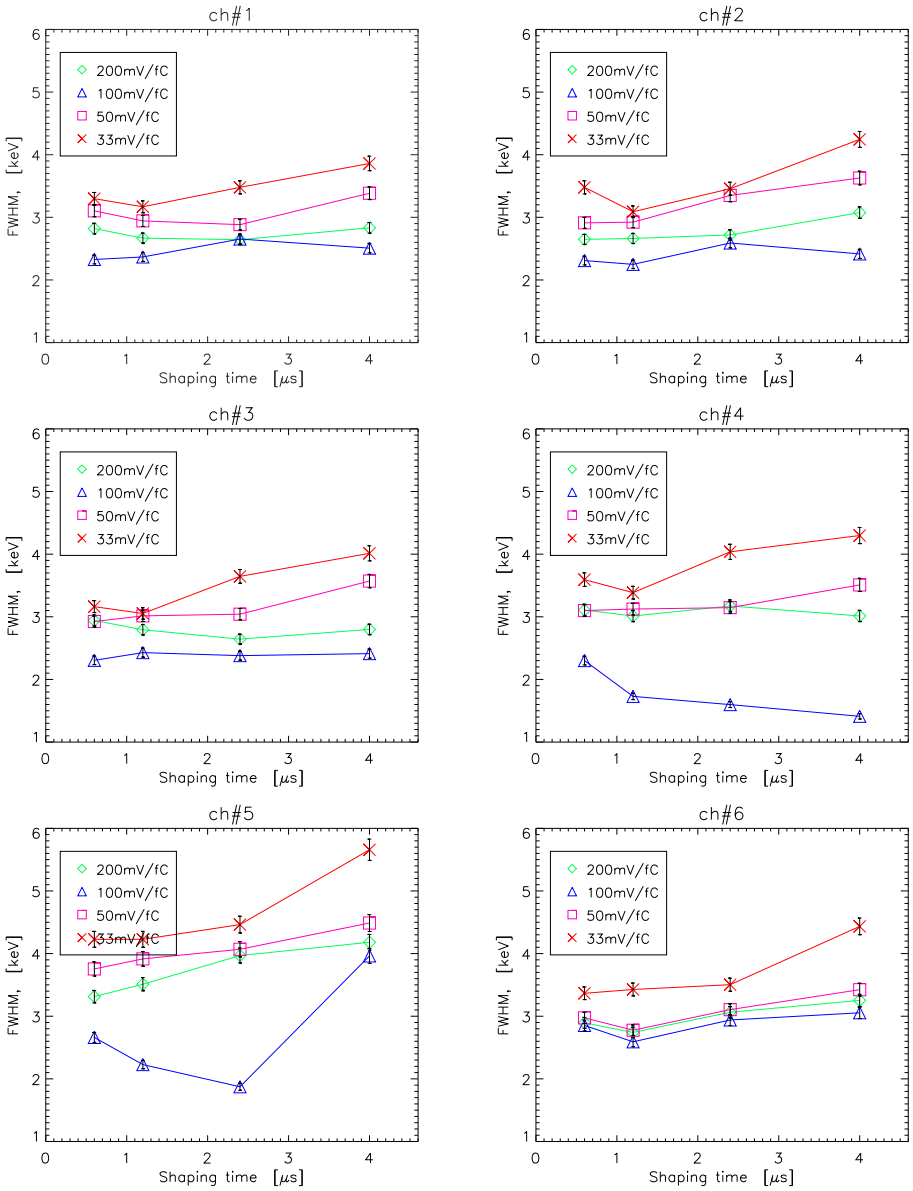

Figure A.3 The measured electronic noise (in keV) as a function of shaping time with different gain settings. The operation voltages are (Vp,Vd)=(-300V,-100V). Gain 200 mV/fC and shaping time 1.2 μs as shown in ch2, yielding a total noise 2.7 keV

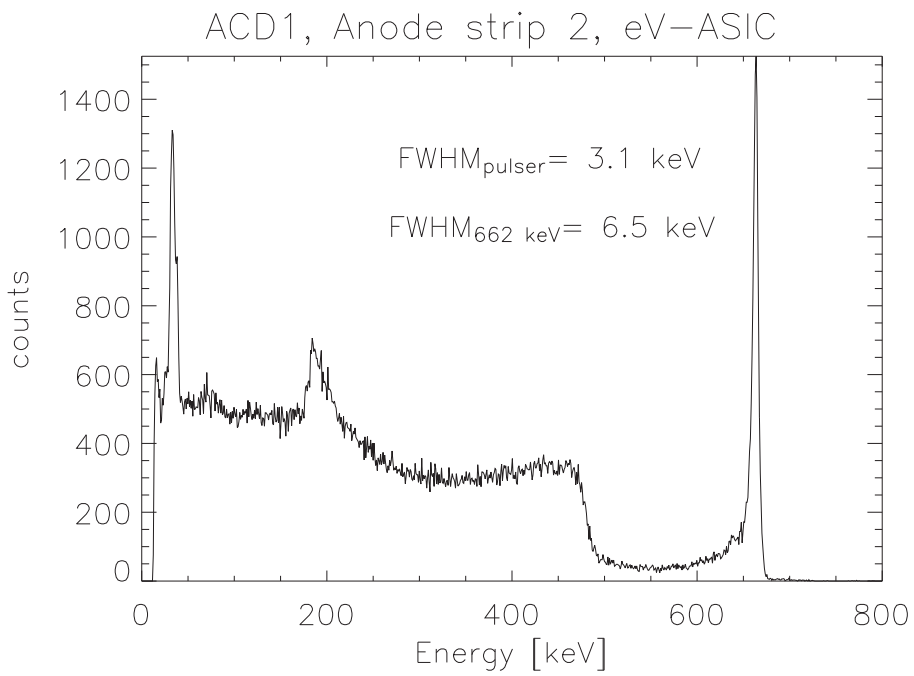

Figure A.4 ^{137}Cs spectrum was measured by the GSFC-CZT-4 using the eV-ASIC shown in Fig. A.2. The spectra were recorded from the anode strip 2 and the planar electrode in coincident. The spectrum is energy calibrated and corrected. Total electronic noise was 3.1 keV FWHM for the anode strip number 2. The shaping time is 1.2 μs. The ASIC gain is 200 mV/fC. The operation temperature was 22^oC. The operation voltages were Vp=-300V and Vp=-100V.

planned in future.

B

Appendix

B.1 Radiation damage experiment

A series of proton beam irradiation measurements have been carried out on a CdZnTe drift strip detector (the GSFC-CZT-1 detector) to study the effect of the proton damage. The proton irradiation reported in this thesis was performed at the cyclotron facility at the Copenhagen University Hospital using a Scanditronic MC32-NI cyclotron. The exit beam energy of the cyclotron was calibrated to be 31.3 ± 0.5 MeV. The beam energy was attenuated by a 25 μm Havar window (~ 0.4 MeV), 50 cm air (~ 0.8 MeV), and then by a 100 μm Al (~ 0.4 MeV) foil in front of the detector. Thus the detector itself was irradiated with protons of 29.7 ± 0.7 MeV. Although the test set-up and the dedicated software are specific to the purpose of the proton irradiation of the CdZnTe drift strip detector, they can be used to irradiate other materials as well.

Two important functions are worth to mention for the set-up. The first is the automated positioning of the Faraday Cup (FC) center relative to the proton beam center (the accuracy in positioning is $\pm 1mm$). This is relevant when the target to be irradiated is "large" compare to the proton beam and an almost homogenous proton fluence is required. This is achieved by sweeping the whole area in front of the circular proton beam with a constant speed. A zigzag path can be composed relative to a start point. The start point in this experiments is the FC center which is fixed on the XY-table together with the target. Positioning the FC center to the proton beam center can be used as a start point for the zigzag path.

The second is the measured beam profile before the irradiation process allowing one to calculate the proton fluence. This can be used to irradiate the

target with the planed proton fluence and it can be adjusted by two variables. The first variable is the beam current (strictly dependent on Cyclotron operation parameters) and the second variable is the velocity of the target following a zigzag path in front of the proton beam (the proton fluence is dependent of the total exposure time during irradiation process). A sort of "user guide" to the irradiation experiment is given in this appendix to help others to use the set-up for similar irradiation experiments.

B.2 Experimental setup

The chopper function was considered to perhaps effect the beam current profile.Therefore the beam profile was tested and no significant change in the shape of the beam current distribution was observed after the chopper was installed. The XY-table moved the detector in a zigzag path in order to ensure a uniform irradiation. A Faraday Cup (FC) was attached to the system in order to measure the beam intensity and and the beam profile just before the irradiation process. Fig. B.9 shows a beam profile recorded from an x-scan. The beam was in the z-axis direction, i.e., horizontal and perpendicular to the XY-table. The opening to the FC is circular with a diameter equal to 10 mm. The measurement was done after a number of beam scans in x- and y-direction using the software developed for the irradiation experiment. The beam parameters then were used to calculate the proton fluence given to the detector.

For the irradiation process, the target was moved with a constant velocity in a zigzag path in front of the beam thus the area of $40 \times 40mm^2$ was irradiated. The detector was placed in the center of the rectangular area with the planar electrode facing the proton beam. The irradiation of the detector lasted typically 40 s. All electrodes of the detector were held at ground potential during the irradiation process.

B.2.1 Hardware

The test bench is shown in Fig. B.1. It consists of a main support (which is fixed during irradiation experiment) and a supporting table (XY-table) provided with two independent movements, driven by two stepping motors along orthogonal directions (x and y directions). This table is complemented by a Faraday Cup (FC) and a readout system based on a charge sensitive preamplifier. For the beam profile measurement, the FC signal is amplified and digitized. A charge sensitive preamplifier is designed and constructed for this purpose. An ADC is installed in order to digitize the signals. The Calibration of the FC-charge sensitive preamplifier-ADC chain was performed with care. The ADC was configured so that the beam current of 1 to 270 pA could be

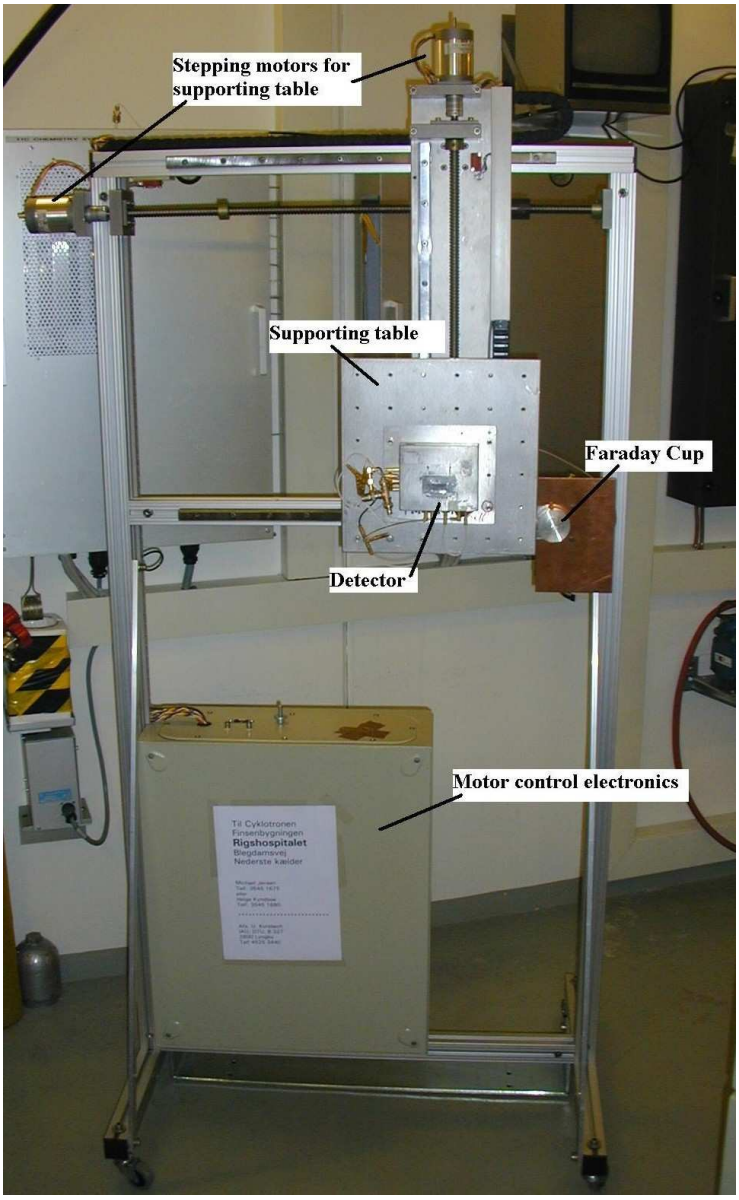
Stepping motors for supporting table
Supporting table
Faraday Cup
Detector
Motor control electronics
Til Cyklotronen
Finsenbygningen
Rigshospitalet
Blegdamsvej
Nederste kælder

Figure B.1

measured with a highest accuracy. The ADC dynamic range can be changed for other experiment requiring a measurement of the beam current higher then 270 pA. The FC-preamplifier-ADC chain must be calibrated and implemented in the software. The ADC and two step motor controllers were using a standard IEEE 485 serial communication protocol [1] and port. This table supports a removable holder that contains the detector to be irradiated. The detector is positioned in front of the proton beam using the x- and the y-motor along the zigzag path. For the beam profile, the proton beam current was measured with the Faraday Cup (FC) during the passage of the proton beam at each position of 1 mm (x or y directions). The beam current measured by the FC (current signal amplified and converted to a voltage signal by a charge sensitive preamplifier and digitized by an ADC) is recorded.

B.2.2 Software

The methods described in note by Korsbech [43] were used to prepare the irradiation experiment set-up system and the theoretical calculations of the determination of the proton fluences used in this irradiation experiment. The test bench is automated and the data is recorded by a Personal Computer (PC). A dedicated software developed using the LabView [2] (LABoratory Virtual Instrument Engineering Workbench) package. The software was planned for controlling the motors and external hardware. As with most programs, during the developing stage, there were many obstacles. The software was planned and constructed from a simple set of tested procedures and functions. The position resolution of the XY-table ($\sim 159.87 step/mm$) and the speed were tested in both direction, and limitation and calibration were implemented in the software. The charge amplifier output related to beam current data is retained along with the position history data. This information is saved into two different computer files. The data contain the measured beam current in pA for each 1 mm step with a date and time information. The data are also displayed on the screen during the scan. Controls are provided to scan and to locate the proton beam center by repeating a number of scans in the x or y directions. After each scan, the current to the FC when passing through the proton beam is measured. The current distribution [3] curve is fitted with a Gaussian curve. Two option is available for the beam profile obtained from the scan. It can be rejected by pressing the "reset" button or it can be accepted

[1] IEEE-485 is a standard of the Institute of Electrical and Electronic Engineers that defines a method of interfacing instruments. The IEEE-485 interface are used for communication and control between the computer and XY table.

[2] © National Instruments

[3] The current distribution is almost symmetric, and the current could with good approximation be described by a Gaussian (peak) curve [43].

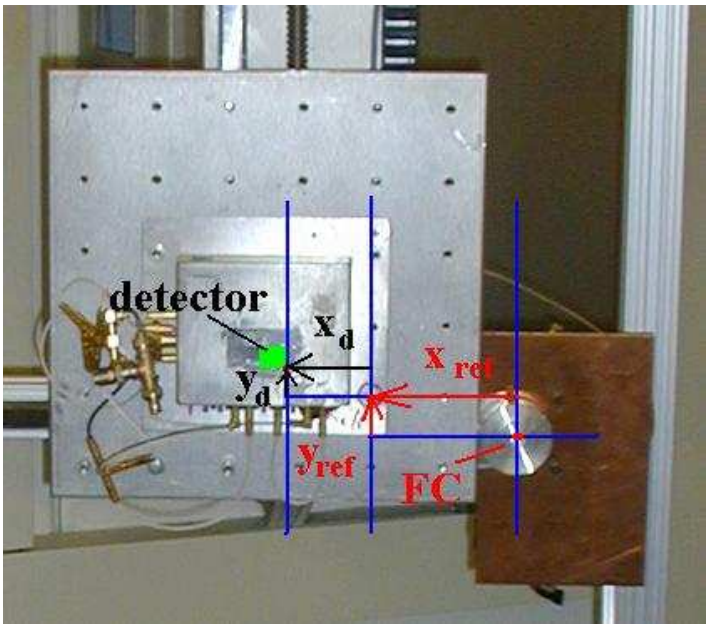

Figure B.2 The detector position is fixed relative to a reference point on the holder. The reference point is the center of the hole at the right bottom corner of the holder. The position is measured for this experiment as (x_d,y_d)=(64 mm, 31 mm) and implemented in the software as a constant. The y_{ref} distance from the FC center must be selected with precautions so that during the beam scan one does not expose the detector to the proton beam.

by pressing the "accept" button.

After the beam profile is completed and the FC center is positioned at the proton beam center, the irradiation process can be started as a second part of the software. The parameters extracted from the last recorded and accepted beam profile is transferred to the second part of the software. The general function of this second part is to perform the irradiation process. A function is implemented in this software to calculate the proton fluence before starting the irradiation process. In this way, planned fluence can be achieved by adjusting the target velocity for the process. However, there is a velocity limit for the supporting table in x and y directions which is found to be approximately 4 cm/s. If the planned proton fluence require higher target speed then the proton beam current must be adjusted instead. The target velocities used in

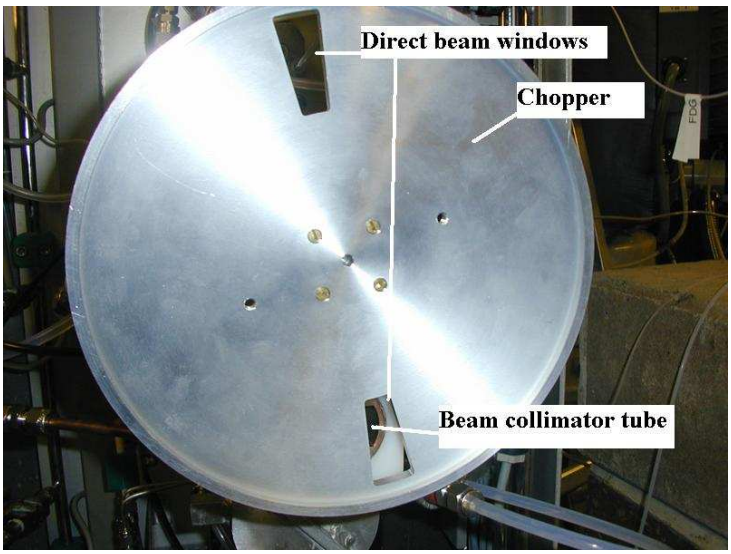

Figure B.3 The main function of the chopper is to reduce the proton beam current for the experiments which require very low beam current (< 100 pA). The proton beam from the cyclotron becomes unstable for beam current less then 100pA. Therefore a chopper with two direct beam window each with a 11^o wide opening was designed and constructed.

this irradiation experiment was in the order of 1 cm/s.

B.3 Measurement procedure

1. The test bench must be moved and placed into the Cyclotron rum. In the control room, the PC with the operative system Windows95 [4] and the installed National Instruments LabView software package must be started. The application program "Radiation damage.vi" must be started. The communication cable and the power cable for the test bench must be plugged in. The batteries (2x9V) must be installed for the charge sensitive preamplifier. The output of the FC must be connected to the input of the preamplifier. The target must be fixed on a removable holder. In this experiment, the detector is fixed on a removable holder and it is shown in Fig. B.2. The detector position is fixed relative to a refer-

[4] © Microsoft Windows®95

ence point on the holder. The reference point is the center of the hole at the right bottom corner of the holder. The position is measured for this experiment as (x_d,y_d)=(64 mm, 31 mm) and implemented in the software as a constant. For other experiments requiring a different size of the holder, this can be changed in the software. The operator must change the constants named as x_{offset} and $y_{offsett}$ in the software. The detector holder can be placed at a proper position on the XY table far from the FC center. The position of the reference point on the holder relative to the FC center is given by x_{ref} and y_{ref}. The y_{ref} distance from the FC center must be selected with precautions so that during the beam scan one does not expose the detector to the proton beam. The operator must record the x_{ref} and y_{ref} for later use in the software as an input parameter.

2. The "chopper" must be installed on the beam collimator tube. The high pressure air supply mechanisms to rotate the "chopper" must be installed. The chopper is an option for the irradiation experiments which require very low beam current (< 100 pA). The installed chopper on the beam collimator tube is shown Fig. B.3.

3. The power cable to the test bench must be unplugged so the XY table can be manually controlled (pull and push to direction). The FC center must be positioned relative to beam collimator opening as accurate as possible so the proton beam can illuminate the FC center by moving the XY-table manually. The set-up after a such an alignment is shown in Fig. B.4. The power cable to the test bench must be plugged back.

4. A "dummy" irradiation test (without proton beam) must be performed in order to verify the connections, software and the hardware. The operator inspects the dummy test with the camera installed inside the cyclotron room to ensure the functionality. When the test confirms that the set-up is ready for the final irradiation experiment, the high pressure air flow must be started for the "chopper". The "chopper" must rotate at high speed. This high rotation speed is important for the beam profile measurements. The operator must ensure the FC center position alignment relative to the beam collimator once again before sealing the cyclotron room.

5. For the final irradiation process, the proton beam must be "on" (started). If the FC is placed in front of the proton beam then the current indicator on the main screen (see Fig. B.5) will show the measured beam current in pA every second. The position of the proton beam center must be determined using the scan function. The scan direction can be selected

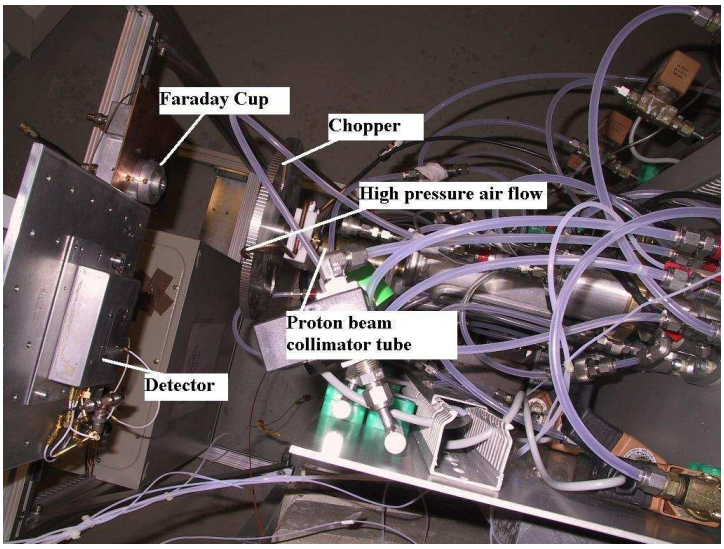

Figure B.4 The FC center was positioned manually relative to the beam (to the beam collimator opening).

using the drop down menu button. There are two options to select. The x-direction which is a horizontal scan and y-direction which is a vertical scan. Both direction must be performed at least one or more time until the operator is convinced that the FC is positioned at the beam center. The scan length must be given in mm ($50mm \leq$ scan length $\leq 100mm$). The length should be selected so the whole beam can be scanned in the first scan. The operator can send the instructions to the XY table hardware using the yellow "send" button after the scan length and scan direction are selected.

6. The "send" button will download a set of instructions to the controllers and then upload the instructions from the controller's memory. This information will be shown in a text box. This text box is used to ensure the functionality of the communication between PC and the XY table. At the same time a new function button, the "Execute program" button will appear on the screen as shown in Fig. B.6. When activating this button the scan process will start. A plot of beam current versus FC center position relative to the proton beam will gradually be displayed on the PC screen as shown in Fig. B.7. When the scan is finished a new

function button, the "Fit" button will appear on the screen as shown in Fig. B.8. The fit button function is to approximate the measured beam current distribution with a Gaussian curve. If a reasonable peak is obtained and the fit is applied successfully (as shown in Fig. B.9) then two new function button will appear on the screen. The "Accept" function button is to accept the fit results and move the FC center to the obtained peak position. From here a new scan can be performed. However, the "Reset" function button is to reject the fit results and move the FC center to its original start position. The operator can repeat the scan process several times until the FC center is at the position of the beam center. The data file of the graph is stored on disk for every accepted scan in the x and y direction. The scan data will be saved (appended) with a time information into two files "maxx.txt" and "maxy.txt" respectively. The files are located at the root directory of the PC (i.e., "C:\maxx.txt"). These data can be used to calculate the proton fluence later.

7. At the end of the scan process, the last fit parameters are also stored in the memory. These parameters will then be used for the final irradiation process. The red button "start irradiation" will start the second part of the irradiation program. An new screen will appear as shown in Fig. B.10 with a proton fluence calculator. The operator must provide some physical parameter here such as the position of the detector holder x_{ref} and y_{ref} relative to the FC center on the supporting table and the target speed. A constant velocity is used for the irradiation process. The operator can calculate the proton fluence before the final irradiation process by pressing the "calculate" button. The proton fluence can be changed by changing the velocity. When the calculated proton fluence coresponds to the planned fluence then the final zigzag path can be send to the controllers by pressing the "send" button. A new button "Run" which function is to start final irradiation process will appear on the screen as shown in Fig. B.13. This final irradiation process can be repeated many times and an indicator named "counter" will show the number of finished irradiation processes on the screen.

8. After the irradiation process, the operator must backup the files ("maxx.txt" and "maxy.txt") stored on disk during the beam scan.

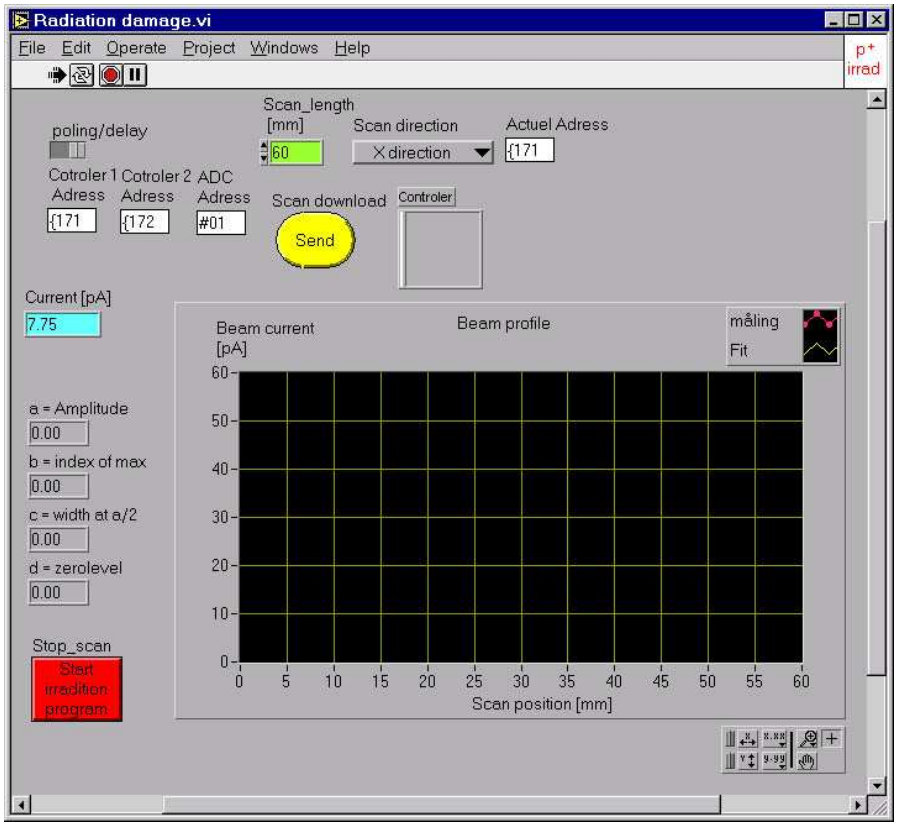

Figure B.5 The main screen for the application program. The operator must locate the proton beam center using the scan function. The scan direction can be selected using the drop down menu button. There are two options to select. The X-direction which is a horizontal scan and Y-direction which is a vertical scan. Both direction must be performed at least once until the operator is convinced that the FC is positioned at the beam center. The scan length must be given in *mm*. The length should be selected so the whole beam can be scanned in the first scan.

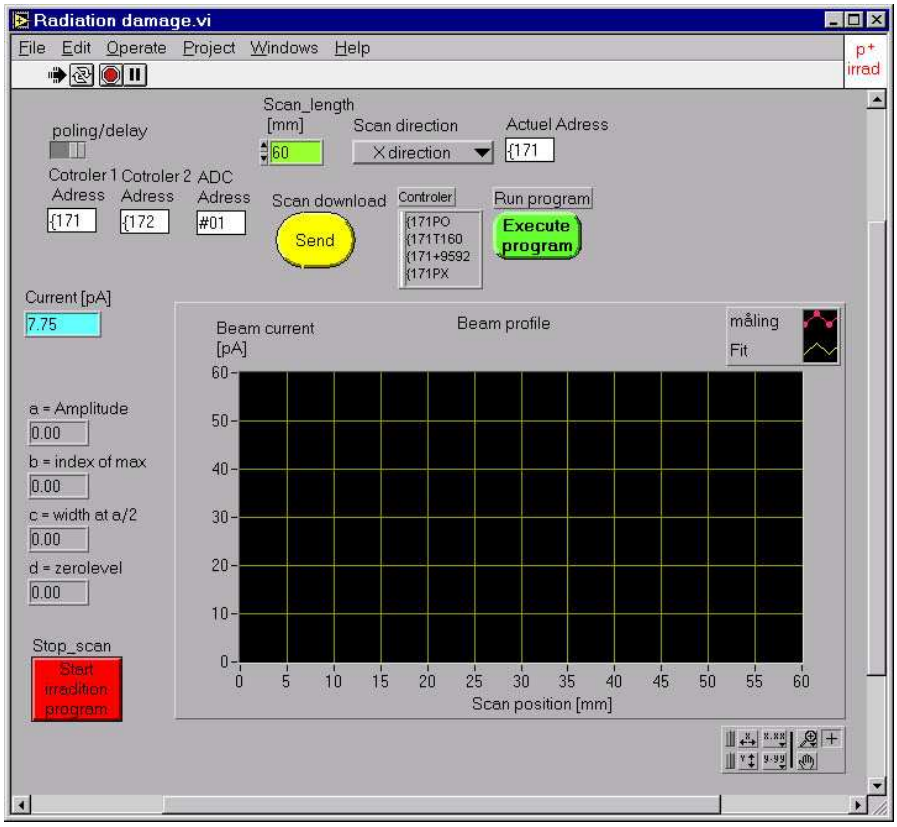

Figure B.6 The operator can send the instructions to the XY table hardware using the yellow "send" button after the scan length and scan direction is selected. The "send" button will download the instruction to the controllers and then upload the instruction from the controller's memory. This information will be shown in a text box and is used for confirmation of the functionality of the communication between PC and the XY table. At the same time a new function button, the "Execute program" button will appear on the screen.

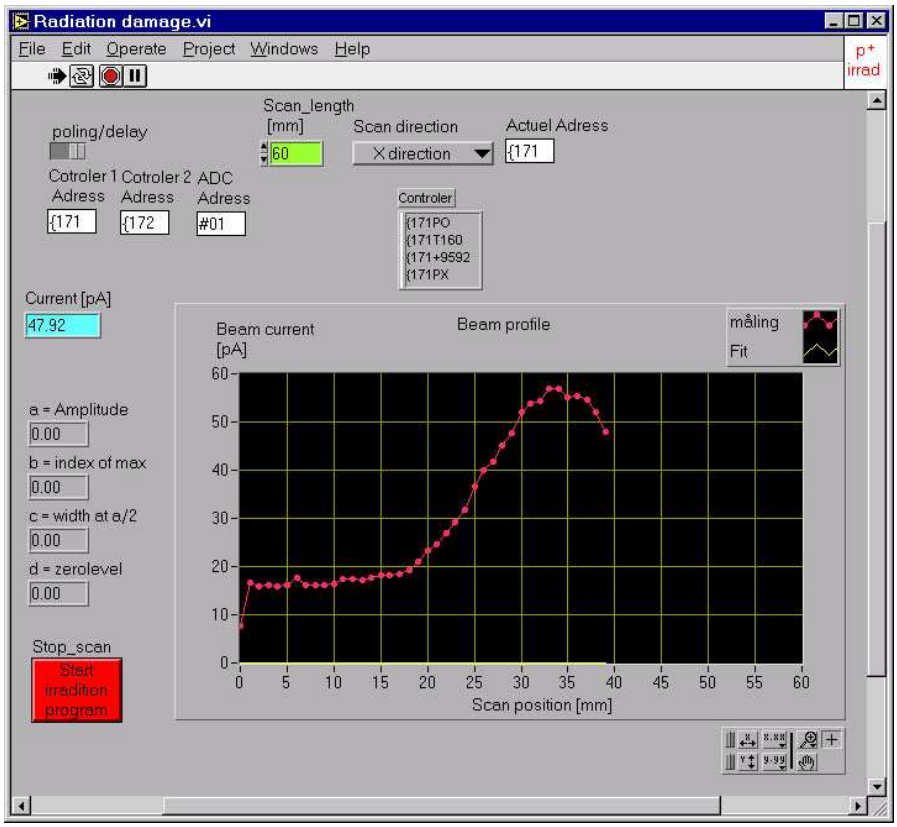

Figure B.7 When activating the "Execute program" button the scan process will start and measured beam current will be updated online on the screen. A plot of beam current versus FC center position relative to the beam is gradually displayed on the PC screen.

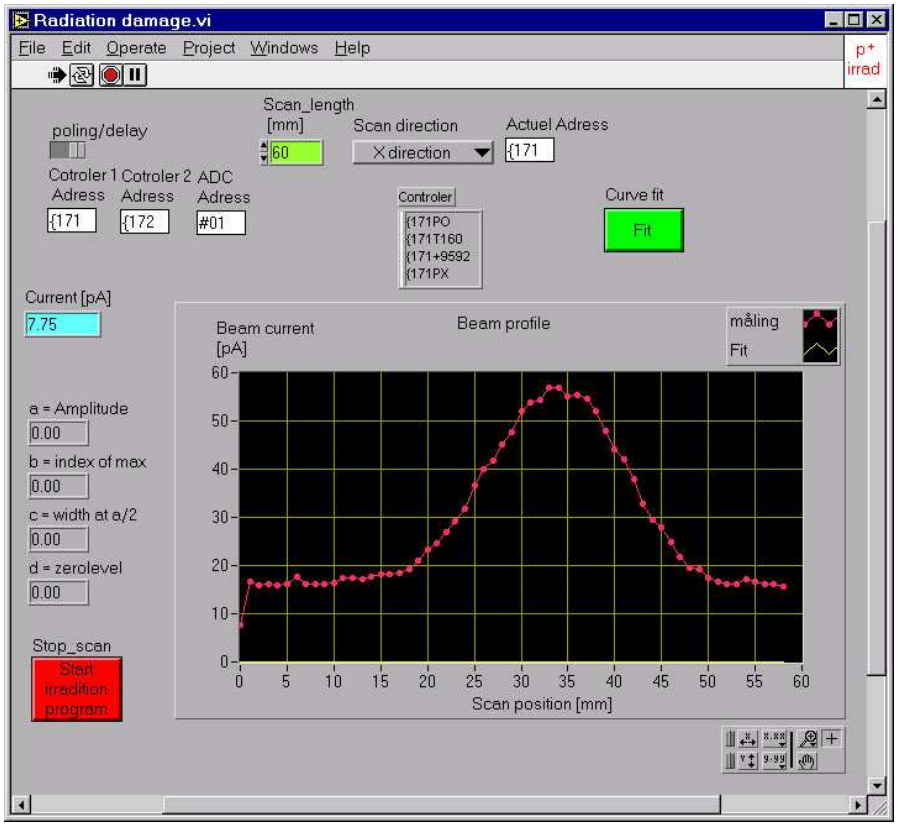

Figure B.8 When the scan is finished then a new button "Fit" which function is to approximate the measured beam current with a Gaussian curve will appear on the screen.

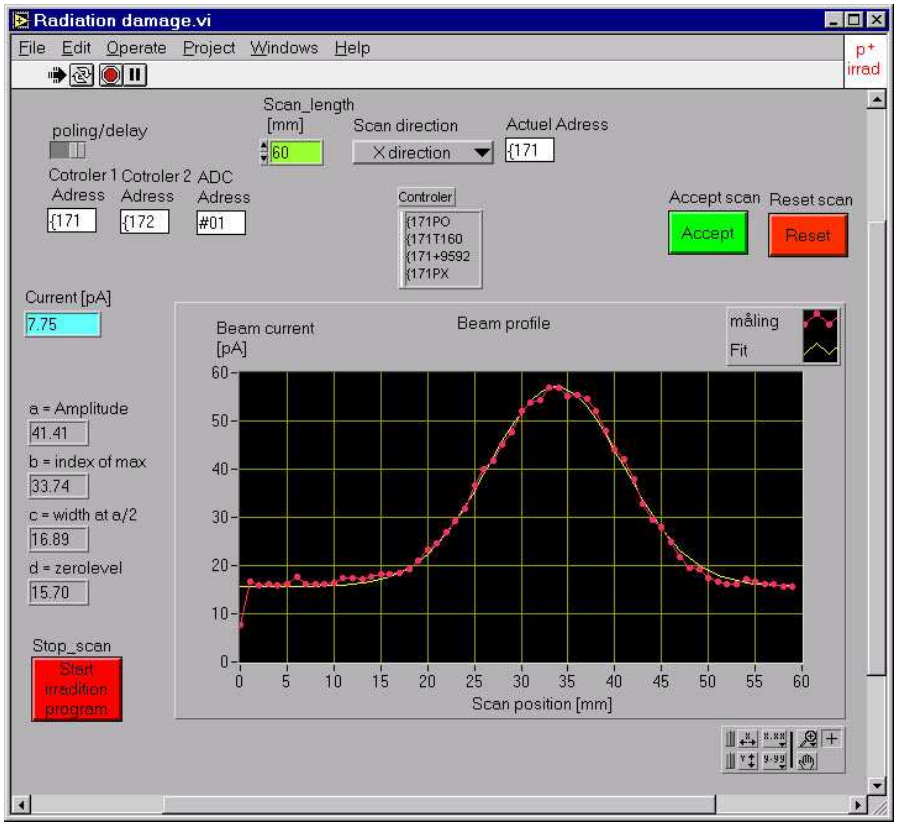

Figure B.9 If a reasonable peak is obtained and the fit is applied successfully, then two new function button will appear on the screen. The "Accept" button which function is to accept the fit results and move the FC center to the obtained peak position and the "Reset" button which function is to reject the fit results and move the FC center to its original position for start of a new scan.

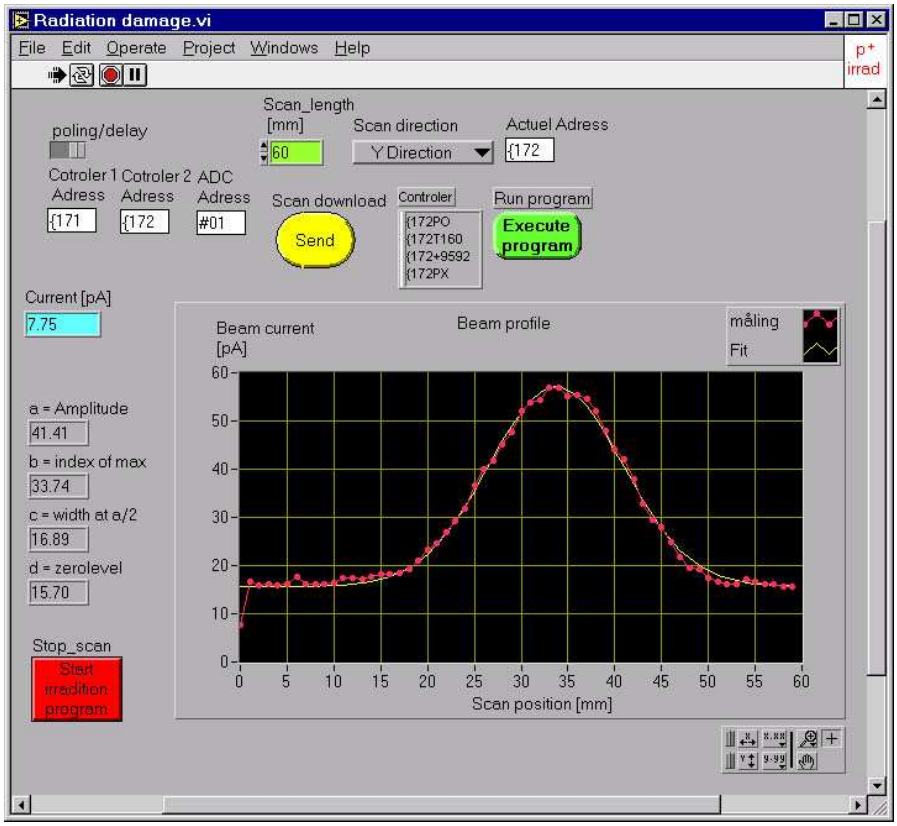

Figure B.10 The proton beam scan direction can be selected using the drop down menu button. The scan must be performed in both direction. At the end of the scan process, the last fit parameters are stored in the memory. These parameters will then be used for the final irradiation process. The red button "Start irradiation" will start the irradiation program.

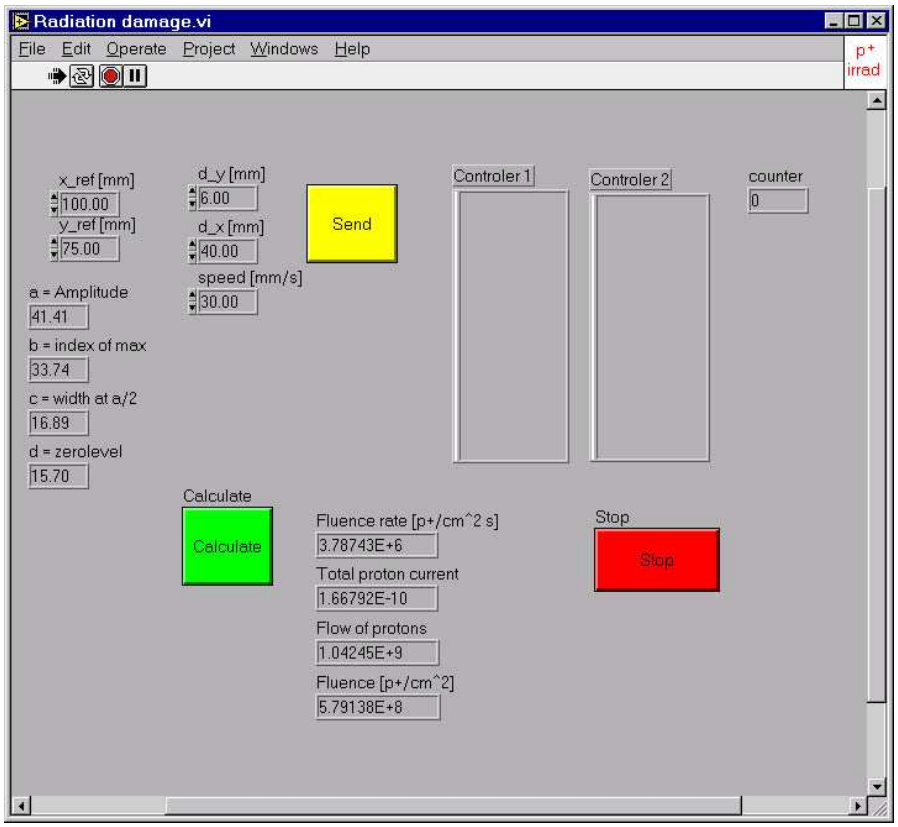

Figure B.11 The second part of the application software. Some physical parameter i.e., the position of the detector holder x_{ref} and y_{ref} relative to the FC center on the supporting table and the beam velocity must be provided here.

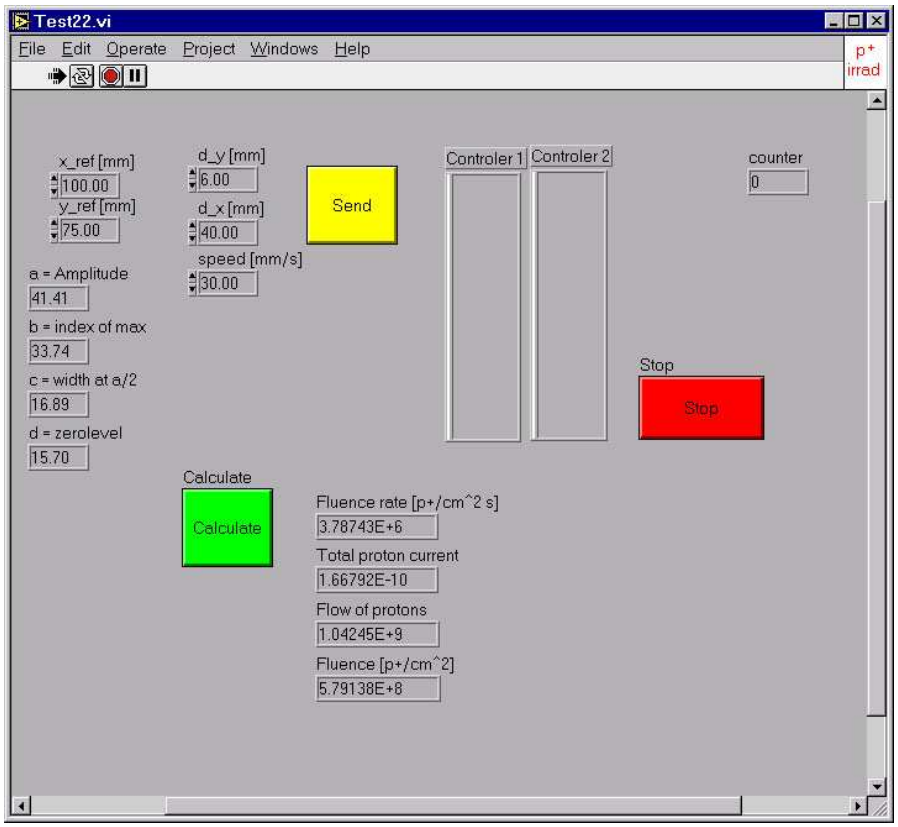

Figure B.12 The operator can calculate the proton fluence in advance by pressing the "calculate" button. When the calculated proton fluence is accepted the final zigzag path can be sent to the controllers by pressing the "send" button.

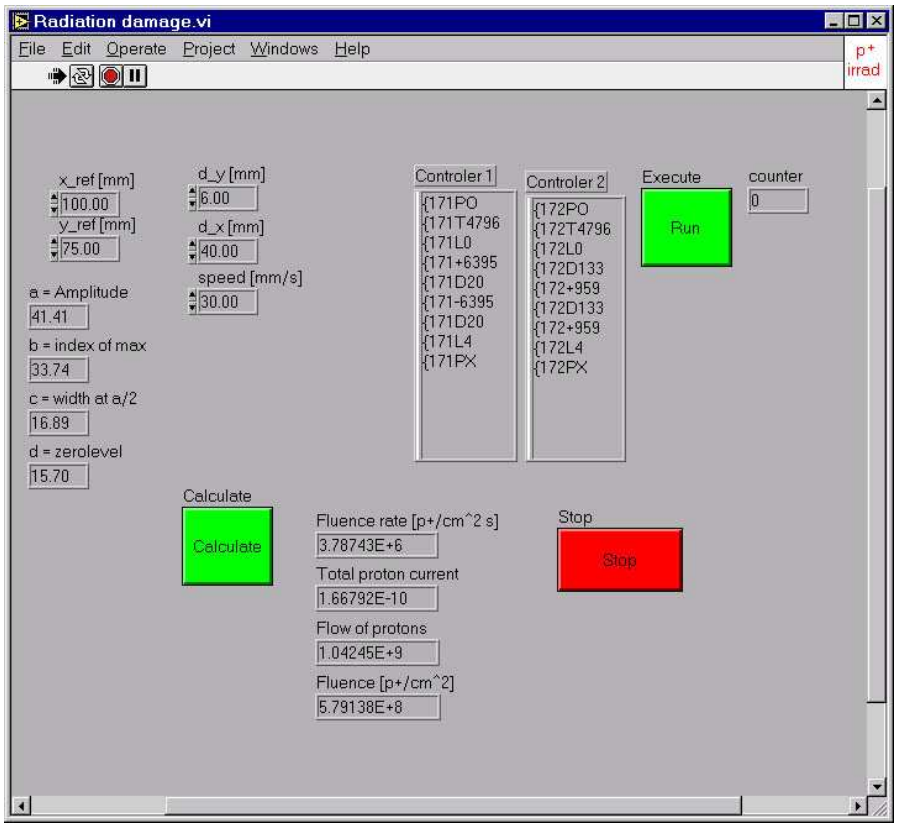

Figure B.13 A new button "Run" which function is to start final irradiation process will appear on the screen. This irradiation process can be repeated many times and an indicator named "counter" will show the number of finished irradiation processes on the screen.

C

Appendix

C.1 The calculation of the damage profile using the computer software TRIM

====== H (10) into CdZnTe =======
SRIM-2003.10
===
Ion and Target VACANCY production
See SRIM Outputs\TDATA.txt for calc. details
===

Recoil/Damage Calculations made with Kinchin-Pease Estimates

See file : SRIM Outputs\TDATA.txt for calculation data
Ion = H Energy = 30000 keV
========== TARGET MATERIAL =========
Layer 1 : CdZnTe
Layer Width = 3.E+07 A ;
Layer # 1- Density = 3.018E22 atoms/cm3 = 5.78 g/cm3
Layer # 1- Cd = 40 Atomic Percent = 38.9 Mass Percent
Layer # 1- Zn = 10 Atomic Percent = 5.67 Mass Percent
Layer # 1- Te = 50 Atomic Percent = 55.3 Mass Percent
===
Total Ions calculated =7590078.00
Total Target Vacancies = 126 /Ion
===

Table Units are >>>> Vacancies / Angstrom / Ion <<<<

TARGET DEPTH (Ang.)	VACANCIES by IONS	VACANCIES by RECOILS
300000.E+00	3540.58E-10	1010.26E-09
600000.E+00	4819.48E-10	1413.23E-09
900000.E+00	4853.75E-10	1406.53E-09
120000.E+01	4887.15E-10	1424.17E-09
150000.E+01	4916.25E-10	1474.58E-09
180000.E+01	4951.41E-10	1410.59E-09
210000.E+01	4981.82E-10	1421.17E-09
240000.E+01	5013.63E-10	1408.82E-09
270000.E+01	5039.66E-10	1437.58E-09
300000.E+01	5077.86E-10	1441.28E-09
330000.E+01	5117.02E-10	1443.66E-09
360000.E+01	5139.29E-10	1568.90E-09
390000.E+01	5184.24E-10	1504.71E-09
420000.E+01	5215.74E-10	1499.88E-09
450000.E+01	5255.80E-10	1511.78E-09
480000.E+01	5289.14E-10	1528.32E-09
510000.E+01	5332.21E-10	1535.13E-09
540000.E+01	5370.05E-10	1508.48E-09
570000.E+01	5403.31E-10	1533.69E-09
600000.E+01	5455.53E-10	1529.76E-09
630000.E+01	5488.53E-10	1557.63E-09
660000.E+01	5530.29E-10	1551.40E-09
690000.E+01	5571.30E-10	1591.83E-09
720000.E+01	5614.86E-10	1588.45E-09
750000.E+01	5657.24E-10	1655.13E-09
780000.E+01	5707.85E-10	1628.84E-09
810000.E+01	5739.00E-10	1599.56E-09
840000.E+01	5798.82E-10	1659.64E-09
870000.E+01	5833.65E-10	1664.09E-09
900000.E+01	5900.40E-10	1677.98E-09
930000.E+01	5938.72E-10	1660.91E-09
960000.E+01	5998.12E-10	1663.70E-09
990000.E+01	6054.93E-10	1733.75E-09
102000.E+02	6099.50E-10	1729.91E-09
105000.E+02	6169.98E-10	1763.70E-09

108000.E+02	6219.92E-10	1794.61E-09
111000.E+02	6271.53E-10	1786.48E-09
114000.E+02	6341.68E-10	1816.12E-09
117000.E+02	6400.78E-10	1801.69E-09
120000.E+02	6470.29E-10	1811.70E-09
123000.E+02	6532.06E-10	1815.80E-09
126000.E+02	6593.67E-10	1820.82E-09
129000.E+02	6657.67E-10	1871.02E-09
132000.E+02	6734.27E-10	1901.22E-09
135000.E+02	6803.79E-10	1912.21E-09
138000.E+02	6880.82E-10	1921.23E-09
141000.E+02	6971.03E-10	1980.59E-09
144000.E+02	7035.88E-10	1979.97E-09
147000.E+02	7131.98E-10	2007.02E-09
150000.E+02	7215.09E-10	2009.95E-09
153000.E+02	7290.37E-10	2068.49E-09
156000.E+02	7391.26E-10	2016.62E-09
159000.E+02	7493.59E-10	2128.47E-09
162000.E+02	7587.14E-10	2106.76E-09
165000.E+02	7686.65E-10	2155.49E-09
168000.E+02	7803.60E-10	2221.39E-09
171000.E+02	7911.15E-10	2220.45E-09
174000.E+02	8019.78E-10	2183.66E-09
177000.E+02	8128.36E-10	2192.83E-09
180000.E+02	8265.12E-10	2301.25E-09
183000.E+02	8388.23E-10	2347.60E-09
186000.E+02	8522.17E-10	2374.40E-09
189000.E+02	8664.93E-10	2398.00E-09
192000.E+02	8795.86E-10	2434.59E-09
195000.E+02	8953.35E-10	2484.19E-09
198000.E+02	9123.44E-10	2531.93E-09
201000.E+02	9293.84E-10	2563.54E-09
204000.E+02	9457.53E-10	2511.96E-09
207000.E+02	9649.29E-10	2682.98E-09
210000.E+02	9848.61E-10	2685.71E-09
213000.E+02	1004.75E-09	2737.03E-09
216000.E+02	1028.11E-09	2780.20E-09
219000.E+02	1051.78E-09	2800.36E-09
222000.E+02	1076.69E-09	2945.51E-09
225000.E+02	1104.18E-09	2939.78E-09
228000.E+02	1132.37E-09	3033.18E-09

231000.E+02	1165.23E-09	3170.09E-09
234000.E+02	1198.04E-09	3144.06E-09
237000.E+02	1232.91E-09	3311.89E-09
240000.E+02	1271.46E-09	3399.64E-09
243000.E+02	1314.37E-09	3459.54E-09
246000.E+02	1361.28E-09	3655.78E-09
249000.E+02	1413.03E-09	3705.78E-09
252000.E+02	1469.07E-09	3863.02E-09
255000.E+02	1532.80E-09	3974.61E-09
258000.E+02	1604.41E-09	4170.70E-09
261000.E+02	1686.18E-09	4362.24E-09
264000.E+02	1781.52E-09	4566.24E-09
267000.E+02	1893.28E-09	4815.63E-09
270000.E+02	2025.03E-09	5116.56E-09
273000.E+02	2184.69E-09	5445.75E-09
276000.E+02	2387.52E-09	5862.80E-09
279000.E+02	2652.40E-09	6441.13E-09
282000.E+02	3029.92E-09	7204.73E-09
285000.E+02	3627.44E-09	8292.68E-09
288000.E+02	4687.40E-09	9982.77E-09
291000.E+02	6466.15E-09	1235.70E-08
294000.E+02	8586.02E-09	1443.85E-08
297000.E+02	9435.16E-09	1414.72E-08
300000.E+02	7666.71E-09	1053.99E-08

To convert to Energy Lo- multiply by Average Binding Energy = 3 eV/Vacancy

C.2 The calculation of the stopping range of 30 MeV protons in the CdZnTe using the computer software SRIM

==========

Calculation using SRIM-2003
SRIM version —> SRIM-2003.10
Calc. date —> March 11, 2003
==========
Disk File Name = SRIM Outputs\Hydrogen in Cd-Zn-Te
Ion = Hydrogen [1] , Mass = 1.008 amu
Target Density = 5.7800E+00 g/cm3 = 2.9585E+22 atoms/cm3
======== Target Composition ========
Atom Atom Atomic Mass

Name Numb Percent Percent
—- —- ——- ——-
Cd 48 045.00 042.99
Zn 30 005.00 002.78
Te 52 050.00 054.23
==========
Bragg Correction = 0.00%
Stopping Units = MeV / mm
See bottom of Table for other Stopping units
Ion dE/dx dE/dx Projected Longitudinal Lateral
Energy Elec. Nuclear Range Straggling Straggling
——— ———- ———- —
10.00 keV 5.962E+01 7.986E-01 987 A 760 A 615 A
11.00 keV 6.236E+01 7.724E-01 1076 A 799 A 650 A
12.00 keV 6.494E+01 7.482E-01 1165 A 835 A 684 A
13.00 keV 6.737E+01 7.256E-01 1252 A 869 A 717 A
14.00 keV 6.967E+01 7.046E-01 1339 A 902 A 748 A
15.00 keV 7.185E+01 6.849E-01 1425 A 933 A 779 A
16.00 keV 7.391E+01 6.665E-01 1511 A 962 A 808 A
17.00 keV 7.587E+01 6.492E-01 1595 A 990 A 836 A
18.00 keV 7.774E+01 6.330E-01 1679 A 1017 A 864 A
20.00 keV 8.121E+01 6.032E-01 1846 A 1068 A 917 A
22.50 keV 8.509E+01 5.703E-01 2051 A 1127 A 979 A
25.00 keV 8.854E+01 5.414E-01 2253 A 1180 A 1038 A
27.50 keV 9.160E+01 5.157E-01 2453 A 1231 A 1094 A
30.00 keV 9.432E+01 4.927E-01 2650 A 1278 A 1147 A
32.50 keV 9.673E+01 4.721E-01 2846 A 1322 A 1198 A
35.00 keV 9.888E+01 4.533E-01 3041 A 1364 A 1247 A
37.50 keV 1.008E+02 4.363E-01 3234 A 1403 A 1295 A
40.00 keV 1.025E+02 4.206E-01 3427 A 1441 A 1341 A
45.00 keV 1.053E+02 3.930E-01 3809 A 1512 A 1430 A
50.00 keV 1.076E+02 3.692E-01 4190 A 1579 A 1514 A
55.00 keV 1.093E+02 3.486E-01 4569 A 1641 A 1596 A
60.00 keV 1.107E+02 3.304E-01 4948 A 1700 A 1674 A
65.00 keV 1.118E+02 3.143E-01 5327 A 1755 A 1750 A
70.00 keV 1.126E+02 3.000E-01 5706 A 1809 A 1824 A
80.00 keV 1.135E+02 2.753E-01 6468 A 1911 A 1968 A
90.00 keV 1.139E+02 2.548E-01 7237 A 2007 A 2107 A
100.00 keV 1.138E+02 2.375E-01 8012 A 2098 A 2243 A
110.00 keV 1.134E+02 2.227E-01 8796 A 2185 A 2375 A
120.00 keV 1.127E+02 2.099E-01 9590 A 2269 A 2506 A

130.00 keV 1.119E+02 1.986E-01 1.04 um 2351 A 2635 A
140.00 keV 1.109E+02 1.886E-01 1.12 um 2431 A 2763 A
150.00 keV 1.098E+02 1.797E-01 1.20 um 2510 A 2890 A
160.00 keV 1.087E+02 1.716E-01 1.29 um 2587 A 3017 A
170.00 keV 1.075E+02 1.644E-01 1.37 um 2663 A 3143 A
180.00 keV 1.062E+02 1.578E-01 1.46 um 2739 A 3270 A
200.00 keV 1.037E+02 1.462E-01 1.64 um 2892 A 3524 A
225.00 keV 1.005E+02 1.342E-01 1.86 um 3085 A 3843 A
250.00 keV 9.733E+01 1.241E-01 2.10 um 3276 A 4167 A
275.00 keV 9.431E+01 1.157E-01 2.35 um 3468 A 4495 A
300.00 keV 9.145E+01 1.084E-01 2.60 um 3660 A 4829 A
325.00 keV 8.873E+01 1.020E-01 2.86 um 3854 A 5170 A
350.00 keV 8.616E+01 9.643E-02 3.13 um 4050 A 5516 A
375.00 keV 8.375E+01 9.149E-02 3.41 um 4248 A 5870 A
400.00 keV 8.148E+01 8.708E-02 3.70 um 4448 A 6230 A
450.00 keV 7.733E+01 7.952E-02 4.30 um 4889 A 6972 A
500.00 keV 7.366E+01 7.328E-02 4.93 um 5338 A 7742 A
550.00 keV 7.039E+01 6.802E-02 5.60 um 5797 A 8540 A
600.00 keV 6.746E+01 6.353E-02 6.30 um 6265 A 9365 A
650.00 keV 6.484E+01 5.964E-02 7.02 um 6743 A 1.02 um
700.00 keV 6.247E+01 5.624E-02 7.78 um 7231 A 1.11 um
800.00 keV 5.836E+01 5.057E-02 9.38 um 8374 A 1.29 um
900.00 keV 5.492E+01 4.601E-02 11.08 um 9538 A 1.49 um
1.00 MeV 5.199E+01 4.227E-02 12.89 um 1.07 um 1.69 um
1.10 MeV 4.963E+01 3.913E-02 14.80 um 1.19 um 1.90 um
1.20 MeV 4.729E+01 3.646E-02 16.80 um 1.32 um 2.11 um
1.30 MeV 4.534E+01 3.415E-02 18.89 um 1.44 um 2.34 um
1.40 MeV 4.359E+01 3.214E-02 21.08 um 1.57 um 2.57 um
1.50 MeV 4.200E+01 3.037E-02 23.35 um 1.70 um 2.81 um
1.60 MeV 4.055E+01 2.880E-02 25.70 um 1.83 um 3.06 um
1.70 MeV 3.922E+01 2.740E-02 28.14 um 1.97 um 3.31 um
1.80 MeV 3.799E+01 2.613E-02 30.67 um 2.10 um 3.57 um
2.00 MeV 3.579E+01 2.395E-02 35.95 um 2.44 um 4.11 um
2.25 MeV 3.345E+01 2.171E-02 43.00 um 2.89 um 4.82 um
2.50 MeV 3.145E+01 1.988E-02 50.52 um 3.34 um 5.56 um
2.75 MeV 2.973E+01 1.836E-02 58.50 um 3.80 um 6.35 um
3.00 MeV 2.822E+01 1.706E-02 66.94 um 4.27 um 7.16 um
3.25 MeV 2.688E+01 1.595E-02 75.81 um 4.75 um 8.01 um
3.50 MeV 2.569E+01 1.498E-02 85.12 um 5.23 um 8.90 um
3.75 MeV 2.461E+01 1.413E-02 94.85 um 5.72 um 9.81 um
4.00 MeV 2.364E+01 1.338E-02 104.99 um 6.23 um 10.76 um

4.50 MeV 2.195E+01 1.210E-02 126.50 um 7.56 um 12.75 um
5.00 MeV 2.052E+01 1.106E-02 149.60 um 8.88 um 14.86 um
5.50 MeV 1.929E+01 1.020E-02 174.25 um 10.22 um 17.08 um
6.00 MeV 1.822E+01 9.465E-03 200.41 um 11.58 um 19.42 um
6.50 MeV 1.728E+01 8.837E-03 228.07 um 12.96 um 21.88 um
7.00 MeV 1.645E+01 8.291E-03 257.19 um 14.37 um 24.44 um
8.00 MeV 1.503E+01 7.390E-03 319.68 um 18.33 um 29.88 um
9.00 MeV 1.387E+01 6.674E-03 387.77 um 22.24 um 35.74 um
10.00 MeV 1.289E+01 6.092E-03 461.31 um 26.17 um 42.00 um
11.00 MeV 1.207E+01 5.608E-03 540.18 um 30.16 um 48.65 um
12.00 MeV 1.135E+01 5.199E-03 624.27 um 34.24 um 55.68 um
13.00 MeV 1.072E+01 4.849E-03 713.48 um 38.41 um 63.09 um
14.00 MeV 1.017E+01 4.545E-03 807.73 um 42.69 um 70.87 um
15.00 MeV 9.683E+00 4.279E-03 906.94 um 47.07 um 79.00 um
16.00 MeV 9.244E+00 4.044E-03 1.01 mm 51.55 um 87.49 um
17.00 MeV 8.849E+00 3.835E-03 1.12 mm 56.15 um 96.32 um
18.00 MeV 8.490E+00 3.647E-03 1.23 mm 60.85 um 105.50 um
20.00 MeV 7.864E+00 3.325E-03 1.47 mm 74.47 um 124.87 um
22.50 MeV 7.214E+00 2.998E-03 1.80 mm 93.56 um 150.92 um
25.00 MeV 6.677E+00 2.732E-03 2.16 mm 112.39 um 178.95 um
27.50 MeV 6.224E+00 2.511E-03 2.54 mm 131.32 um 208.92 um
30.00 MeV 5.836E+00 2.325E-03 2.95 mm 150.52 um 240.75 um

Multiply Stopping by for Stopping Units

1.0000E-01 eV / Angstrom
1.0000E+00 keV / micron
1.0000E+00 MeV / mm
1.7302E-03 keV / (ug/cm2)
1.7302E-03 MeV / (mg/cm2)
1.7302E+00 keV / (mg/cm2)
3.3800E-01 eV / (1E15 atoms/cm2)
3.6353E-01 L.S.S. reduced units

==========

References

The last line of each entry refers to the page(s) of reference in the thesis.

[1] T. Schlesinger and R. James.
Semiconductors for Room Temperature Nuclear Detector Applications, volume 43.
Acedemic Press, San Diego, California, 1995.
1, 2, 12, 19, 29, 74, 75

[2] A. Owens, H. Andersson, M. Bavdaz, C. Erd, T. Gagliardi, V. Gostilo, N. Haack, M. Krumrey, V. Lamsa, D. Lumb, I. Lisjutin, I. Major, S. Nenonen, A. Peacock, H. Sipila, and S. Zatoloka.
Development of compound semiconductor detectors for X-and gamma-ray spectroscopy.
SPIE Proceedings, **4784**, (2003), pp. 244–259.
2

[3] V. Ivanov.
Spectrometric Characteristic Improvement of CdTe detectors.
IEEE Tranc. Nucl. Sci., **42** (4), (1995), pp. 258–262.
3

[4] J. Lund, R. Olsen, J. V. Scyoc, and R. James.
The Use of Pulse Processing Techniques to Improve the Performance of Cd1-xZnxTe Gamma-Ray Spectrometers.
IEEE Tranc. Nucl. Sci., **43** (3), (1996), pp. 1411–1416.
3, 4

[5] M. van Pamelen and C. Budtz-Jørgensen.
Novel electrode geometry to improve the performance of CdZnTe detectors.
Nucl. Instr. and Meth., **A 403**, (1997), pp. 390–398.
4, 8

[6] J. Kemmer and G. Lutz.
New semiconductor detector concepts.
Nucl. Instr. and Meth., **A 253**, (1997), pp. 356–377.
4, 51

[7] G. Lutz.
Semiconductor Radiation Detectors.
Springer, New York, 1999.
4, 12, 29, 51, 86

[8] S. Sze.
Semiconductor Devices: Physics and Technology.
John Wiley & Sons, New York, 1985.

11

[9] C. Kitel.
Introduction to solid state physics.
John Wiley & Sons, New York, 1976.
11

[10] G. Knoll.
Radiation detection and measurement.
John Wiley & Sons, New York, 1989.
12, 15, 16, 18, 21

[11] E. Stassinopoulos and J. Raymomd.
The space radiation environment for electronic.
Proc. of the IEEE, **76** (11).
13, 89

[12] U. Fano.
Ionization yield of rations. II. the fluctuations of the number of ions.
Phys. Rev., **72**, (1947), pp. 26–29.
21

[13] S. Ramo.
Current induced by electron motion.
Proc. IRE, **27**, (1939), pp. 584–585.
25, 65

[14] C. Jen.
On the induced current and energy balance in electronics.
Proc. IRE., (june 1941), p. 345.
25

[15] G. Cavalleri, E. Gatti, G. Fabri, and V. Svelto.
Extention of Ramo's theorem as applied to induced charge in semiconductor detectors.
Nucl. Instr. and Meth., **92**, (1971), p. 137.
25

[16] Z. He.
Review of the Shockley-Ramo theorem and its application in semiconductor gamma-ray detectors.
Nuclear Instruments and Methods in Physics Research, **A 463**, (2001), pp. 250–267.
25

[17] K. Hecht and Z. Physik.
John Wiley & Sons, Berlin, 1932.
27

[18] T. Schlesinger, J. Toney, H. Yoon, E. Lee, B. Brunett, L. Franks, and R. James.
Cadmium zinc telluride and its use as a nuclear radiation detector material.
Material Science and Engineering, **32** (4-5), (2001), pp. 103–189.
32

[19] P. Capper.
Properties of Narrow Gap Cadmium-Based Compounds.
INSPEC, London, 1994.
32

[20] C. Szeles and M. Driver.
Growth and properties of semi-insulating CdZnTe for radiation detector application.
SPIE conference on Hard X-ray and Gamma-ray Detector Physics and Applications, **3446**, (1998), p. 1.
33

[21] A. Burger, H. Chen, K. Chattopadhyay, D. Shi, S. Morgan, W. Collins, and R. James.
Characterization of metal contacts on and surfaces of cadmium zinc telluride.
Nucl. Instr. and Meth., **A 428**, (1999), pp. 8–13.
35

[22] A. E. Bolotnikov, C. H. Chen, W. R. Cook, F. A. Harrison, I. Kuvvetli, and S. M. Schindler.
Effects of Bulk and Surface Conductivity on the Performance of CdZnTe Pixel Detectors.
Nuclear Science, IEEE tansaction, **49** (4), (2002), pp. 1941–1949.
35

[23] C. Stahle, Z. Shi, K.Hu, S. Barthelmy, S. Snodgrass, L. Bartlett, P. Shu, S. Lehtonen, and K. Mach.
Fabrication of CdZnTe strip detectors for large area arrays.
SPIE Proceedings, **3115**, (1997), pp. 90–97.
36, 52, 92

[24] *CdZnTe Material Grades.*
<http://www.evproducts.com/pdfs/Material%20Grades.pdf>.
[Accessed March 9 2003].
36

[25] P. Luke and E. Eissler.
Performance of CdZnTe coplanar-grid gamma-ray detectors.
IEEE Tranc. Nucl. Sci., **43** (3), (1996), pp. 1481–1486.
36

[26] J. Lund, R. Olsen, R. James, J. V. Scyoc, E. Eissler, M. Blakeley, J. Glick, and C. Johnson.
Performance of a coaxial geometry Cd1-xZnxTe detectors.
Nucl. Instr. and Meth., **A 377**, (1996), p. 479.
36

[27] J. Toney, B. Brunett, T. Schlesinger, H. Yoon, J. V. Scyoc, A. Antolak, D. Morse, E. Eissler, C. Johnson, J. Lund, and R. James.
Composition and performance mapping of CdZnTe nuclear spectrometers.
SPIE Proceedings, **2859**, (1996), p. 17.
36

[28] Y. Eisen and A. Shor.
CdTe and CdZnTe materials for room-temperature X-ray and gamma ray detectors.
Journal of Crystal Growth, **184/185**, (1998), pp. 1302–1312.
36

[29] Z. He, G. Knoll, D. Wehe, and J. Miyamoto.
Position-sensitive single carrier CdZnTe detectors.
Nucl. Instr. and Meth., **A 388**, (1997), pp. 180–185.
61

[30] SIR-Simulated Reality, Siegen, Germany.
Benutzerhandbuch ELFI, Ein Programm zur numerischen Berechnung zweidimensionaler elektischer Felder , 1993.
62

[31] V. Redeka.
Ann. Rev. Nucl. Part. Sci., **38**, (1988), p. 217.
74

[32] G. Bertuccio and A. Pullia.
Rev. Sci. Instr., **64**, (1993), p. 3294.
74

[33] K. Shah, P. Bennet, L. Moy, M. Misra, and W. Moses.
Characterization of indium iodide detectors for scintilation studies.
Nucl. Instr. and Meth., **A 320**, (1996), pp. 215–219.
74

[34] J. Iwanczyk, B. Patt, J. Segal, J. Plummer, G. Vilkelis, B. Hedman, K. Hodgson, A. Cox, L. Rehn, and J. Metz.
Simulation and modelling of a new silicon X-ray drift detector design for syncrotron radiation applications.
Nucl. Instr. and Meth., **A 380**, (1996), pp. 288–294.
74, 75

[35] G. Messenger and M. Ash.
Van Nostrand Reinhold, New York, 1992.
86

[36] S. Kayali, G. Ponchak, R. Shaw, C. Barnes, L. Selva, L. Aucoin, C. Chen, Y. Chou, A. Downey, R. Ferro, A. Immorlica, W. Jiang, E. Rezek, R. Romanofsk, R. Simons, and T. Trinh.
GaAs MMIC Reliability Assurance Guideline for Space Applications.
<http://nppp.jpl.nasa.gov/mmic/10.PDF>, December 15, 1996.
Chapter 10. Radiation Effects in MMIC Devices, [Accessed March 9 2003].
88

[37] E. Daly.
The Evaluation of Space Radiation Environments for ESA Projects.
ESA Journal, **12**, (1988), p. 229.
89

[38] E. Stassinopoulos.

Radiation Environment of Space.
IEEE Nuclear and Space Radiation Effects Conference Short Course.
New York, 1994.
89

[39] A. Wong, F. Harrison, and L. Varnell.
Effects of proton-induced radiation damage on Cadmium Zinc Telluride pixel detectors.
SPIE Proceedings, **2806**, (1996), p. 442.
90, 111, 113

[40] L. S. Varnell, W. A. Mahoney, E. L. Hull, J. F. Butler, and A. Wong.
Radiation effects in CdZnTe gamma-ray detectors produced by 199-MeV protons.
SPIE Proceedings, **2806**, (1996), pp. 424–431.
90

[41] L. Franks, B. Brunett, R. Olsen, D. Walsh, G. Vizkelethy, J. Trombka, B. Doyle, and R. James.
Radiation damage measurements in room-temperature semiconductor radiation detectors.
Nucl. Instr. and Meth., **A 428**, (1999), pp. 95–101.
90

[42] J. Ziegler, J. Biersack, and U. Littmark.
The Stopping and Range of Ions in Solids.
Pergamon, New York, 1985.
See <http://www.research.ibm.com/ionbeams/home.htm> for more information.
90, 103, 104, 112, 118

[43] U. Korsbech.
Exposure of space electronics and material to ionizing radiationdetermination of test methods.
Department of Automation, Tecnical University if Denmark.
94, 95, 128

[44] A. Zumbiehl, M. Hage-Ali, P. Fougeres, J. Koebel, R. Regal, and P. Siffert.
Electric field distribution in CdTe and $Cd_{1-x}Zn_xTe$ nuclear detectors.
Journal of Crystal Growth, **197**, (1999), pp. 650–654.
100

[45] R. Firestone and V. Shirley.
Table of Isotopes.
John Wiley & Sons, New York, 1996.
109

Comprehensive author index

The numbers refer to the entry in the list of references.

Lutz, G. 6, 7

Mach, K. 23
Mahoney, W. A. 40
Major, I. 2
Messenger, G. 35
Metz, J. 34
Misra, M. 33
Miyamoto, J. 29
Morgan, S. 21
Morse, D. 27
Moses, W. 33
Moy, L. 33

Nenonen, S. 2

Olsen, R. 4, 26, 41
Owens, A. 2

Patt, B. 34
Peacock, A. 2
Physik, Z. 17
Plummer, J. 34
Ponchak, G. 36
Pullia, A. 32

Ramo, S. 13
Raymomd, J. 11
Redeka, V. 31
Regal, R. 44
Rehn, L. 34
Rezek, E. 36
Romanofsk, R. 36

Schindler, S. M. 22
Schlesinger, T. 1, 18, 27
Scyoc, J. V. 4, 26, 27
Segal, J. 34
Selva, L. 36
Shah, K. 33
Shaw, R. 36
Shi, D. 21
Shi, Z. 23
Shirley, V. 45
Shor, A. 28
Shu, P. 23
Siffert, P. 44
Simons, R. 36
Sipila, H. 2
Snodgrass, S. 23
Stahle, C. 23
Stassinopoulos, E. 11, 38
Svelto, V. 15
Sze, S. 8
Szeles, C. 20

Toney, J. 18, 27
Trinh, T. 36
Trombka, J. 41

van Pamelen, M. 5
Varnell, L. 39
Varnell, L. S. 40
Vilkelis, G. 34
Vizkelethy, G. 41

Walsh, D. 41
Wehe, D. 29
Wong, A. 40

Yoon, H. 18, 27

Zatoloka, S. 2
Ziegler, J. 42
Zumbiehl, A. 44

fin.